

DEVELOPMENT OF A HIGH YIELD FABRICATION PROCESS
FOR MEMS BASED RESONANT MASS SENSORS
FOR CELL DETECTION APPLICATIONS

A THESIS SUBMITTED TO
THE GRADUATE SCHOOL OF NATURAL AND APPLIED SCIENCES
OF
MIDDLE EAST TECHNICAL UNIVERSITY

BY

TAYLAN BERKİN TÖRAL

IN PARTIAL FULFILLMENT OF THE REQUIREMENTS
FOR
THE DEGREE OF MASTER OF SCIENCE
IN
MICRO AND NANOTECHNOLOGY

SEPTEMBER 2014

Approval of the thesis:

**DEVELOPMENT OF A HIGH YIELD FABRICATION PROCESS FOR
MEMS BASED RESONANT MASS SENSORS FOR CELL DETECTION
APPLICATIONS**

submitted by **TAYLAN BERKİN TÖRAL** in partial fulfillment of the requirements
for the degree of **Master of Science in Micro and Nanotechnology Department,**
Middle East Technical University by,

Prof. Dr. Canan Özgen

Dean, Graduate School of **Natural and Applied Sciences**

Prof. Dr. Tayfun Akın

Head of Department, **Micro and Nanotechnology, METU**

Assoc. Prof. Dr. Haluk Klah

Supervisor, **Electrical and Electronics Engineering Dept., METU**

Examining Committee Members:

Prof. Dr. Tayfun Akın

Electrical and Electronics Engineering Dept., METU

Assoc. Prof. Dr. Haluk Klah

Electrical and Electronics Engineering Dept., METU

Asst. Prof. Dr. Kıvanç Azgın

Mechanical Engineering Dept., METU

Dr. Fatih Koçer

Electrical and Electronics Engineering Dept., METU

Dr. Said Emre Alper

MEMS Research and Application Center, METU

Date:

05.09.2014

I hereby declare that all information in this document has been obtained and presented in accordance with academic rules and ethical conduct. I also declare that, as required by these rules and conduct, I have fully cited and referenced all material and results that are not original to this work.

Name, Lastname: Taylan Berkin TÖRAL

Signature:

ABSTRACT

DEVELOPMENT OF A HIGH YIELD FABRICATION PROCESS FOR MEMS BASED RESONANT MASS SENSORS FOR CELL DETECTION APPLICATIONS

Töral, Taylan Berkin

M. S., Department of Micro and Nanotechnology

Supervisor: Assoc. Prof. Dr. Haluk Külâh

September 2014, 132 pages

This thesis reports the development of a high yield fabrication flow for MEMS based resonant mass sensors for cell detection applications. The basic design is a gravimetric resonator for real-time electronic detection of captured cells through bioactivation on gold coated active area which assures an antibody based cell capture inside a biocompatible microfluidic channel. The proposed design is demonstrated to have various advantages over its conventional counterparts. However, the yield of the previous fabrication methods is too low. Thus, the primary objective of this thesis is to increase the throughput efficiency of the fabrication process flow.

For this purpose, the resonator design layouts are improved without considerable geometry modifications compared to the previous generation designs. The original resonator devices make use of capacitive comb drive fingers with wide proof mass area, and folded spring beam structure as anchor structures. Correspondingly, in this thesis, the proposed design deviates only in the manner of dimensions in order to

increase the performance and endurance of the devices. Besides, the newly designed resonators are spanning a wider margin with respect to the bioactive area on the proof masses. The new designs differ from $44 \times 16 \mu\text{m}^2$ to $248 \times 128 \mu\text{m}^2$; and the natural resonance of these resonators start from 220 kHz and vary up to 1.47 MHz.

Secondly, the fabrication method is remodeled with the aim of decreasing the number of process steps and possibly simplifying every process step. In the new fabrication flow, the improvement of process yield is achieved, after the destructive process steps such as wet processes on suspended devices are eliminated. Many of these wet process steps can be avoided; but still some of these destructive wet processes, can only be replaced with analogous dry processes.

The major advantage of the design is the hydrophobic parylene coating in between fingers and springs of the resonators which avoids fluid penetration and thus, increases the resonators' performance considerably inside liquid flow. The hydrophobic parylene layer is required to be coated after the resonators are released and then, the bioactivation field needs to be cleared properly. Therefore, a novel method is developed for dry patterning which ensures the proper removal of the parylene on top of gold bioactivation site for keeping the thin parylene layer only on the fingers and anchors of the resonators.

Additionally, the previous generation fabrication flows are inspected, and advantages and disadvantages of these designs are discussed by taking fabrication achievements, design trade-offs, and yield considerations into account. The new fabrication method is presented under the light of these facts. In this way, with a new fabrication approach, the yield of the fabrication is fruitfully benefited that the working devices are increased from 5% to 90%.

Keywords: Resonant mass sensor, MEMS, parylene, hydrophobic coating, yield improvement, resonator, fabrication of suspended structures, cell detection.

ÖZ

HÜCRE ALGILAMA UYGULAMALARI İÇİN MEMS TABANLI YÜKSEK RANDIMANLI REZONANT KÜTLE SENSÖRÜ FABRİKASYON METODU GELİŞTİRİLMESİ

Töral, Taylan Berkin

Yüksek Lisans, Mikro ve Nanoteknoloji Bölümü

Tez Yöneticisi: Doç. Dr. Haluk Külâh

Eylül 2014, 132 sayfa

Bu tezde, MEMS teknolojisine dayanan ve hücre algılama uygulamalarında kullanılacak biçimde tasarlanmış bir rezonant kütle algılayıcısı için yüksek verimli bir üretim metodu sunulmuştur. Esas tasarım, antikor kullanılarak aktifleştirilmiş altın yüzey üzerinde tutundurulan hücrelerin, biyo uyumlu bir kanalın içinde yerleştirilmiş halde, gerçek zamanlı elektronik okuma devresi kullanılarak algılanmasını sağlayan bir gravimetrik rezonatördür. Bu tasarımın, benzer amaçlı ürünlere karşı önemli üstünlükleri daha önceki çalışmalarda ortaya konmuştur. Ancak, bu tasarım önceki üretim yöntemleri ile üretildiğinde, ürün verimi çok düşük sınırlarda kalmaktadır. Bu doğrultuda, çalışmanın temel amacı, fabrikasyon işlem akışının genel üretim verimliliğini artırmaktır.

Bu hedefe yönelik olarak, önceki nesil tasarımlara göre köklü geometri değişiklikleri yapılmaksızın rezonatör tasarımı iyileştirilmiştir. Orijinal rezonatör tasarımı, kapasitif tarak parmakları ile sürülen, katlı yay tutucuları ile sabitlenen ve merkezde

geniş bir kütle alanına sahip bir yapıdır. Buna bağlı olarak, bu tezde önerilen yeni tasarım, esas tasarıma göre sadece boyutsal olarak farklılık göstermektedir ve bu sayede rezonatörlerin performansı ve dayanıklılığı artırılmıştır. Rezonatör kütle alanı üzerinde oluşturulan biyo aktif alanlar, yeni tasarlanan rezonatörler için $44 \times 16 \mu\text{m}^2$ ile $248 \times 128 \mu\text{m}^2$ aralığında değişmektedir; ayrıca rezonatörlerin doğal rezonans frekansları 220 kHz ve 1.47 MHz frekans değerleri aralığında farklılık göstermektedir.

İkincil olarak, üretim sürecindeki işlem aşamaları azaltılarak ve olabildiğince basitleştirilerek, fabrikasyon metodu yeniden kurgulanmıştır. Yeni üretim sürecinde, serbest askıda duran parçalar üzerinde yapılan ıslak işlemlerin ortadan kaldırılması sonucunda gelişme sağlanmıştır. Bu tip ıslak işlemlerin bir kısmı doğrudan elenebilir; ama bazılarının yerine sadece denk işlevde kuru işlemler geçirilmelidir.

Geliştirilen tasarımın en önemli atılımı, rezonatör parmakları arasına kaplanan hidrofobik parilen katmanı ile parmakların arasına sıvı sızmasının önlenmesi ve böylece sıvı akışı altında çalışma performansının açık biçimde artışının sağlanmasıdır. Hidrofobik parilen katmanı, ancak rezonatör yapıları serbest hale geldikten sonra kaplanabilir ve bu aşamadan sonra biyo aktif kütle alanının üst yüzeyi tekrardan temizlenmelidir. Bu amaçla, bu aşamada kullanılan ıslak işlemin yerine, yeni bir kuru aşındırma yöntemi önerilmiştir. Bu yöntem ile parilen rezonatör parmakları ve tutucuları arasına kaplanırken, merkez kütle üzerindeki aktif altın yüzeyinin açık kalması sağlanmaktadır.

Önceki nesil üretim metodları; üretim başarıları, kayıpları ve verimlilik esaslarında artı ve eskilerine göre irdelenmiştir. Yeni önerilen fabrikasyon metodu, bu tecrübelerin ışığında belirlenmiştir. Böylece yeni bir üretim yaklaşımıyla, rezonatörlerin fabrikasyon verimi %5 seviyesinden %90 seviyelerine çıkartılmıştır. Ayrıca, daha önce sunulan rezonatörlerle benzer veya daha iyi performans gösteren cihazlar üretilmiştir ve bu rezonatörlerin sıvı içinde çalışma becerisi gösterilmiştir.

Anahtar Kelimeler: Rezonant kütle sensörü, MEMS, parilen, hidrofobik kaplama, üretim verimliliği arttırımı, rezonatör, serbest askıda yapıların üretimi, hücre algılama.

*To my family,
to my grandmother,
and to my love...*

ACKNOWLEDGEMENTS

I would like to express my deep gratitude to my thesis advisor, Assoc. Prof. Dr. Haluk Klah, for the support and guidance he gave me during my graduate study. I would also like to thank Prof. Dr. Tayfun Akın for his contribution and support during my thesis studies and the opportunity offered me by the METU MEMS facility during my MS studies.

I am particularly grateful to my colleague Mustafa Kangl for his contributions to the electronics interface part of the project and this thesis study, both in the design and testing phases and also accompanying me in long cleanroom hours. I would also like to thank Deniz Erođlu and Ekrem Bayraktar for developing the earlier generation process flows and fabrication of the first generation resonators.

My special thanks go to Mert Torunbalcı for his many helps during the fabrication and staying in the cleanroom in prolonged off hours to help me finish my process steps. I would also like to thank Dr. Said Emre Alper for his priceless contributions during all the bottlenecks I encounter. I feel highly in debt to Orhan Akar for sharing his deep knowledge on microfabrication and for his helps in the cleanroom.

I am especially thankful to all my colleagues in the BioMEMS and PowerMEMS groups. I would also like to recognize all the past and present members of the METU MEMS research group members, TAUB and TADB employees for their valuable friendship and kind helps in and out of the cleanroom.

Finally, I am grateful to my parents, Esmâ Demet Őener and İlker Tral for their precious support, enforcement and unconditional parenting through my life. Last but not least, I thank my love, Beyza Avcı, for her passionate aid and comfort. I could not have done it without them.

TABLE OF CONTENTS

| | |
|---|------|
| ABSTRACT..... | v |
| ÖZ | vii |
| ACKNOWLEDGEMENTS | x |
| TABLE OF CONTENTS..... | xi |
| LIST OF TABLES | xiii |
| LIST OF FIGURES | xiv |
| CHAPTERS | 1 |
| 1 INTRODUCTION..... | 1 |
| 1.1 Introduction to BioMEMS..... | 2 |
| 1.2 BioMEMS Methods for Cell Detection..... | 4 |
| 1.3 Mechanical Detection..... | 6 |
| 1.4 Gravimetric Detection for Cell Sensing | 9 |
| 1.4.1 Controlling Damping | 18 |
| 1.5 Research Objectives and Thesis Organization | 20 |
| 2 THEORY & DESIGN..... | 23 |
| 2.1 Gravimetric Detection | 23 |
| 2.1.1 Damping Mechanisms..... | 26 |
| 2.1.2 Resonator Damping Model | 28 |
| 2.2 Resonator Detection Capabilities | 32 |
| 2.3 Resonator Design..... | 35 |
| 2.3.1 Folded Spring Beams | 38 |
| 2.3.2 Hydrophobic Parylene Coating | 40 |
| 2.4 FEM Simulations..... | 42 |
| 2.5 Design Determinations | 44 |
| 2.6 Design and Simulation Summary | 49 |

| | | |
|-------|---|-----|
| 3 | FABRICATION | 51 |
| 3.1 | Previous Generation Process Flows | 53 |
| 3.1.1 | First Generation Process Flow | 55 |
| 3.1.2 | Second Generation Process Flow | 59 |
| 3.1.3 | Third Generation Process Flow | 64 |
| 3.1.4 | Problems with the Previous Generation Process Flows | 69 |
| 3.2 | New (4 th) Generation Process Flow | 77 |
| 3.3 | General Remarks on the New (4 th) Generation Process Flow | 89 |
| 3.4 | Fabrication Summary | 92 |
| 4 | EXPERIMENTAL RESULTS | 95 |
| 4.1 | Parylene Cleaning Except on the Inner Bioactivation Gold Sites..... | 95 |
| 4.2 | Interface Circuit | 103 |
| 4.3 | Test Results..... | 106 |
| 4.4 | Fabrication Yield | 114 |
| 4.5 | Fabrication Yield Results and Summary | 115 |
| 5 | CONCLUSION AND FUTURE WORK | 119 |
| | REFERENCES..... | 123 |

LIST OF TABLES

TABLES

| | |
|---|-----|
| Table 2.1: Geometric parameters of different resonator designs in the previous generation designs. All dimensions are in μm , if it is not mentioned..... | 46 |
| Table 2.2: Geometric parameters of all resonator designs in the final generation (4 th generation) designs. All dimensions are in μm , if it is not mentioned. | 48 |
| Table 4.1: Average values for the percentage of the EDS analysis for 3 different location intervals. The values are average of 5 measurements each for 6 dies (30 measurements)..... | 100 |
| Table 4.2: Comparison for the resonator controlling designs with the previous generation fabrications..... | 111 |

LIST OF FIGURES

FIGURES

Figure 1.1: Dimensional scale of nanotechnology and MEMS with respect to the biological field of interest [4]..... 2

Figure 1.2: The schematic view of the micro-cantilever design is proposed. Each detector consists of two cantilevers with monolayer biological agents are coated and clean cantilever as control group [26]. 7

Figure 1.3: (a) Schematic view of the cantilever array for bio-analyte attachment with resistive sensing of the piezoresistor embedded on the cantilevers. One of the cantilevers is not activated so differential signal is monitored. (b) The SEM image of the cantilever array of 32 piezoresistive microcantilevers arranged inside the microfluidic channel is shown [27]. 8

Figure 1.4: (a) SEM image of the fabricated biosensor with a square bulk biosensor. (b) The measurement setup of differential drive and sense ports is shown [32]. 9

Figure 1.5: The schematic view of the cantilever resonator with a monolayer of bio analytes on the upper side is shown. When, the cantilever oscillates, the average displacement signal arises from the surface stress can be inspected. Fluctuations that are analyzed in the frequency domain determine the resonance frequency and quality factor (Q). The elasticity and mechanical losses of the cantilever are modeled by a spring and a damper placed in parallel with a smaller biological layer modeled similarly as another spring and damper in addition [36]. 11

Figure 1.6: (a) Schematic view of the “checker-mode” resonator, and (b) three possible electrode configurations; top checker patterned electrodes, top checker patterned electrodes with full bottom ground electrode, and the checker patterned electrodes are placed on top and bottom are shown. Finally, (c) the resonant

| | |
|--|----|
| frequency of checker-mode resonator after coating 12 PEMs bilayers are shown [38]. | 12 |
| Figure 1.7: (a) The probe geometry for the fine sensing, and (b) the optical image of the probe is shown. The base length L , of the cantilever is made of p-doped silicon and the L_l length is the ZnO active material coated with Ti/Au. (c) and (d) show the natural resonance shift of the sensor before (blue) and after (red) the adsorption of enzyme molecules [39]. | 13 |
| Figure 1.8: Schematic drawing of the principle of operation of a cantilever with microchannel embedded inside. (a) Mass of flowing particles is measured using resonance peak shifts over time under continuous flow of biomolecules, cells or synthetic particles. (b) While bound and unbound molecules both increase the mass of the channel, that bind to the channel wall accumulate inside the device. (c) Another measurement of particles flow through the microchannel of the cantilever without binding to the surface, and the detected signal changes with the position along the channel [41]...... | 15 |
| Figure 1.9: (A) Sensor schematic with the first mode of resonance is shown with the mass sensitivity normalized to its maximum value. (B) SEM image showing sensor array and (C) measurement setup are presented. (D) Finally, the frequency response of the sensor with cell attachment (orange), and without (blue) cell attachment are shown [44]...... | 17 |
| Figure 1.10: Schematic of the resonator and water droplet containing streptavidin spotted on the center of biotin modified resonator far from the surrounding electrodes. [46]..... | 17 |
| Figure 1.11: (a) Schematic view of the U-shaped groove cantilever etched in a SiN membrane, (b) cross sectional view of the trapping with the meniscus formation on the bottom of the groove is shown. (c) The resonance spectrum measurements are shown in air, and (d) after partial wetting under DI water is applied [48]...... | 19 |
| Figure 2.1: Schematic view of second order mass and loaded biological entity with two parallel spring and damper systems. | 24 |
| Figure 2.2: The representations of microfluidic flows; (a) Couette flow, and (b) Poiseuille flow [63]...... | 29 |

| | |
|--|----|
| Figure 2.3: Schematic view of the overlapping parallel comb finger capacitors is shown. | 32 |
| Figure 2.4: Schematic view of (a) resonant mass sensor embedded into the microchannel, and (b) 3-D representation of microfluidic channel and the bioactivation functionalized on the proof mass gold active area. | 36 |
| Figure 2.5: Schematic view of double folded beam and finger geometries of the resonator with design parameters are denoted. | 38 |
| Figure 2.6: The schematic cross sectional view of the resonator comb finger is shown with Parylene-C is conformably coated on the suspended components. Thus, the surface thermodynamic interfacial energy keeps the liquid without any penetration [69]. | 41 |
| Figure 2.7: The quality factor improvement with parylene coating on the resonator fingers is shown as a comparison with resonance characteristics of bioresonator in air, after parylene coating and uncoated performance in water [69]. | 42 |
| Figure 2.8: Fundamental vibration mode of design RES#1 at 1.47 MHz. | 43 |
| Figure 2.9: The buckling of the resonators are simulated for gravitational forces. The maximum buckling displacement at the middle of the proof mass is measured to be 0.1 pm. | 44 |
| Figure 3.1: First Generation Process Flow. | 56 |
| Figure 3.2: Illustration of DRIE Notch Effect [74]. | 58 |
| Figure 3.3: Second Generation Process Flow. | 61 |
| Figure 3.4: PDMS Microchannel Preparation for Second Generation Process Flow. | 62 |
| Figure 3.5: Third Generation Process Flow. | 64 |
| Figure 3.6: SEM image of the 3 rd generation resonator device after DRIE structure is etched. | 67 |
| Figure 3.7: Broken wafer for the inspection of DRIE etch profile optimization trials for the prevention of the notching effect. | 70 |
| Figure 3.8: Active silicon layer is not etched completely and the resonators are not formed properly with under etch in DRIE. | 70 |
| Figure 3.9: Remaining silicon residue after DRIE etch on the varying etch spaces without optimization. These residues are the counter issue for the notching effect which cause loss of the resonator finger and anchor structures. | 71 |

| | |
|---|----|
| Figure 3.10: Proper etch on the corner sites of the anchor and fingers after optimizations are done for the specific structure mask of the resonator features. | 71 |
| Figure 3.11: After anodic bonding due to floating areas on the bond surface, high rate of burning and sparking between fingers of the resonators and metal lines, resulting in huge amount of loss of the contacts and resonators..... | 72 |
| Figure 3.12: (a) Metal routing lines mask can be seen, the die level metal lines are not connected so at the state of the anodic bonding, there are many floating pads remaining on the active silicon layer of the SOI and this results in sparking during the anodic bonding. (b) Metal routing lines mask can be observed for the 4th generation flow, the die level metal lines are all connected in the new design. Also there are no floating areas remaining. | 73 |
| Figure 3.13: Rupture oxide regions above bond pads after backside DRIE. [71] | 74 |
| Figure 3.14: After the lithography, photoresist penetrated the oxide layer through microfractures marked with red throughout the wafer and again rupture the oxide layer after the baking step. | 75 |
| Figure 3.15: Chromium is etched under long oxygen plasma steps for photoresist strip and the bioactivation gold site on top of proof mass of the resonators are lifted off. | 76 |
| Figure 3.16: BHF release wet etch undercut the bond sites glass and the weak spots like gold connection areas are vulnerable for breakage. | 76 |
| Figure 3.17: New Generation Process Flow. | 77 |
| Figure 3.18: Bioactivation metal patterned on clean SOI active layer silicon side. .. | 80 |
| Figure 3.19: SOI active layer structure DRIE etch lithography..... | 80 |
| Figure 3.20: SEM inspection of SOI active layer structure DRIE etch on the test resonator..... | 81 |
| Figure 3.21: Recess etch Cr/Au metal masking layer with Au and Cr layers are etched. The resonator sites and the tips of the drive, sense and ground lines can be seen..... | 82 |
| Figure 3.22: Recess etch on the glass wafer with metal masking for pure HF wet etch with 5 μm deepness after the Cr/Au metal masking layer is stripped..... | 82 |

Figure 3.23: The general top view of the resonator mask steps for process flow 3rd generation. The blue lines show the recess gaps and the metal lines that will be carved inside the glass wafer..... 83

Figure 3.24: Microchannel carved inside on the recess patterned glass wafer with 50 μm deep and not more than 170 μm wide..... 84

Figure 3.25: Microchannel carved inside on the recess patterned glass wafer with routing metal lines and wire bond pads are patterned..... 85

Figure 3.26: Resonator sites can be seen after anodic bonding. The microchannel is carved inside the glass wafer and the bioactivation gold layers are appearing on the resonators. Sparking is not occurring between fingers of the resonators and it does not burn off the contact lines..... 87

Figure 3.27: After the DRIE backside handle layer removal and BHF release are done. The BHF over etch can be observed around pad contact areas..... 88

Figure 3.28: Gold residues between the fingers and DRIE etch sites due to penetration challenge of the metal wet etchants in between deep DRIE trenches. 90

Figure 3.29: The bioactivation structures compared under SEM, (a) the twisted edges can be easily observed with lift-off patterning; and on the other hand, (b) the metal etch over etch of the gold sites with increased diffused gold etch times. Cr under the gold bioactive sites can be observed. 91

Figure 3.30: The spin coating of photoresist with cavities on the field create some trenches under HF wet etch and then at the next spin coating steps, the metal routing lines become trimmed and even become discontinuous. 92

Figure 3.31: SEM image of resonant mass sensor device with bioactivation gold is standing on the proof mass of 4th generation process flow. 93

Figure 3.32: The photograph of resonant mass sensor device integrated with microfluidic channel cap and electrical connections in the 4th generation process flow. One of the input and output ports are mounted on the holes of the glass microchannel with white epoxy. 93

Figure 4.1: The view of the resonators can be observed after tape-check for observing the inner parylene coating thickness. (a) Parylene is coated and after oxygen plasma treatment the resonator finger side walls parylene coating still

remains in an aspect. (b) If the treatment increased the parylene layer becomes so thin that the SEM blur created cause of the insulation of parylene disappears..... 98

Figure 4.2: The field of interest with certain EDS analysis are done shown on the SEM image of the resonator after tape-check; inside the blue box is called “Middle” measurements, in between blue and red boxes is called “Edge” measurements and in between green and red boxes is called “Outer” measurements..... 99

Figure 4.3: The measurements for the thickness are not reliable but it gives information about the average thickness distribution. (a) The measurement of thickness of the parylene layer on the resonators from the top view before the oxygen plasma treatment is around 0.45 μm , after the oxygen plasma treatment (b) resonator coating thickness is dropped to 0.31 μm 101

Figure 4.4: The resonator devices are shown under optical microscope, (a) after parylene coating, (b) after parylene is etched with short oxygen plasma treatment. (c) and (d) are the focused images for parylene coated and plasma treated devices respectively. 102

Figure 4.5: Resonator measurement setup is shown, with the network analyzer, DC supplies, and the interface TIA circuit. The device is measured with the network analyzer under probe station. The measured devices and the read-out circuit with TIA interface integrated are identified in green circles. 105

Figure 4.6: The magnitude and phase measurements of (a) the resonator without coating and (b) with parylene coating are done for RES #7 device by direct observation of network analyzer. The shift of natural frequency is observed from 572.8 kHz to 563.2 kHz after parylene coating. 107

Figure 4.7: The capillary flow test is done with injecting DI water with syringe from one end of the microchannel and without any leakage water come out from the other end of the microchannel 108

Figure 4.8: The mass of parylene can be observed with shift of resonance peak of the gravimetric resonator sensor. The resonance frequency is shifted down from 229.3 kHz (green) to 221.5 kHz (red) and the quality factor is also decreased from 764.3 to 573.0. The resonator with parylene coating under fluid flow shows 221.6 kHz resonance frequency and the quality factor drop to 198.4. 109

Figure 4.9: The magnitude and phase components of the resonance characteristics of RES #1 design with $44 \times 16 \mu\text{m}^2$ proof mass area and with natural frequency of 806 kHz and quality factor of 289..... 112

Figure 4.10: The magnitude and phase components of the resonance characteristics of RES #13 design with $248 \times 128 \mu\text{m}^2$ proof mass area and with natural frequency of 232 kHz and quality factor of 862. 113

Figure 4.11: The wafer map with numerical representation of 64 dies with 14 different architectures of resonators are placed..... 116

CHAPTER 1

INTRODUCTION

The future of MEMS relies on the new efforts to develop micromachined components for the governance of microfluidic systems are just beginning to bear fruit. The biological opportunities on the MEMS field are expected as the driving factor for next decade [1]. When the sizes of the biosensors shrink to the cell level, the sensing of a living cell becomes the attracting field of interest where the rare cell detection which is specialized for selective sensing, trapping, isolation and inspecting the cell. The properties like mass, volume, density and deformability of living cell are required to be precisely measured with the new tools in hand. The integration of micropumps with microvalves and reservoirs to build new miniaturized biosensing and delivery systems are under radar for research [2].

This thesis is specialized on a certain kind of rare cell detection with a gravimetric resonator structure. Thus, the thesis will take a brief underline for the concept and focus on the cell detection applications particularly the mass sensing of the living cell in fluid environment.

In this chapter, BioMEMS is briefly explained, basically focusing on the cell detection applications with different detection methods. The proposed sensor is a gravimetric resonant biosensor, so the chapter is narrowed down to especially on gravimetric detection techniques for cell detection applications. At the end, yield tracking for MEMS fabrication process flows is also mentioned.

1.1 Introduction to BioMEMS

Biomedical Microelectromechanical Systems (BioMEMS) is defined as “devices or systems, constructed using techniques inspired from micro or nanoscale fabrication, that are used for processing, delivery, manipulation, analysis, or construction of biological and chemical entities” that Rashid Bashir famously stated [2]. Conventional commercial instruments for medical, biochemical, and genetic analysis perform a broad range of analytical functions but are generally bulky. The general aim to miniaturize all aspects of biochemical analysis is flourished with the concept of micrototal analysis system (μ TAS) or Lab on a Chip (LoC) system, which was introduced in 1989 by Manz [3]. The terminology makes little difference; the basic fact is the BioMEMS technology emerged from the requirement of achieving micrometer level medical laboratories. The biological analytes under the interest of biology and medicine; like cells, proteins or viruses, have micrometer or even nanometer level sizes. Thus, the transducer of the sensor device should also be at comparable sizes (See Figure 1.1).

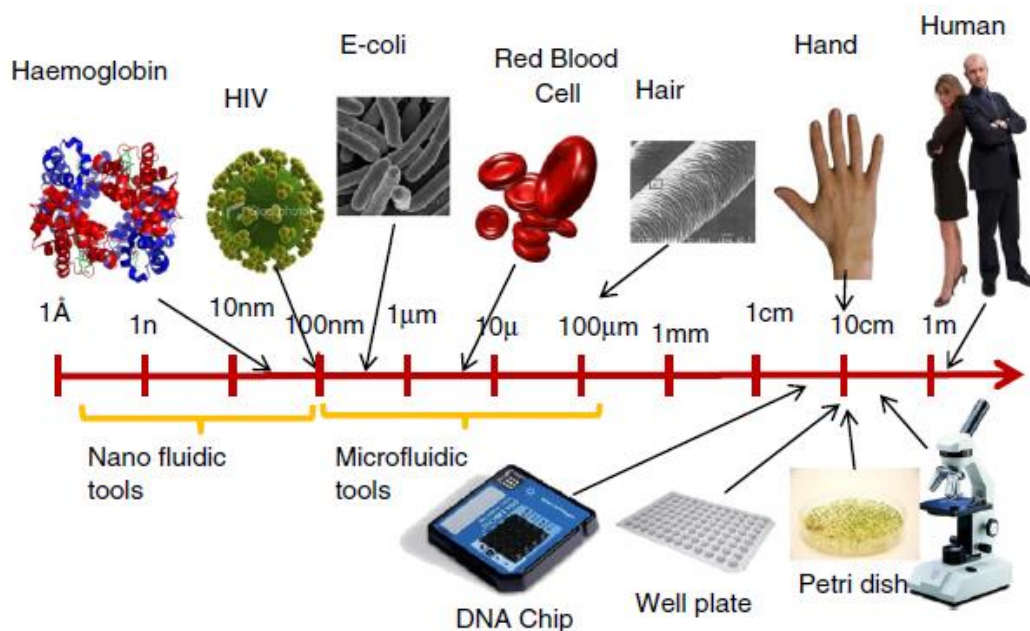


Figure 1.1: Dimensional scale of nanotechnology and MEMS with respect to the biological field of interest [4].

The major advantage of MEMS technology is the opportunity of designing and producing miniaturized systems. The shrinking of the sizes of operational devices is permitting the systems to be fabricated with low die budget, mass produce capability and lower power consumption. Likewise, these new micro level biodevices of BioMEMS decrease the manufacturing costs, increase reproducibility, enhance controllability, and also lower the sample size and the reagent use. The signal to noise ratio and response time improves with these micro devices. The other advantages are precise control of mixing, reaction rate, enhanced heat transfer, discarding waste products, enabled point of care diagnosis, improved safety with experiments and also possibility of embedded detection methods and high throughput rate [5].

BioMEMS devices are analytical devices that integrate a biosensitive factor with a physical or chemical transducer for selectively and quantitatively detect the biological compounds in a specified environment. μ TAS or LoC devices are used for delivery, processing, analysis, or detection of biological molecules and species [1]. These devices are used to detect cells, microorganisms, viruses, proteins, DNA and related nucleic acids, and small molecules of biochemical importance and interest.

The studies of BioMEMS can be separated into diagnostic and therapeutic devices [6]. The diagnostic systems study the analysis, separation, and characterization of the biological analytes [7], alternatively the therapeutic systems work on implantable biocompatible devices for the living organisms like implants [8], neural interfaces [9], and drug delivery systems [10].

Generally the BioMEMS devices are integrated with tubings and channels. Microfluidics operation is critical in order of the biological and medical analysis studies with examination samples in fluidic environments. The biocompatibility is critical with the microchannel in tube material or coating; due to the interaction with the biological elements in the fluid. PDMS (Polydimethylsiloxane) [11] and Parylene [12] patterned structures are both biocompatible and they are best fit for the microchannel fabrication of BioMEMS devices. Processing of BioMEMS devices using polymeric devices and soft lithography is very attractive due to increased

biocompatibility and easy fabrication, ability to integrate functional hydrogel materials, and low cost and rapid prototyping methods available in polymer based materials [13].

Cells consist of 70% water and the cell can not survive out of liquid environment for an adequate time. Among these advantageous properties of BioMEMS, the sensing and actuation of living cells under fluidic medium, mostly with water and blood is the prominent field. The recent emerges of the techniques of the BioMEMS enables us to detect under these targeted environments [14].

1.2 BioMEMS Methods for Cell Detection

The living cell detection is one of the most promising fields of BioMEMS which includes; ability to detect a specific cell inside a population of cells, and ability to deal with very small sized samples like even receptive biomolecules. These demands can be only solved with high sensitivity, high accuracy, high selectivity, and high throughput of cells under medium. Cellular analysis supports many fields including drug discovery, diagnostics, cancer research, regenerative medicine, system and synthetic biology, and renewable energy [1].

The implementation of microfluidic technologies in single cell analysis is one of the most promising approaches that not only offers information rich, high throughput screening but also enables the creation of innovative conditions that are impractical or impossible by conventional means. The possibilities for distinguishing the difference between individual cells and the benefits from miniaturization have led to many discoveries both in traditional biopharmaceutical communities and in emerging fields such as synthetic biology [3].

Physical applications of cell sorting and isolation are examined as the first elevation for the BioMEMS cell analysis applications. These applications are mostly fluidic setups with certain geometries and the separation of cells with respect to their volume, mass and density can be easily implemented as LOC apparatuses. In this way, size based capture and separation [15], identification and counting [16], with

geometry manipulations under changing flow, and electrophoresis and dielectrophoresis applications with the use of electrokinetic forces [17] are used for cell detection and analysis [18].

Although, these kinds of applications of BioMEMS show a great promise for the future with simple designs of biochips with microarray architectures; the transducer based biosensor applications create the possibility of straight to the point sensing [19]. The biosensor based devices stand on detection methods of BioMEMS which can be narrowed down to four fields; electrical [20, 21], electrochemical [22, 23], optical [24, 25], and mechanical detection [26, 27].

The electrical detection technique relies on the electrical impulse caused of current change due to conductance, impedance and RF parameter manipulations with the sensor. The method minimizes the sensing field and enables label free detection that the direct interaction between analyzed medium and the sensor is possible. In this way, the sensitive agent is directly attached to a transistor, a resistor of a MEMS circuit that measures the electrical parameters of the sample [13]. The electrical detection is similar to electrochemical detection without any chemical reactions taking place in the medium. The effect of conductance or impedance change is directly result from the change of the electrical characteristics of the analyte or in RF case, the analyte is placed so that the magnetic effect causes a disturbance of the permittivity or permeability.

The electrochemical sensors are very similar to the electrical sensing applications. The only difference is a chemical reaction is occurring on the site of sensing. This reaction causes a direct actuation for the biosensor in respect of current, voltage or conductance. The electrochemical detection of BioMEMS application mostly sense the redox reactions and changing ion concentration in the medium. The main advantage of the electrochemical detection is simplicity and though cheap applications for BioMEMS with label free detection. The electrical sensing without any complex analysis tool decrease the response time and even real time sensing is possible. On the other hand, the data analysis can be an issue with many chemical reactions other than desired sensing entity occurs at the same time which causes data

ambiguity. The solution is cross checking the data with other detection tools like optical or mechanical detection equipments for calibration or optimization.

Optical detection mechanism makes use of change of optical entities like UV absorption, luminescence, and reflectance [28]. Additionally, the interferometry is applied to bio-analytes for detection applications with the use of refractive index differentiations on the biosensitive thin film [29]. Many nowadays used monitoring device for medical applications are based on the optical detection mechanisms so the background of these applications is well defined and most of the BioMEMS optical applications are miniaturized systems with similar working principles with the original counterparts. Nonetheless, optical biosensors offer several advantages such as sensitivity, flexibility, resistance to electrical noise and high stability. Actually, the bulky structure of the optical sensing setup with extra observation tools required, the area gives space for new novel designs.

In this thesis the proposed design is a gravimetric sensor so focus is on the mechanical detection mechanisms for biosensor based rare cell detection applications.

1.3 Mechanical Detection

The mechanical detection techniques rest ground on stress and mass detection techniques. The cantilever structures are the main component for the widely used mechanical detection applications for BioMEMS. The bending of the cantilever is the transducing factor measured with the help of position detector like AFM or laser or electrical means like piezoresistor established on the cantilever. Stress sensitivity of the cantilever is inversely proportional to the spring constant while the overall surface of the cantilever determines the number of molecules that can attach to the surface to cause a resulting stress change. The change is measured with the resonance characteristics of the design at this time [5]. Cantilever based systems are capable of real-time, multiplexed detection of unlabeled disease markers in extremely small volumes of samples. Nowadays fabrication techniques will allow the integration of electronic readout and sample introduction into a single unit,

decreasing the device size, detection time, and cost. Biosensor technologies based on fabricated cantilever arrays involving multiple cantilevers, electronic processing, and even local telemetry on a single chip have the potential of satisfying the need for highly sensitive and selective multiple-target detection in very small samples.

The design of the cantilever array structure is a label free surface stress sensor with two identical sensors with one of them is working as a reference detector [26]. The other detector is coated with self-assembled monolayer of binding agents (See Figure 1.2). Also, the study examines the appropriate biocantilever with comparative study of Si, AlN, SiN and PMMA (Polymethylmethacrylate); and found out that the higher sensitivity and biocompatibility lead to PMMA is the suitable material for this application. The system is also tested for self-assembly monolayer of yeast cells.

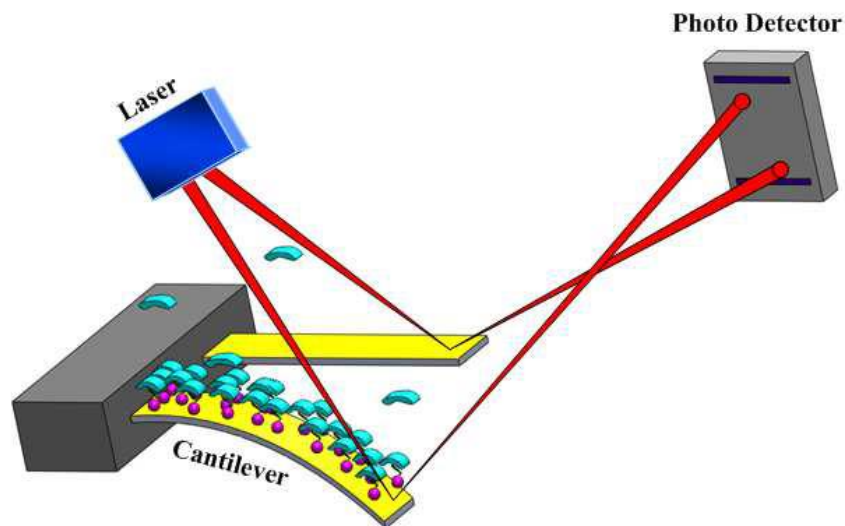


Figure 1.2: The schematic view of the micro-cantilever design is proposed. Each detector consists of two cantilevers with monolayer biological agents are coated and clean cantilever as control group [26].

Another study focuses on the instrumentation of the piezoresistors fabricated on silicon micro cantilevers and measuring the bending of the cantilever array [27]. A minimum detectable surface stress change of 2.6 mN/m is measured with immobilization of single stranded thiol modified DNA oligonucleotides (See Figure 1.3). Also, it is demonstrated that analyze of two samples simultaneously by utilizing

the laminar flow in the microfluidic channel system with controlled directionality is possible.

The mechanical biosensors are also fabricated with different base materials like thin membrane of PDMS with bi-membrane concept [30]. The study shows a low cost design with easy fabrication steps for a large active functionalization area for biological analyte binding and the bending of the PDMS is sensed by a capacitor which one electrode is placed on the PDMS membrane and the other onto the base substrate. The stress based sensors are further reviewed by the study of Sang *et al.* [31] in detail with state of the art applications.

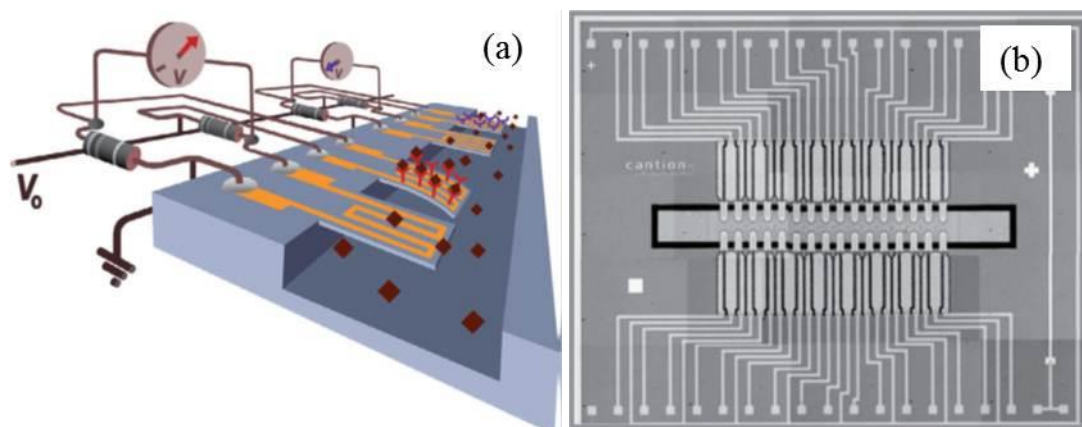


Figure 1.3: (a) Schematic view of the cantilever array for bio-analyte attachment with resistive sensing of the piezoresistor embedded on the cantilevers. One of the cantilevers is not activated so differential signal is monitored. (b) The SEM image of the cantilever array of 32 piezoresistive microcantilevers arranged inside the microfluidic channel is shown [27].

The second portion of mechanical biosensors senses the mass of the analyte directly with shift of the resonance characteristics of the resonator structure. In the study [32], Heidari *et al.* present the a biosensor with a micromachined silicon squared plate that is excited in the Lamé bulk acoustic resonant mode at a frequency of 37.8 MHz, and with quality factor of 10,000 and the mass sensitivity of 400 Hz/pg (See Figure 1.4).

In another study by Liu *et al.* [33] the biosensor system includes two biosensing techniques; resonant frequency measurements and electric cell substrate impedance sensing (ECIS) on a single device. The double sensor system integrates the upper

electrode of a quartz crystal microbalance (QCM) resonator and a active site as working microelectrode for ECIS technique. The hybrid device is successfully used for Bovine aortic endothelial live cells. This method can be implemented to water toxicity detection apparatuses. Likewise, the study of Huang *et al.* [34] is based on QCM resonators which are used as a maize chlorotic mottle virus biosensor is compared to the commercial enzyme linked immunosorbent assay (ELISA) test methods. Moreover, in the study of Gruhl *et al.* [35], the surface acoustic wave (SAW) biosensor is used for label free detection of Penicillin G in milk and the system gives satisfactory results for commercial limits of European Commission.

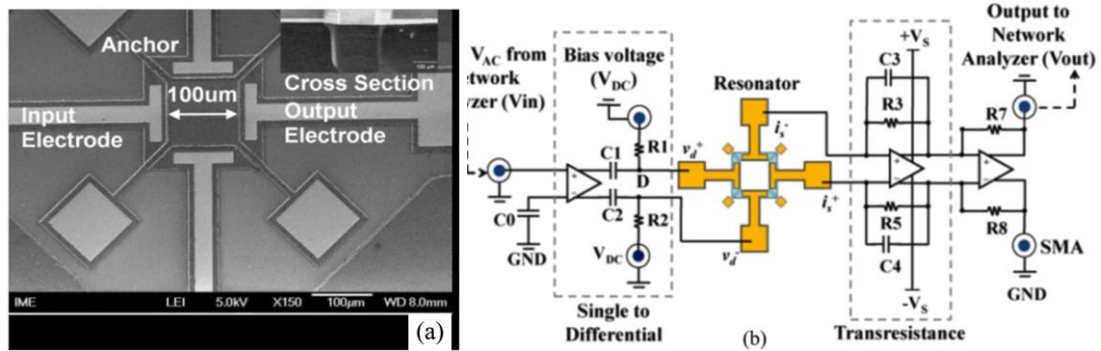


Figure 1.4: (a) SEM image of the fabricated biosensor with a square bulk biosensor. (b) The measurement setup of differential drive and sense ports is shown [32].

1.4 Gravimetric Detection for Cell Sensing

The gravimetric detection technique is one of the sub topics of mechanical detection related with the mass detection. Briefly, the gravimetric detection technique depends on the change of resonance frequency of an oscillating mass, when the resonator mass changes. When extra mass is added on the oscillating structure, the natural frequency of the resonator alters [36]. Actually, the damping coefficient and the spring constant of the gravimetric resonator system also change when a mass is added on the proof mass of the resonator. However, the change caused by this loading can be considered negligible for most of the applications. The relationship between the natural resonance frequency (f) and the resonator mass (m) is given in

Equation (1.1), where k is the spring constant of the resonator. Also, the mass change can be calculated from the relation between resonator shifted frequency (f_i) and the initial unloaded natural frequency (f_0) as seen in Equation (1.2). The quality factor (Q) of the resonance characteristic can be defined as in Equation (1.3). The basic cantilever operation as a gravimetric sensor is explained in Figure 1.5.

As mentioned for mechanical detection applications, the gravimetric technique also relies mostly on cantilever structures. However, other kinds of resonator structures are starting to arouse interest for the past decade [37]. Generally, the operation principle of the gravimetric sensor is that the resonator is driven at its resonance frequency where the resonance dynamic response amplitude is at its peak. The driving methods include piezoelectric actuators, magnetic forces, and light-induced forces.

$$f = \frac{1}{2\pi} \sqrt{\frac{k}{m}} \quad (1.1)$$

$$\Delta m = \frac{k}{4\pi^2} \sqrt{\frac{1}{f_i^2} - \frac{1}{f_0^2}} \quad (1.2)$$

$$Q = \sqrt{3} \frac{f_0}{\Delta f} \quad (1.3)$$

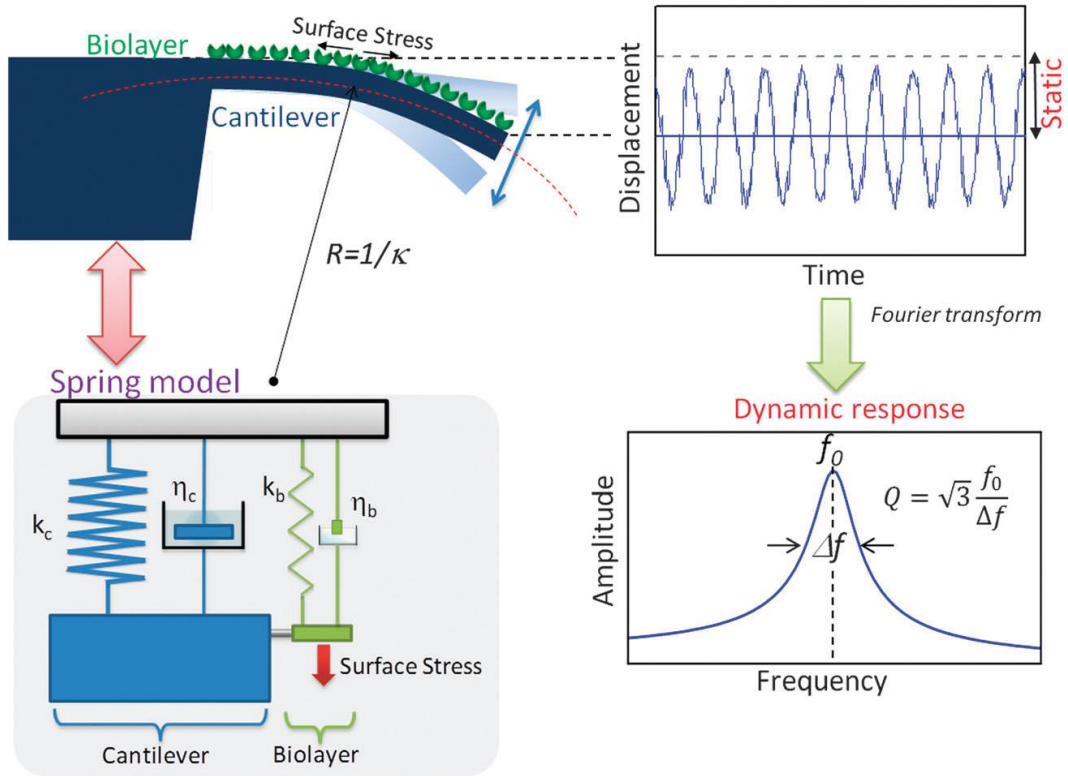


Figure 1.5: The schematic view of the cantilever resonator with a monolayer of bio analytes on the upper side is shown. When, the cantilever oscillates, the average displacement signal arises from the surface stress can be inspected. Fluctuations that are analyzed in the frequency domain determine the resonance frequency and quality factor (Q). The elasticity and mechanical losses of the cantilever are modeled by a spring and a damper placed in parallel with a smaller biological layer modeled similarly as another spring and damper in addition [36].

The cell detection applications require high degree of sensitivity for perceiving very low amount of mass changes. The gravimetric detection with high performance resonator based designs show that detection of even one cell with high precision of the mass amount quantitatively and selectively. Thus, the gravimetric detection becomes the promising field of interest, and is successfully used for rare cell detection among much different cell diversity.

The PZT based piezoelectric gravimetric biosensors have the high detection performance for rare cell detection applications. In the study of Heidari *et al.* [38] a AlN piezoelectric resonator with checker patterned electrode is fabricated for mass

sensing applications (See Figure 1.6). Three different electrode architectures are shown in the schematic differing for the placement of electrodes on the top side, both sides, and the ground electrode addition to the backside. The device shows a mass sensitivity of $175 \mu\text{m}^2/\text{ng}$ and $18.7 \text{ ng}/\text{cm}^2$ detection limit when polyelectrolyte multilayer (PEM) polymer is coated on the resonator structures and then, the resonance shift is monitored [38].

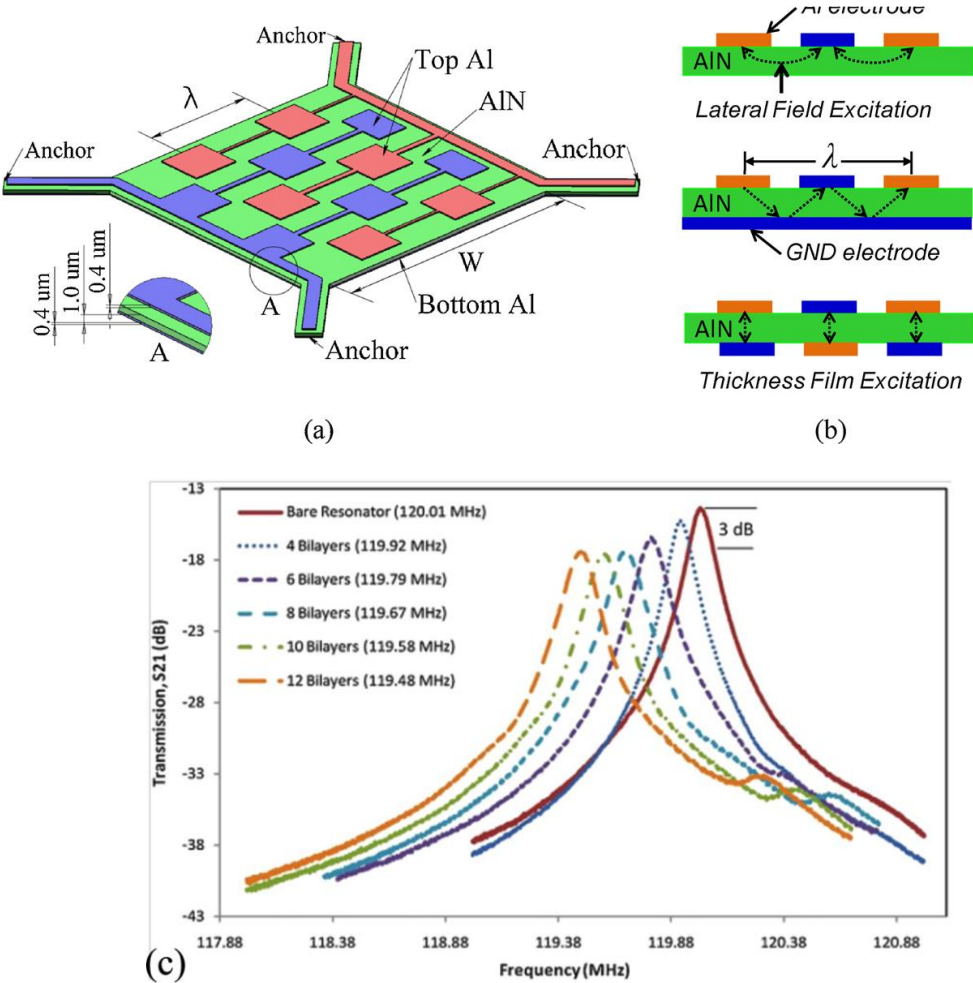


Figure 1.6: (a) Schematic view of the “checker-mode” resonator, and (b) three possible electrode configurations; top checker patterned electrodes, top checker patterned electrodes with full bottom ground electrode, and the checker patterned electrodes are placed on top and bottom are shown. Finally, (c) the resonant frequency of checker-mode resonator after coating 12 PEMs bilayers are shown [38].

In another study, based on the Euler-Bernoulli Beam Theory, a PZT gravimetric cantilever geometry is applied to very small mass sensing in the means of enzyme molecules immobilized on the sensor surface [39]. The design geometry and the sensitivity results are shown in Figure 1.7. Finally, a wireless magnetoelastic gravimetric sensor is developed for sensing Salmonella cell cultures, which is a kind of biological contamination for tomato [40]. The system can be used for level of contamination on site and real time.

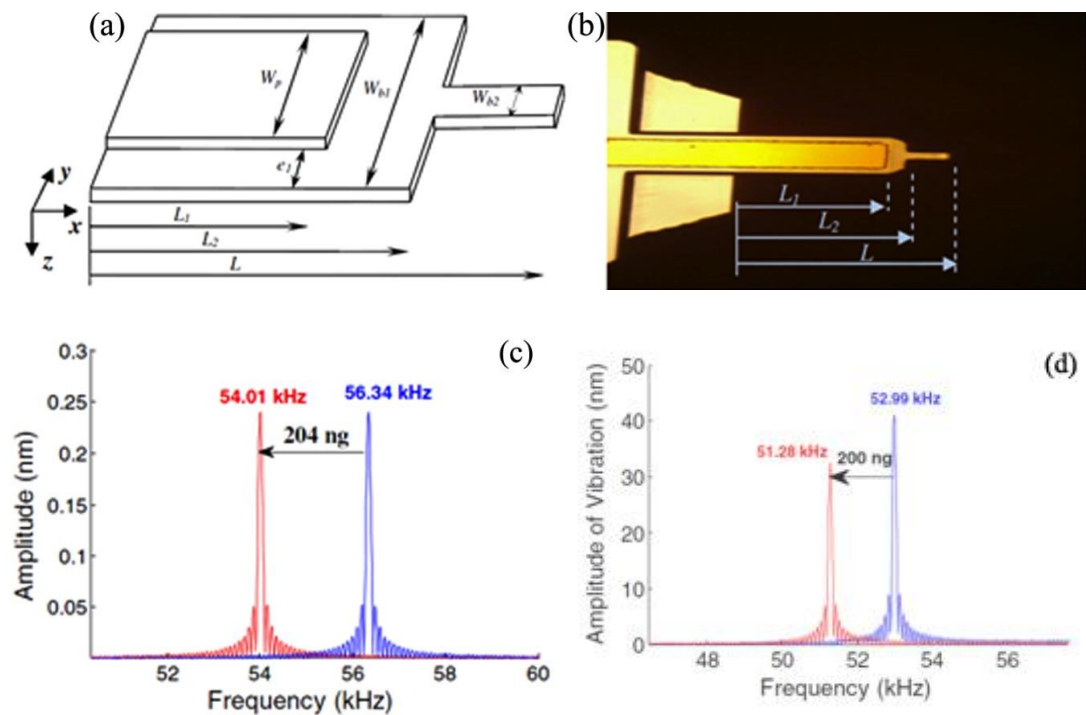


Figure 1.7: (a) The probe geometry for the fine sensing, and (b) the optical image of the probe is shown. The base length L , of the cantilever is made of p-doped silicon and the L_1 length is the ZnO active material coated with Ti/Au. (c) and (d) show the natural resonance shift of the sensor before (blue) and after (red) the adsorption of enzyme molecules [39].

One of the leading studies in the field of gravimetric rare cell detection was presented by Burg et al. [41]. The resonator cantilever structure includes the microchannel inside the suspended structure. The working principle is that the solution flows in the channel embedded hollow resonator and the cantilever can work under vacuum environment for achieving high resonance quality factor. The group

demonstrates that by using suspended microchannel resonators, even single biological nanoparticles, bacterial cells and sub-monolayers of adsorbed proteins can be identified inside DI water. The structure and the measurement procedure is explained briefly in Figure 1.8. Also, resolution at the level of femtograms is reported with less than 1 Hz measurement bandwidth. The working opportunity under vacuum eliminate also the air damping issue, and it is shown that the viscous fluid damping is negligible compared to inner dissipation of energy inside cantilever microchannel. However, this method is not applicable for medium sized cells and other particles, that the cells will be stuck inside the microchannel because of crowdedness.

Another study by Poshtiban *et al.* [42], presents a microresonator array platform that uses phage tail spike proteins as a recognition probe. This array is composed of one thousand active beams in 13.5 mm² area for high capture rate of bacteria cells. The resonators have natural frequency at 1.095 ± 0.005 MHz and minimum mass sensitivity of 52 fg. This device demonstrates the usage of these beams with specific detection of the *Campylobacter jejuni* cells after immobilization of devices with phage GST-Gp48 tail-spike proteins. On the other hand, the functionalized device active areas do not show any sensitivity to *Escherichia coli* bacteria which confirms the specificity of the detection [42].

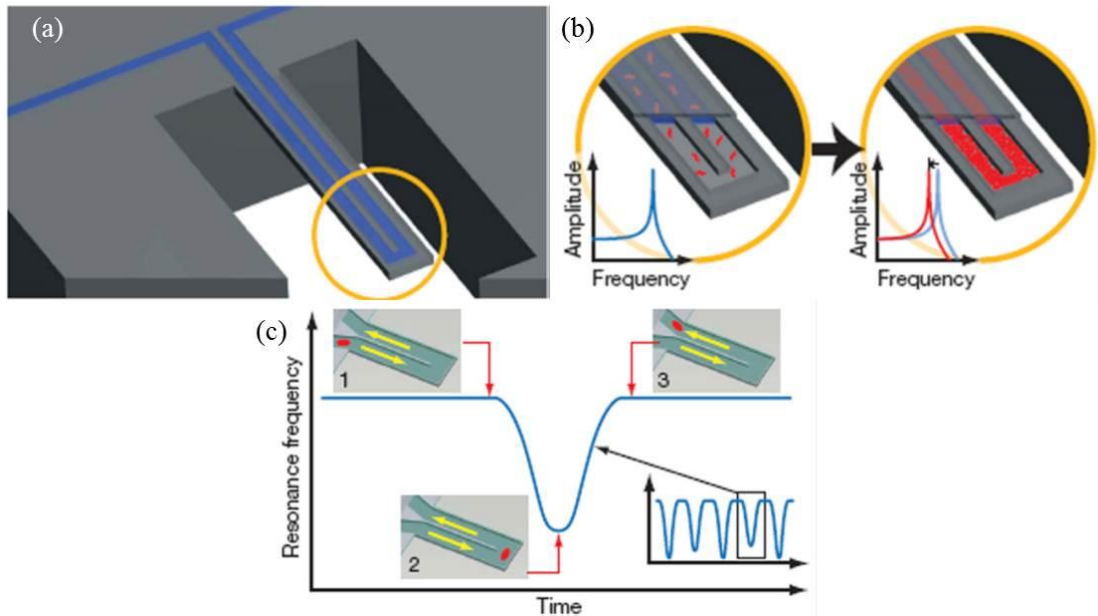


Figure 1.8: Schematic drawing of the principle of operation of a cantilever with microchannel embedded inside. (a) Mass of flowing particles is measured using resonance peak shifts over time under continuous flow of biomolecules, cells or synthetic particles. (b) While bound and unbound molecules both increase the mass of the channel, that bind to the channel wall accumulate inside the device. (c) Another measurement of particles flow through the microchannel of the cantilever without binding to the surface, and the detected signal changes with the position along the channel [41].

The final group of studies is well known application of droplet investigation technique led by R. Bashir's group [43-45]. In one of the first studies [43] the rare cell mass detection by trapping and immobilizing the cell on cantilever based resonator systems, and then, the observation is done under optical equipment. They inject HeLa cells inside of a microfluidic channel and capture the cells on the cantilevers using positive dielectrophoresis. Then, the immobilized cells are dried or cultured at the site of the cantilever array in order to make the measurements. Afterwards, standing on the same concept, cantilever is replaced with a MEMS based mass sensor and the cell growth is monitored for more than 50 hours [44]. Analysis shows that resonating platform designs demonstrate spatial non-uniformity of mass sensitivity or error due to cell position to be less than 4% from the center to the edge of the platform. The structure of the biosensor, measurement setup, and frequency response is presented in Figure 1.9.

One of the newest studies on this method is microdroplet evaporation process with the mass changes during the evaporation of the dimethylsulphoxide and water [45]. By this way, the study validates the possibility of investigation of microscaled physical processes and biological phenomena involving evaporation and mass transport. However, these studies require Lorentz force actuation for resonator sensing components and complex laser systems for observation. Therefore, the system is not practical for usual medical detection.

In a similar study, the water droplet is put on the biotin functionalized resonator device without leakage to the surrounding electrodes on the sides of the resonator as shown in Figure 1.10. It is demonstrated that the capacitive detection of the biotin and streptavidin binding with the mass sensitivity level is $87.76 \mu\text{m}^2/\text{ng}$ in aqueous environment [46]. Besides, the sensor surface immobilization of biotin molecules took place directly on the silicon surface using APTES. The developed sensor can be used to observe the interaction between biotin and streptavidin without the use of labeling or molecular tags. Thus, the method is applicable for a variety of different immunoassay tests.

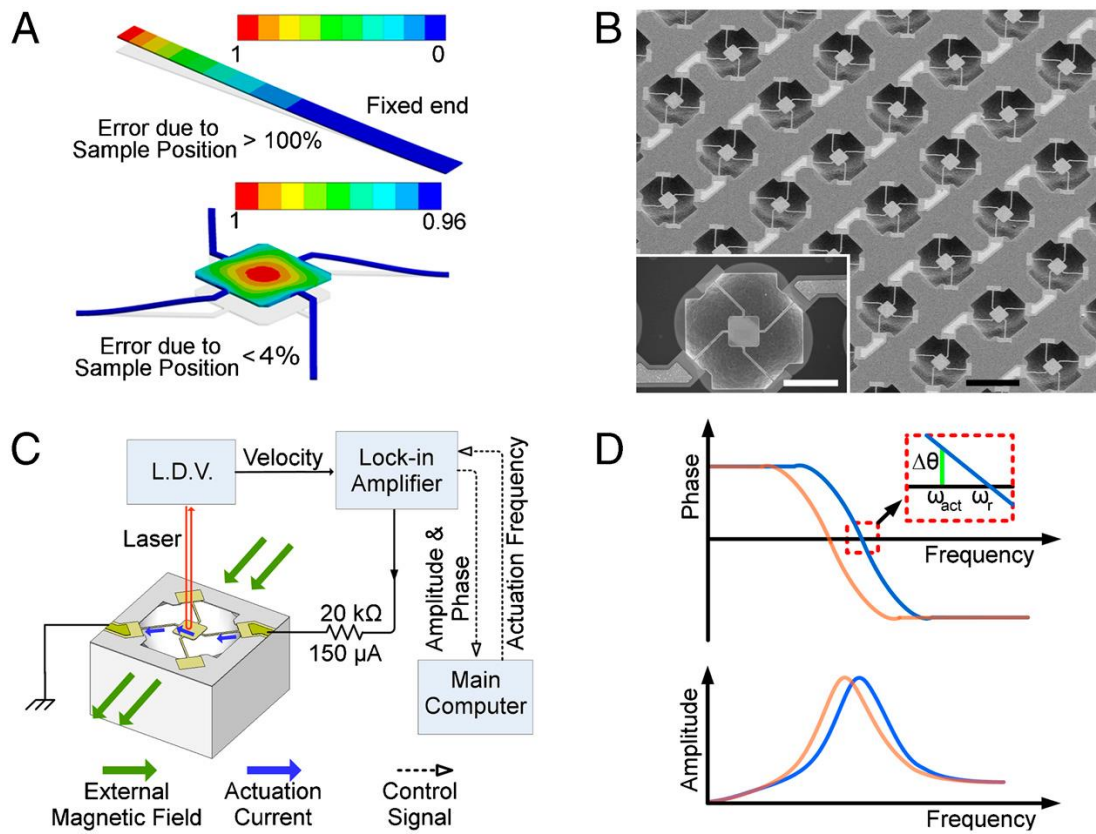


Figure 1.9: (A) Sensor schematic with the first mode of resonance is shown with the mass sensitivity normalized to its maximum value. (B) SEM image showing sensor array and (C) measurement setup are presented. (D) Finally, the frequency response of the sensor with cell attachment (orange), and without (blue) cell attachment are shown [44].

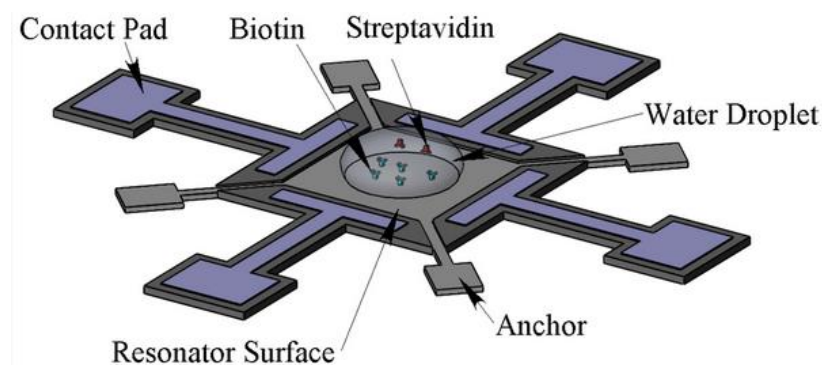


Figure 1.10: Schematic of the resonator and water droplet containing streptavidin spotted on the center of biotin modified resonator far from the surrounding electrodes. [46]

1.4.1 Controlling Damping

The fluidic damping is the main obstacle for the resonator operation under fluidic environment which degrades the performance even to the nullity level. Thus, before closing the chapter, a literature survey for the techniques used for reducing the damping effect is given.

In the study [47] by Joshi *et al.* the general approaches for lowering or even eliminating different types of damping effects for the basic resonator applications are summarized. As mentioned before, the major gravimetric sensing mechanisms utilize cantilever based structures so most of the solutions are enhanced for cantilever applications.

One of the state-of-art methods for prevention of damping under fluidic operation is stated by Linden *et al.* [48], that the adaptation of the fluid interface with a meniscus formation benefits the performance considerably. In the study, a U-shaped design is etched in silicon nitride layer and the meniscus like membrane cantilever is working as a trap for a certain volume of water droplet on the top of the U-shaped cantilever. The schematic representation is shown in Figure 1.11 and the trapping or partial wetting can be observed on top of the silicon nitride cantilever. The sensitivity in DI water flow is measured to be 2.77 fg/Hz, and also the resonance characteristics are shown in Figure 1.11.

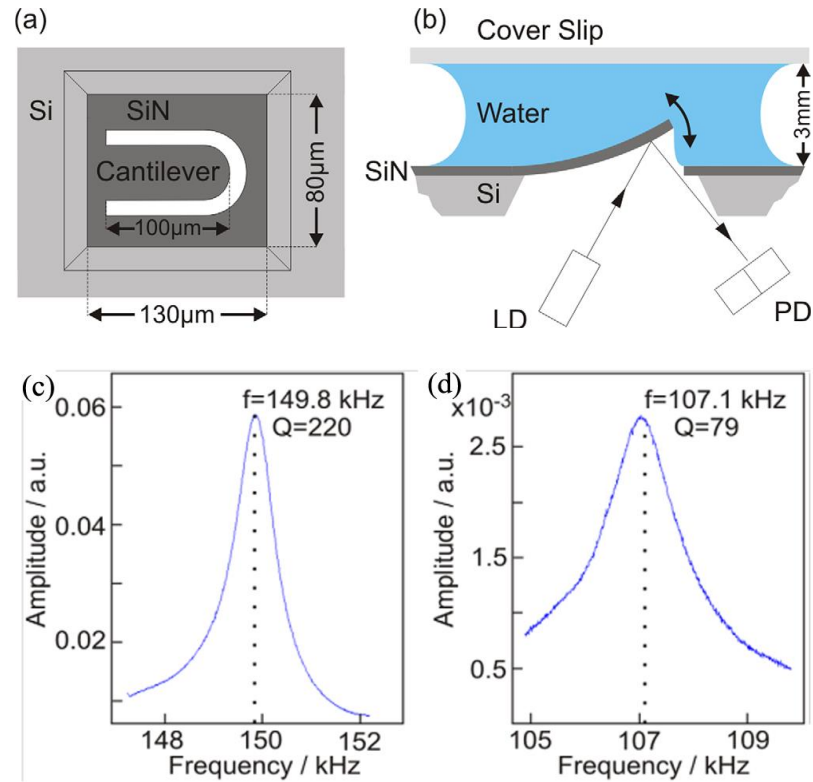


Figure 1.11: (a) Schematic view of the U-shaped groove cantilever etched in a SiN membrane, (b) cross sectional view of the trapping with the meniscus formation on the bottom of the groove is shown. (c) The resonance spectrum measurements are shown in air, and (d) after partial wetting under DI water is applied [48].

In another study, a micro level drumhead like structure with a hole in the middle of the design is presented for the degradation of squeeze film damping under fluidic sensing environment for acoustic radiation [49]. For a narrow band of acoustic frequencies the specific damping issue is solved with the design but it can not be implemented to common practice of resonator geometries in fluidic applications.

Furthermore, Cranch *et al.* show that the low frequency ($\omega \leq 1\text{kHz}$) driven cantilevers are less affected by damping in viscous fluid environments [50]. In another study, the geometry of the cantilevers are manipulated differing from the standard rectangular suspended design [51] and even the placement of the active sites are examined for lowest optimized damping impact [52]. Besides, the advantages of the laterally oscillating cantilevers are shown in fluid mediums with considerable quality factor improvements and with lower limits of mass detection [53].

1.5 Research Objectives and Thesis Outline

In this thesis, the development of a high yield fabrication method for the predesigned gravimetric resonator sensor devices is shown. As the main advantage, the resonators are capable of operating under fluidic flow inside biocompatible microfluidic channels. The newly proposed fabrication flow takes the problems existing for the previous generation cell detection resonator devices into account and by introducing a new approach for the fabrication with the main aim of increasing the fabrication yield considerably. The principal objectives of the thesis are listed below.

- The fabrication process flow will be improved with easily workable process steps and eliminating the wet processes applied on the suspended devices. Moreover, the new fabrication flow considers improving each step one by one, and so the total yield of the fabrication increases.
- The strengthened folded spring anchors and design modifications is aimed to decrease the breakage rate so the endurance of the resonators during problematic fabrication steps is increased from start to end.
- The resonators' operability is intended to be sustained under fluid flow. Therefore, successful hydrophobic parylene coating between fingers and anchors needed to be established. At the same time, the field of the bioactivation gold needs to be cleared for functionalization protocol to immobilize selectively the intended cells after the hydrophobic film coating. Hence, the rare cell detection with the gravimetric resonators is achieved. This issue is aimed to be solved with a novel parylene coating method.
- Finally, the new process flow intends to solve the poor PDMS microchannel architecture. The new fabrication method makes use of an anodic bonded glass microchannel with high opportunity of controlling the alignment with respect to the resonators. The anodic bonding process will seal the microchannel with a negligible leakage. Lastly, the glass microchannel will present better optical transparency compared to the PDMS microchannel architectures.

The thesis focuses on;

In chapter 2, the necessary theoretical background to analyze the operation of micromechanical resonators is given. The characteristics of the MEMS actuators with capacitive actuation and the microfluidics theory are explained. Next, the theories behind the sensing mechanisms of a gravimetric sensor, movement of the mechanical structure, folded spring beams, and damping issue on the structure are given. Finally, the design parameters of the devices are optimized together with COMSOL finite element analysis results.

Chapter 3 summarizes the fabrication process development of the resonators. Previous fabrication process flows and the newly proposed process flows are inspected. The advantages and disadvantages are presented with the solutions of the issues. Implemented solutions to the previous generation fabrication flows are summed up in the new generation fabrication process flow with a newly introduced approach to fabrication. Finally, the problems encountered during the new process flow are submitted with the solutions for the issues.

Chapter 4 starts with the novel method of parylene hydrophobic coating trials. Afterwards, the experimentation and test results are presented. First, the experimental setup and test environment is briefly introduced. Then, the results of various tests such as resonance characterization with and without parylene coating are presented. The results are compared with the previous generation cell detection studies of the METU BioMEMS group.

As the closure, conclusions and future works are presented in Chapter 5.

CHAPTER 2

THEORY & DESIGN

In this thesis, the proposed resonator structure is basically an electrostatic capacitive comb drive resonator with folded spring beams. Thus, the study is narrowed down to these operation principles of the comb drive resonator structures from now on. Capacitive comb drives are used in many different applications in the literature including charge sensors [54], microgrippers [55], gyroscopes [56] and accelerometers [57].

In this chapter, an introduction for gravimetric detection is summarized. Then, the theoretical background and the operation principles of the BioMEMS group resonators are stated. Finally, the device characteristics and major trade-offs of the design parameters are described, and through this examination the optimized limits of parameters for the device are stated.

2.1 Gravimetric Detection

The gravimetric detection concept relies on the change of the natural frequency, of the resonator, when the resonator mass changes. There is an inverse quadratic relation between the resonance frequency of the system and the oscillating mass of the resonator. Actually, the spring constant and the damping coefficient of the resonator system changes but the transition remain at a negligible level for most gravimetric sensing systems.

The resonator sensor beam can be examined as a mass, damper and spring system as represented in Figure 2.1, in this representation the biological load is also added as an added smaller spring, damper and spring system installed in parallel with the main mass, spring and spring system. Where k_{res} and k_{bio} represents the spring constants, η_{res} and η_{bio} denotes the damping constants and m_{res} and m_{bio} represents the resonating mass for resonator sensor and the biological analyte respectively. The springs accumulate force and the dampers dissipate the force in the system [5].

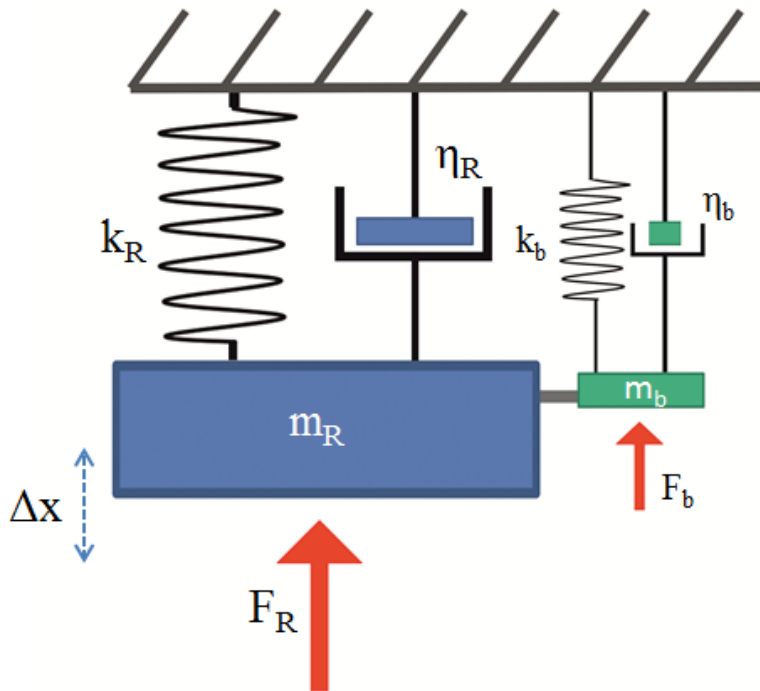


Figure 2.1: Schematic view of second order mass and loaded biological entity with two parallel spring and damper systems.

The following equation describes the second order behavior of this system;

$$m\ddot{x} + \eta\dot{x} + kx = F \quad (2.1),$$

where x identifies the proof mass displacement, F represents the applied force, m stands for the system mass, η is the damping constant, and k is the spring constant. The gravimetric resonator system is a linear and time-invariant system, so we can

take the Laplace transform of the above equation to obtain the transfer function of the system as applied in Equation (2.2) [58].

$$H(s) = \frac{1}{ms^2 + \eta s + k} \quad (2.2)$$

Then, we can identify the natural frequency ω_n of the system as in Equation (2.3);

$$\omega_n = \sqrt{\frac{k}{m}} \quad (2.3)$$

The shift of the resonance frequency of the resonator (ω_d) from the natural frequency (ω_n) is caused by the damping applied on the system [59] as in Equation (2.4).

$$\omega_d = \omega_n \sqrt{1 - \xi_d^2} \quad (2.4)$$

where ξ_d is the damping ratio, and defined as in Equation (2.5).

$$\xi_d = \frac{\eta}{2\sqrt{mk}} \quad (2.5)$$

If the damping ratio is higher than 1 ($\xi_d > 1$), from the Equation (2.4), the frequency of oscillation will become complex [60]. In this case, the system is called to be over-damped and the resonance peak will be degraded. If it is smaller than one ($\xi_d < 1$), the system is called under-damped and the resonance oscillation frequency becomes closer to the natural resonance frequency where the damping ratio gets even smaller. If the damping ratio is equal to 1 ($\xi_d = 1$), then critical damping state occurs, and the natural frequency asymptotically approach to zero.

Furthermore, in mass sensing applications, the parameter that indicates the resonator performance is the quality factor; Q . For resonance applications, quality factor is the parameter that indicates how much the system is under-damped. In other words, the quality factor expresses the dissipation of energy due to damping from the total stored energy of the resonating system. Therefore, resonance oscillations vanish in a slower manner caused of damping when the quality factor increases. The general

definition of the quality factor is defined as in Equation (2.6) by the means of energy E and so Equation (2.7) is derived.

$$Q = 2\pi \frac{E}{\Delta E} \quad (2.6)$$

$$Q = \frac{1}{2\xi_d \sqrt{1 - \xi_d^2}} \quad (2.7)$$

For this study, the damping ratio is much smaller than 1 ($\xi_d \ll 1$). Thus, Equation (2.7) can be simplified into Equation (2.8).

$$Q \cong \frac{1}{2\xi_d} = \frac{\sqrt{km}}{\eta} \quad (2.8)$$

When Equation (2.8) is analyzed, Q is a parameter that can be calculated from the resonance frequency spectrum measurement result in a very narrow frequency range. Firstly, the resonant frequency ω_n is measured and then, the amplitude A_r at the resonance frequency is expressed. Then, the amplitude and frequency parameters around the resonant frequency with -3 dB low amplitude margins ω_1 and ω_2 are measured. Finally, the quality factor (Q) can be calculated by the reinterpretation of Equation (1.3);

$$Q = \sqrt{3} \frac{\omega_0}{\omega_1 - \omega_2} \quad (2.9).$$

2.1.1 Damping Mechanisms

The quality factor of the gravimetric resonators is decreased mostly by the energy dissipation of the damping effects of the resonator relation with the environment. Broadly speaking, the damping mechanisms fall into two main categories; fluid and structural damping. The fluid damping is divided into viscous and acoustic radiation based damping and the structural damping is separated into thermo elastic damping (TED) and anchor loss [61]. Thus, the lowest quality factor dominates the general

quality factor of the resonator resonance characteristics. The quality factor relations are given in Equations (2.10) to (2.12).

$$\frac{1}{Q} = \frac{1}{Q_{fluid}} + \frac{1}{Q_{structural}} \quad (2.10)$$

$$\frac{1}{Q_{fluid}} = \frac{1}{Q_{viscous}} + \frac{1}{Q_{radiation}} \quad (2.11)$$

$$\frac{1}{Q_{structural}} = \frac{1}{Q_{TED}} + \frac{1}{Q_{anchor}} \quad (2.12)$$

A thin fluid layer like air is trapped in the gap between the MEMS moving structure and the substrate. Then, the complex interaction between fluid and vibrating suspended structure results in both damping and stiffening of the structure. When the gap thickness is sufficiently small compared to the lateral dimensions of the geometry, the squeeze film damping (SFD) dominates. SFD is affected by various factors like geometry of the structure, oscillation frequency, packaging pressure, thickness of the fluid film, and boundary conditions [61]. SFD dominates, often by one or two orders of magnitude over the other damping mechanisms. The optimization is done for SFD affect is done with a linearized form of the modified Reynolds equation as mentioned by Pandey *et al.* in [62] represented in Equation (2.13);

$$\nabla_T (h_0^3 f_{ch} \nabla_T P_f - 6\mu h_0 \vartheta_T) = j\omega l 2\mu (P_f \frac{h_0}{P_a} + \Delta h) \quad (2.13)$$

where P_f is the film pressure in the gap, f_{ch} is the relative flow function, that stands for inertial and rarefaction effects, Δh is the gap deformation ($h - h_0$), and ϑ_T is the tangential velocity of the structure moving above a fixed substrate. The tangential operator ∇_T refers to the fact that equation is solved on boundary conditions.

2.1.2 Resonator Damping Model

The lateral motions of the proposed comb drive resonator overwhelming damping components on the resonator are the slide film and squeeze film types. The optimization for the parameters to prevent damping effect is difficult to model based on approximations and limitations. For a start, MEMS design needs to be simulated with a full flow simulation around the entire vibrating structure, at least to check various assumptions underlying the SFD models. The first difficulty is that all Navier-Stokes numerical solvers that we are aware of do not propose a harmonic solver. The second difficulty is the high computational cost of 3D flow simulations around complex MEMS structures [61].

At this point, we need to express the microfluidic based motion characteristics. The microfluidics is based on motion of fluid inside a micrometer level channel and the characteristics of these kinds of fluids become restricted to Newton's motion equations [63]. The general remarks for the microfluidic flow is that all fluid flow is laminar rather than turbulent, surface tension becomes an important force, inertia becomes less effective, and the apparent viscosity increases considerably.

The equation of motion for an incompressible fluid is expressed in Equation (2.14); with the fluid density ρ is constant.

$$\frac{\partial \rho}{\partial t} = 0 \quad (2.14)$$

If the velocity of the fluid is ϑ , the divergence of unit mass in a unit area is equal to the decrease in density per unit time as shown in Equation (2.15). Thus, we evaluate the Equation (2.16).

$$\nabla(\rho\vartheta) = -\frac{\partial \rho}{\partial t} = 0 \quad (2.15)$$

$$\nabla\vartheta = 0 \quad (2.16)$$

Then, with Newton's law for forces acting on a unit volume of fluid, the force per unit volume is written as Equation (2.17).

$$F = -\nabla\rho - \rho\nabla\phi + F_{vis} \quad (2.17)$$

where $-\nabla\rho$ is the pressure force per unit volume and $-\rho\nabla\phi$ is the force per unit volume associated with the potential ϕ and F_{vis} is the viscous force.

The viscosity is defined for a Newtonian fluid is as in Equation (2.18) with surface velocity is ϑ and separation of the channel is d ;

$$F_{vis} = \mu A \frac{\vartheta}{d} \quad (2.18)$$

Thus, the more viscous the fluid is, the force required to drive is increased. By these means, there are two types of fluid flows in microfluidic devices; Couette and Poiseuille flows. The Couette flow is a steady viscous flow between parallel walls, the velocity of the fluid varies linearly from zero at the stationary bottom boundary up to velocity ϑ at the moving plate (See Figure 2.2a). The Poiseuille flow is a pressure driven flow between stationary parallel plates of microfluidic channel. A parabolic variation occurs for the pressure with the maximum velocity in the middle of the microchannel and zero flow velocity at the walls (See Figure 2.2b).

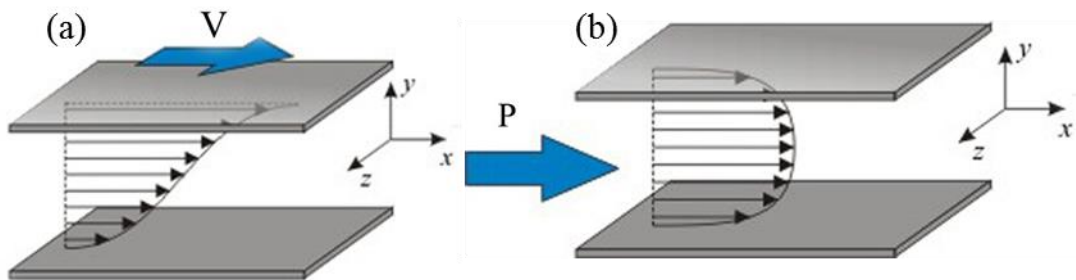


Figure 2.2: The representations of microfluidic flows; (a) Couette flow, and (b) Poiseuille flow [63].

The relation between viscosity and inertia is denoted by Reynolds number (Re), for the fluid flow. The Reynolds number is referred in Equation (2.20) with F_{iner} and F_{vis} stand for inertial and viscous forces acting on fluids. In the case of high Reynolds numbers ($Re > 2000$) the inertial force dominates the viscous forces and the flow becomes turbulent. For low Reynolds numbers ($Re < 1$) the viscous forces dominate and the flow becomes laminar. In laminar flow conditions the mixing of fluids occurs only by diffusion, which is slow compared to turbulent mixing.

$$F_{vis} = \mu A \frac{\vartheta}{d} \quad (2.18)$$

$$F_{iner} = ma = \rho A \vartheta^2 \quad (2.19)$$

$$Re = \frac{F_{iner}}{F_{vis}} = \frac{\rho d \vartheta}{\mu} \quad (2.20)$$

According to the previous definitions, for an indefinitely wide channel the Navier-Stokes equation for fluid flow is interpreted as in Equation (2.21).

$$\frac{\partial v}{\partial t} + v \frac{\partial v}{\partial x} = \frac{\mu}{\rho} \frac{\partial^2 v}{\partial z^2} \quad (2.21)$$

where ρ is the density of the fluid medium and μ is the dynamic viscosity of the fluid, and v is the velocity of the plate in the x-direction. Assuming that the amplitude of the vibration is small, the second term in the equation can be neglected [61].

Then, the simplified Couette damping model is used when the oscillation frequency is relatively low and the effective decaying distance becomes relatively larger than the gap between the resonator and the opposing surface in terms of distance [60]. This approach is valid for the sidewalls and the bottom plate of the resonator. Then the expression for the damping force on that surface becomes as in Equation (2.22).

$$F_{damping} = \mu \frac{A_p}{d_p} \frac{dx}{dt} = \eta_{Couette} \frac{dx}{dt} \quad (2.22)$$

where A_p is the effective surface area, d_p is the distance between the opposing surfaces and $\eta_{Couette}$ is the damping coefficient for the surfaces for Couette flow model as mentioned above.

Assuming the gap thickness is larger than some extend ($g > 10 \mu\text{m}$) then Couette model is not applicable and the more generalized Stokes model should be used instead [61]. This is the case for the top surface of the resonator where the channel thickness is relatively high. When the Stokes model is used, the damping expression changes to Equation (2.23).

$$F_{damping} = \mu \frac{A_p}{\delta} \frac{dx}{dt} = \eta_{Stokes} \frac{dx}{dt} \quad (2.23)$$

where δ is the effective decaying distance and it is denoted as in Equation (2.24).

$$\delta = \sqrt{\frac{2\mu}{\rho\omega}} \quad (2.24)$$

The final component of the damping force which influences the resonator system is the drag force. The drag force that affects the interfacing rectangular plates can be expressed as in Equation (2.25).

$$F_{drag} = \frac{32}{3} \mu l \frac{dx}{dt} = \eta_{drag} \frac{dx}{dt} \quad (2.25)$$

where l is the characteristic dimension of the plate which can be assumed as half the width of the plate. The drag force increases when a biological analyte as assumed to be a spherical cell is attached to the resonator proof mass. Then, the expression of the drag force for the cell component becomes as in Equation (2.26).

$$F_{drag} = 6\pi\mu R \frac{dx}{dt} = \eta_{drag} \frac{dx}{dt} \quad (2.26)$$

where R is the radius of the attached particle or cell.

The total damping force acting on the resonator proof mass can be calculated by simply adding all these damping force components in Equations (2.22) to (2.26). If we take into account that the resonator geometry parameters are relatively affect all the damping effects with the operation dimensions of the microchannel.

2.2 Resonator Detection Capabilities

The basic detection principle of the proposed resonator device is expressed as a comb drive resonator. The capacitive actuation of comb drive resonator capacitance varies through a change in the overlap area between a set of interpenetrating comb fingers. The two overlapping comb fingers are shown in Figure 2.3 with the defined parameters in the schematic.

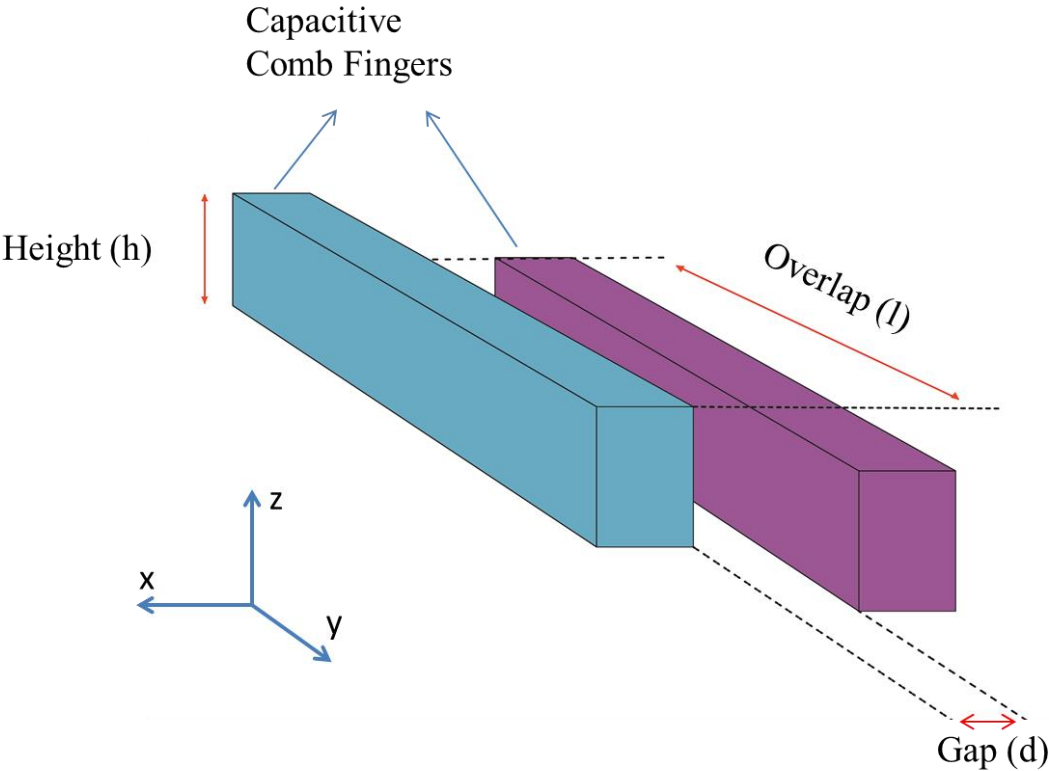


Figure 2.3: Schematic view of the overlapping parallel comb finger capacitors is shown.

In the previous sub chapter the damping affect and the energy dissipation under air damping and fluid damping are presented. If we take into consideration about these issues, we can now parameterize the detection capabilities of the resonator device for sensing in fluid. The mass added of the resonator is related with the natural frequency of the resonator in aspect of Equation (2.3) mentioned here again.

$$\omega_n = \sqrt{\frac{k}{m}} \quad (2.3)$$

From the Equation (2.3) we understand that there is an inverse quadratic relation between the mass of a resonant system and its natural resonance frequency. The loaded mass (Δm) can be extracted from this expression as in Equation (2.27).

$$\Delta m = k \left(\frac{1}{\omega_1^2} - \frac{1}{\omega_0^2} \right) \quad (2.27)$$

If the loaded mass of the biological entity is at least one order of magnitude smaller than the resonator which is valid for the design under consideration in this study; the derivative of the resonance frequency simplifies to Equation (2.28).

$$\left| \frac{\partial f_n}{\partial m} \right| \cong \frac{f_n}{2m} \quad (2.28)$$

Thus, to generate the minimum detectable load mass on a resonator, we need to determine the minimum detectable frequency shift. Moreover, the minimum detectable frequency shift expands if the noise contribution of the frequency spectrum increases. There are mainly two noise sources that generate these uncertainties for the resonator device; firstly, the thermal noise resulting from random phonon motion of the structures, and secondly the electronic noise resulting from interface circuit and experimental setup.

By using equipartition theorem and thermal energy and spectral noise calculations the mean square frequency modulations due to thermal noise is calculated and given in equation (2.29) [64].

$$\langle (\Delta\omega)^2 \rangle = \frac{1}{2\pi} \int_{\Delta\omega}^{\infty} \frac{2E_\phi}{E_{osc}} (\Delta\omega)^2 d(\Delta\omega) \quad (2.29)$$

where $\Delta\omega$ is the frequency instability amount, E_{osc} is the oscillation energy, and E_ϕ is the phase noise energy.

After the integration and rearrangement of the Equation (2.29), the minimum detectable force gradient and the minimum detectable frequency shift are found to be as expressed with Equation (2.30) and Equation (2.31) respectively.

$$(\Delta F)_{min} = \frac{2k\Delta\omega}{\omega_0} = \sqrt{\frac{4kk_B T}{\omega_0 Q} BW} \quad (2.30)$$

$$(\Delta\omega)_{min} = \frac{2}{x_{osc}} \sqrt{\frac{k_B T}{kQ} \omega_0 BW} \quad (2.31)$$

where x_{osc} is the maximum amplitude of oscillation, k_B is the Boltzmann constant, T is the ambient temperature, and BW is the measurement bandwidth. Thus, the minimum detectable mass load of a resonator can be extracted by simply dividing Equation (2.31) and Equation (2.28), then we reach to expression given in Equation (2.32) which gives the theoretical limit for the minimum detectable mass of a resonant system.

$$(\Delta m)_{min} = \frac{4}{x_{osc}} \sqrt{\frac{m\eta k_B T}{k} BW} \quad (2.32)$$

Yet it only takes mechanical noise into account, and it is not applicable to practical cases accurately. Even so, the equation gives clues for the factors contributing the performance of the sensor, and we can decide on the revision of the parameters.

If we take the previous theoretical results into account, decreasing the mass and damping effect for a resonator means the improvement of the overall performance. Also, the mass can be decreased by geometry minimization so this will directly decrease the mass of the resonator and decrease the damping on the mass. Furthermore, if the geometry is reduced, trimmed anchors results in the spring

constant increase or the increase of the stiffness and these manipulations improve the minimum detectable mass limit.

On the other hand, there is a trade-off in this aspect that the spring constant increase causes decrease in the oscillation amplitude, and degrades the minimum mass resolution of the sensor. The reduction of the signal amplitude, result in reduction of the sense port current signal. Moreover, this causes a major decay on the signal to noise ratio characteristic of the whole sensor system. Unfortunately, the minimization of the geometry with high stiffness produce less number of comb drive fingers and the requirement of higher electrostatic force, which means increasing the operation driving voltages for actuation. Last but not least, the possibility of the attachment of biological analyte to the proof mass geometry is the basic sensing mechanism of the resonator systems and the minimization of the proof mass area geometry directly degrades the binding probability of these analytes.

2.3 Resonator Design

The proposed gravimetric comb drive sensor design of METU BioMEMS group is represented in Figure 2.4. The sensor consists of symmetric drive and sense stationary electrodes on the top and bottom of the resonator design represented in green and purple colors respectively. The proof mass of the resonator structure is anchored to the bulk substrate by four identical folded spring beams. Also, a bioactivation functional gold coating on the proof mass surface which is represented with yellow field is placed. The resonators are placed inside a glass microchannel structure shown in Figure 2.4b with a three dimensional representation with bioactivation antibodies are included.

The actuation of the resonator is derived with the applied AC signal to the drive electrode and the sensing is measured with the sense electrode, and the proof mass is biased from the substrate through the folded spring beams with DC potential. The microchannel is aligned on the resonator for introduction of the biological analytes like cells through a microfluidic system.

The resonator dimensions and parameters are determined after close consideration of the theoretical investigation presented in the previous sections. Many of these parameters are affecting multiple characteristics of the resonator in other words, there are many trade-off situations rising on the dimensions of the resonators. Besides, there are some concerns that need to be dealt with certain solutions are mentioned below.

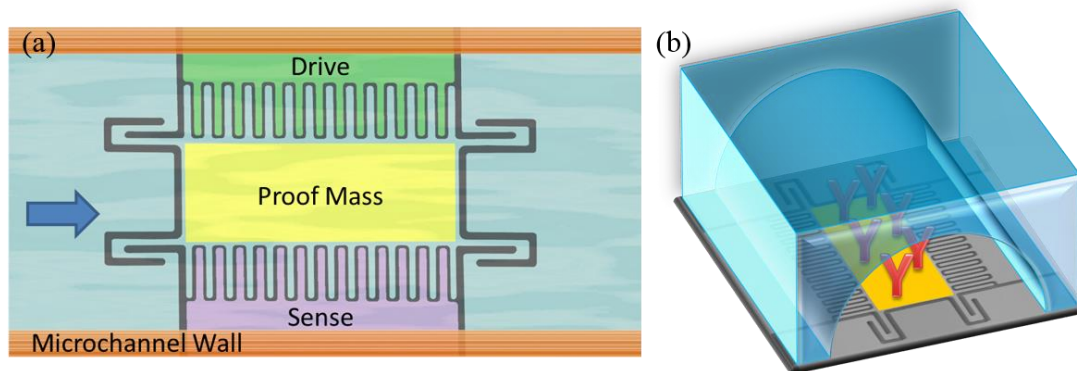


Figure 2.4: Schematic view of (a) resonant mass sensor embedded into the microchannel, and (b) 3-D representation of microfluidic channel and the bioactivation functionalized on the proof mass gold active area.

The first approach for preventing the squeeze film damping effect of fluid flow is aligning the resonators in laterally with the fluid flow gradient. The squeeze film damping occurs on the vertical dimension and with lateral placement of the resonator, the effect is eliminated. Therefore, the architecture of the resonator with spring beam and proof mass geometries has to be restricted that the fundamental oscillation motion of resonator is in lateral direction and other vibrational oscillation modes can not ascend over the fundamental mode of oscillation.

The proof mass bioactivation site require to be lying inside the microchannel flow pattern which limits the maximum dimensions for the proof mass geometries and also from the microchannel point of view, the microchannel minimum width is required to be equal or wider than the proof mass dimensions.

The depth of the microchannel is limited with the flow characteristics of the fluid flowing on the resonator. The height of the channel is required to be larger than the

size of the biological analyte as in this study, cells without any clinging. On the other hand, if the microchannel is too broad, the immobilization of the cells on the resonator proof mass becomes a problem.

There should be an adequate active area space on the resonator proof mass for bio functionalization in order to immobilize the cells or other biological analytes of interest. Additionally, the amplitude of the resonance sensing signal is higher for larger resonator geometries and the natural frequency magnitude make ease for the measurement constraints. On the other hand, the resonator quality factor highly benefit from the minimization of the resonator geometry. Also, the minimum detectable mass and the relative mass sensitivity become flourished with small resonator geometries.

The height of the resonator is defined by the active layer of the SOI wafer in this design which is chosen to be 5 μm for this study. The thickness of this active layer needs to as thin as possible for decreasing the initial mass of the sensor for high relative mass sensitivity. Still, the fabrication process performance limits the SOI thickness purchased. The thickness of the resonators directly supports the endurance of the resonators during fabrication and operation periods.

The critical dimensions of the resonators are shown in Figure 2.5. w_m and l_m denote the width and length parameters of the resonator proof mass; and w_s and l_s are the width and length of the spring beams. a_s represents the aperture of the spring with including gap and width of the folded spring beams. w_f and g_f are the width of the capacitive comb fingers and the gap in between fingers of the comb geometry. The thickness and the gap length are kept constant for fabrication demands. These dimensions directly impact the capacitive gain of the system but the limitations of the variables are mostly considered for implementing a properly working lateral resonator structure.

The major concern of the geometry of the whole masking layer for the resonator geometries lies on the application of hydrophobic coating for increased sensitivity under fluid flow. The success of the hydrophobic coating is limited to 4 μm gap space (with 5 μm device thickness) in between suspended structures for whole geometry exposed to the fluid flow in microfluidic channel.

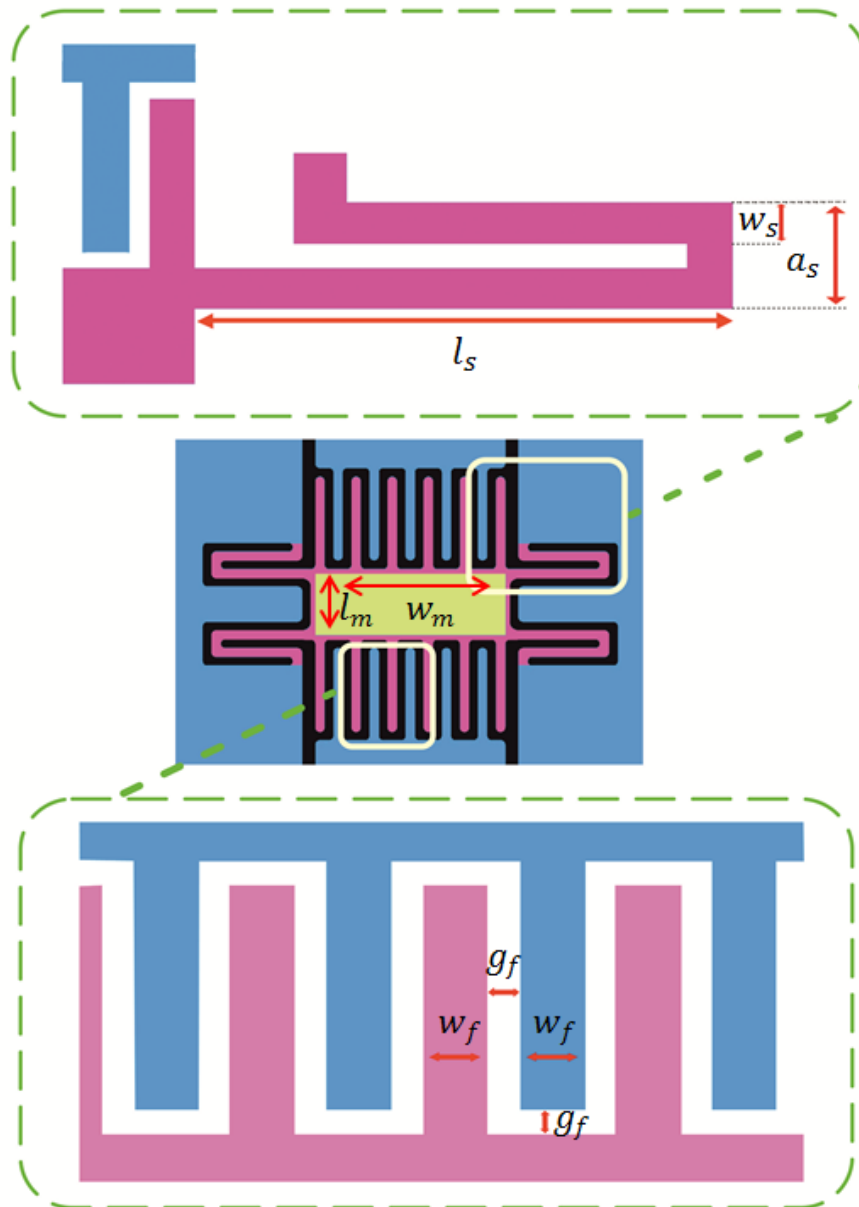


Figure 2.5: Schematic view of double folded beam and finger geometries of the resonator with design parameters are denoted.

2.3.1 Folded Spring Beams

The spring beams are kind of anchors that are coupled to bulky proof mass and fix the proof mass to the mechanical ground or the substrate for MEMS suspended devices. Different types of spring beam architectures are investigated for MEMS

resonator designs in [65], as clamped beam, crab leg beam, folded beam and U-shaped, fish hook, and serpentine beam models.

Based on our study purposes the double folded beam structure is chosen for its high linearity, free of buckling problems, and the high stiffness value in the out-of-plane direction. As derived in [66] the stiffness constant of the double folded spring anchors in x, y, and z directions are given in Equations (2.33), (2.34), and (2.35) respectively.

$$k_x = 2E \frac{hw_s^3}{l_s^3} \quad (2.33)$$

$$k_y = 2E \frac{hw_s}{l_s} \quad (2.34)$$

$$k_z = 2E \frac{h^3w_s}{l_s^3} \quad (2.35)$$

The resonator anchor architecture supporting the proof mass is an important factor but the other concern is the placement of the anchors along the proof mass sidewalls. The primitive design is to connect the proof mass with two spring anchors to the midpoints of the proof mass edges. However, this approach causes some issues. Firstly, the structure becomes prone to oscillate under rotational modes as the fundamental mode of vibration. Secondly, the uniformity of movement along the resonator field is coerced, which is crucial for the high performance of the device. To eliminate these issues, we choose four support beams or anchors with folded beam structure on the vertices of the proof mass. When the resonator proof mass is supported with four spring beams on its vertices, rotational vibration modes are repressed to high frequencies far away. In other words, the unwanted rotational vibrations are removed from the active working frequency range. Also, the movement uniformity is sustained in acceptable range along the whole resonator device components.

2.3.2 Hydrophobic Parylene Coating

As mentioned before the Parylene is the leading type of the polymer family for its conformable high coating uniformity, high compatibility with MEMS fabrication techniques, relatively high working temperature, biocompatibility, and transparency properties. The parylene surfaces are inert to many strong chemical treatments and resistant to fungal and bacterial growth makes the polymer ideal for BioMEMS applications [67].

The hydrophobic characteristic of the parylene thin film coating is a well-known property of the Parylene-C polymer [68]. In this study, this hydrophobicity is used for in fluid applications of BioMEMS with suspended MEMS structures for prevention of penetration of liquid like resonators [69]. Parylene-C is conformably coated on the suspended components, and thus, the surface thermodynamic equilibrium takes place and the interfacial energy on the surface of thin film Parylene-C prevents the liquid penetrating in between the suspended fingers of the resonator (See Figure 2.6). The parylene-C layer is also a good insulating material with conformal coverage which protects the cross talk between the liquid and the silicon and gold layers. Consequently, the enhancement of the quality factor is reported and the in fluid operation of the proposed design is validated [70]. The quality factor improvement under fluid flow is shown in Figure 2.6. By this method, the resonators possibly become functional under fluid flow. Thus, the feasibility of suspended biosensors that can be directly implanted into microfluidic channels arises, the resonance characteristics and the calculated quality factor results are shown in Figure 2.7.

An opposing effect of the parylene layer coating is the increase in capacitances of the comb drive actuators, since the effective permittivity of the capacitive gap is increased with the insulating coating. The resultant permittivity level can be calculated with the Equation (2.36).

$$\varepsilon_{total} = \left[\frac{(d - 2t_p)}{\varepsilon_0} + \frac{2t_p}{\varepsilon_p} \right]^{-1} \quad (2.36)$$

where ϵ_{total} is the effective permittivity of the capacitive gap, t_p is the thickness of the parylene layer, and ϵ_p is the relative permittivity of parylene.

As a result, the minimum thickness that Parylene-C can be coated conformably with proper hydrophobic properties needs to be achieved. This value is experimentally checked and the minimum thickness achieved with the CVD based Parylene-C coating tool, we observe 0.4 μm thickness is the best fit for the expectations.

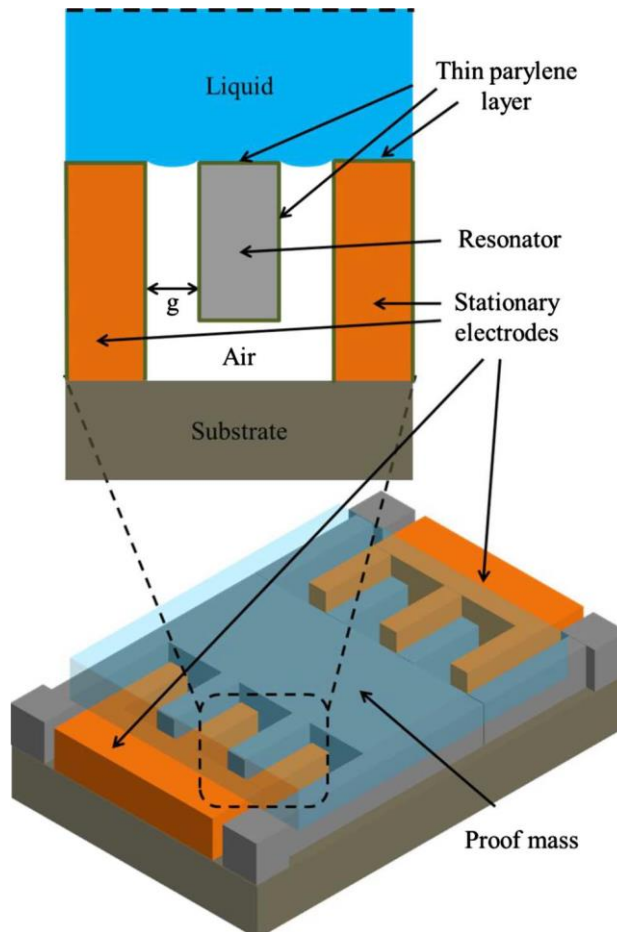


Figure 2.6: The schematic cross sectional view of the resonator comb finger is shown with Parylene-C is conformably coated on the suspended components. Thus, the surface thermodynamic interfacial energy keeps the liquid without any penetration [69].

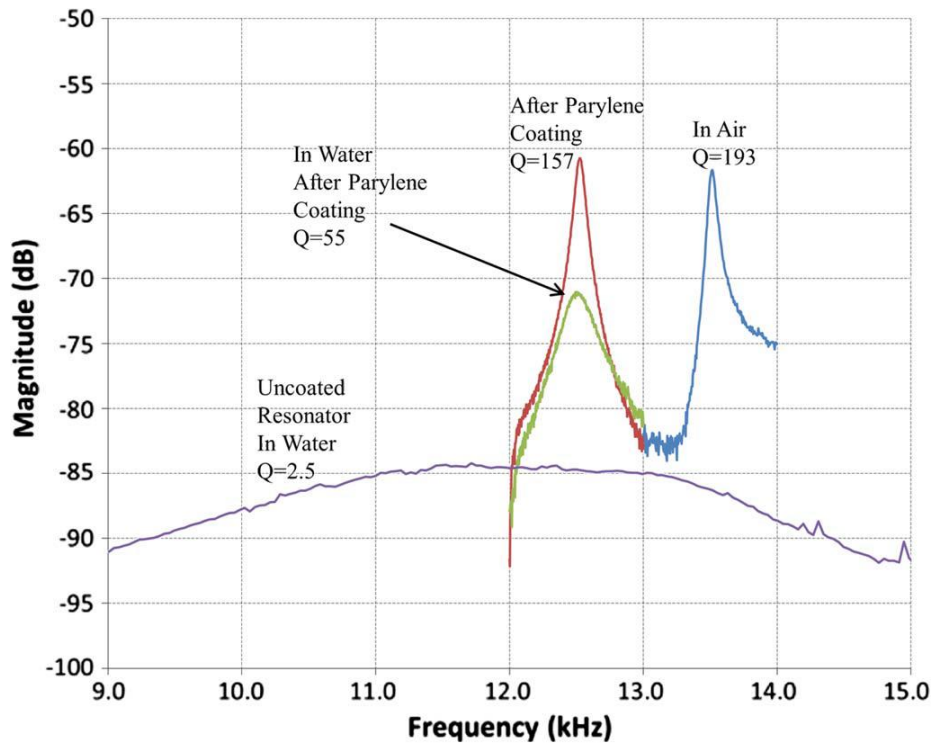


Figure 2.7: The quality factor improvement with parylene coating on the resonator fingers is shown as a comparison with resonance characteristics of bioresonator in air, after parylene coating and uncoated performance in water [69].

2.4 FEM Simulations

Finite element modeling (FEM) simulations are conducted with COMSOL Multiphysics software, in order to verify the natural resonance frequencies of the designed resonators. As mentioned in the previous sections, the fundamental oscillating motion of the resonator that we are interested in is the lateral resonance movement. The simulation results are investigated that the other modes like out of plane oscillation or rotational motion should be far away from the fundamental resonance frequency mode.

The fundamental lateral oscillation is shown in Figure 2.8 for RES #1 design, the simulations are repeated for all 14 designs of the resonators and it is shown that the fundamental vibration characteristics is the lateral oscillation for all of them as expected.

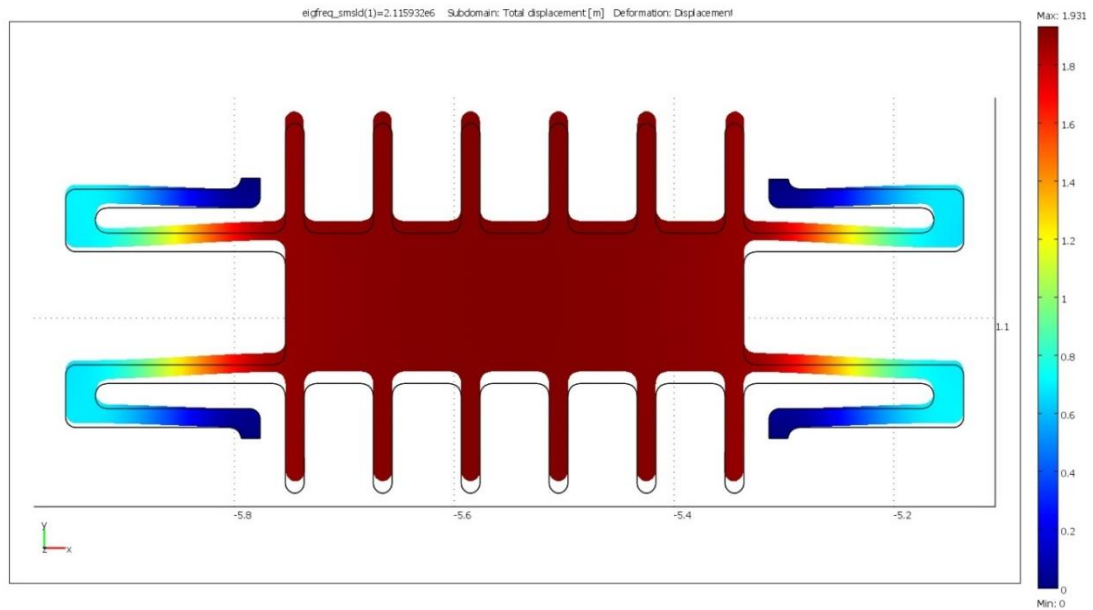


Figure 2.8: Fundamental vibration mode of design RES#1 at 1.47 MHz.

The finger displacement inside the resonator comb gaps is also calculated to be very low considered with $1 \mu\text{m}$ mid-level for the pull-in effect. This shows that the designs will be operational with proper fabrication without any distortions.

Another important issue on the resonator devices is the buckling effect with the new designs that the proof mass and anchor parameters are changed and the possibility of buckling have to be controlled. In Figure 2.9, the maximum buckling displacement of the resonators with the gravitational forces is simulated; and the maximum displacement is on the middle of the resonator proof mass and the value is around 0.1 picometers. Thus, it is also concluded that the effect of buckling under normal operation of the resonators are suitable for aimed applications. However, the buckling effect of the resonators and other components of the layout are also required to be tested under fluid operation in practical applications. The tests are done and shown in the test results chapter.

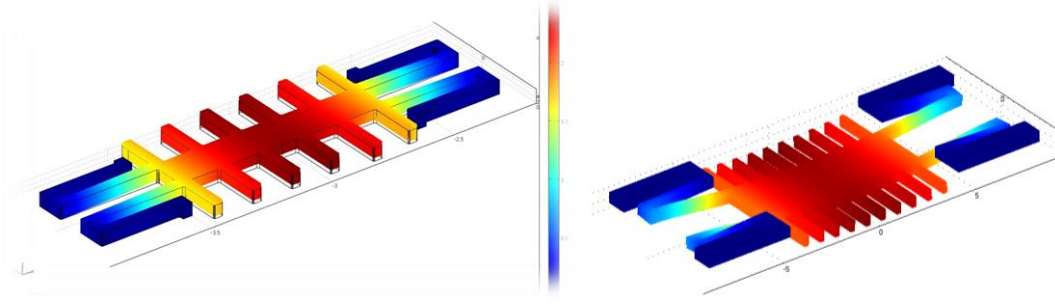


Figure 2.9: The buckling of the resonators are simulated for gravitational forces. The maximum buckling displacement at the middle of the proof mass is measured to be 0.1 pm.

2.5 Design Determinations

In order to improve the design, we need to optimize the parameters of the layout geometry. For deciding which parameter to maximize or minimize, and also to observe the effect of the manipulations with certain parameters, we define figure of merit (FOM). For maximizing the theoretical minimum detectable mass of the resonator, the following figure of merit can be defined as in Equation (2.37).

$$FOM = \frac{[\epsilon_m \epsilon_0 h]^3 \sqrt{l_s^3 l_p V_{dc}^4}}{\eta^3 w_p^{3.5} g^{10.5} t_p^3} \quad (2.37)$$

Unfortunately, the FOM expression takes only the mechanical noise of the resonator into account, so the directions and critical parameters can be extruded from the expression but the theoretical predictions has its limitations on the real applications. Yet, the interface electronics and the external measurement setup should also be taken into account during the revision of the design.

Bethinking these considerations and issues of the fabrication endurance leads us to a requirement of a new design with certain manipulations. Firstly, the breakage problems with the previous fabrication flows and with respect to the limitations of the lithography tools, the resonator anchors are chosen not to be thinner than 2 μm . The minimum feature size will be 2 μm for the new resonator designs.

Secondly, the thick anchors increase the stiffness, and endurance, so the mass resolution increases as the resonance frequency is increased. However, as the resonance frequency increases, the readout circuit limitations become inevitable. The limit of measurement is theoretically around 3 MHz with the chosen transimpedance amplifier that we use for amplifying the signal out. However, getting close to this limit of frequency the reading of the circuit fluctuates and signal to noise ratio becomes worsen. The natural frequencies of the resonators are required to be restricted under consideration of this measurable spectrum.

Thirdly, to guarantee that the devices will oscillate in lateral direction, the coefficient of stiffness for the double folded spring beams in the z-direction should be high enough. For this purpose, the beam dimensions are determined to maintain this relation; $l_s > h \gg w_s$. Resonator proof mass width, w_m has to be chosen with respect to the microchannel dimensions. Also, these dimension, w_m and l_m required to be related for preventing arising of unwanted resonance oscillation motion modes.

Furthermore, the hydrophobic Parylene-C coating is useful for preventing the penetration of water in between fingers and anchors if the gap thickness is at most 4 μm . The designs of the whole wafer level gaps are drawn with respect to the limitation, even the gaps between spring beams and the separation of drive, sense and proof mass ports are patterned with maximum of 4 μm apertures.

Also, the proof mass dimensions are considered for amplifying the capacitive sensing signal by increasing the number of fingers as much as possible. The dimensions of the proof mass geometries therefore enlarge in a little aspect.

Additionally, the thickness of the overall active layer silicon, h , is limited with SOI specifications. The stress on the SOI wafer makes the fabrication process extremely hard and possible cause of wafer level breakages. Additionally, even more important, the current injected from the sense port is directly proportional with the thickness of the active layer and decreasing the thickness considerably, will cause overwhelming of the noise over the sensing current signal which will even end the functionality of the device.

Finally, the gap spacing between resonator comb fingers, g , and comb finger width, w_m should be as small as possible, to increase the injected current amount. Thus,

decreasing the gap space between the comb fingers benefit the performance but the fabrication capabilities are the limiting factor at this stage. Also, if the comb fingers are designed too close, the pull-in phenomenon is needed to be considered.

According to the design determinations explained above, 14 different device designs have been proposed. In comparison with the previous generation 6 separate designs, the new designs are planned with more variety in respect of comb finger length and width, spring beam length and width, and proof mass dimensions notably (See Table 2.1 and Table 2.2).

The geometric parameters of all designs are shown in Table 2.1 and Table 2.2. The comparison is done between previous generation resonator designs of D. Eroğlu [71], and represented as “RCD” standing for resonator cell detection devices, and the new generation resonator designs are expressed as “RES” instead of resonator devices. The designs are labeled as RCD #1 to #6 for Table 2.1; and RES #1 to #14 for Table 2.2. Note that the thickness of the resonators is fixed at 5 μm , since the thickness of the active layer of the SOI wafer is the same throughout the wafer.

Table 2.1: Geometric parameters of different resonator designs in the previous generation designs. All dimensions are in μm , if it is not mentioned.

| Name | h | l_m | w_m | g | w_f | l_s | w_s | K [E. μm] | m [ng] | f_n (Comsol) |
|---------------|-----|-------|-------|-----|-------|-------|-------|----------------------------|----------|-------------------|
| RCD #1 | 5 | 40 | 15 | 1 | 1 | 20 | 1 | 0.029 | 8.62 | 810 kHz |
| RCD #2 | | 40 | 15 | 2 | 2 | 20 | 2 | 0.233 | 8.38 | 1.71 MHz |
| RCD #3 | | 80 | 15 | 1 | 1 | 20 | 1 | 0.01 | 15.6 | 540 kHz |
| RCD #4 | | 80 | 15 | 2 | 2 | 40 | 2 | 0.08 | 16.8 | 460 kHz |
| RCD #5 | | 160 | 30 | 2 | 4 | 40 | 4 | 0.08 | 65.2 | 760 kHz |
| RCD #6 | | 160 | 30 | 2 | 4 | 80 | 4 | 0.08 | 74.5 | 260 kHz |

The designs vary in a range of resonance frequency and injected current values to ensure that the readout circuit could be used successfully. The minimum feature size considerations limit the performance of the resonators but the yield is increased considerably and as a result, many of the resonators fabricated are standing after the processes. The resonator dimensions are chosen to enable controlled comparison between different designs with changing each dimension parameter one by one. For example; with RES #8, RES #9, and RES #10, the length of the fingers (l_f) is the only parameter changed and the effect of the parameter can be inspected with these resonator designs. The cross study devices are chosen as RCD #2, RCD #4, RCD #5 of previous design with RES #1, RES #4 and RES #10 of new design resonators. These devices show a slight difference because of the proof mass dimension change.

Moreover, the designs of the wide field resonators are added to the list. The designs of RES #11 and RES #12 have $164 \mu\text{m} \times 64 \mu\text{m}$ proof mass active areas; and the designs of RES #13 and RES #14 have $248 \mu\text{m} \times 128 \mu\text{m}$ proof mass active areas. These large field bioactive areas can increase the binding probability of the antibodies of the functionalization procedure. Thus, the wide field resonators increase the sensitivity in this manner. On the other hand, the mass of the resonator is increased considerably so the mass sensitivity of these devices decreases if we consider the minimum mass sensitivity relation in Equation (2.32).

For comparative reasons, the spring constants, K , and the mass of the resonator m are also included in the tables. As mentioned above, the resonator mass inversely affects the minimum detectable mass sensitivity. Besides, the spring constants are very similar that the anchor and proof mass are chosen to be proportional due to oscillation motion uniformity.

Table 2.2: Geometric parameters of all resonator designs in the final generation (4th generation) designs. All dimensions are in μm , if it is not mentioned.

| Name | h | l_m | w_m | g | l_f | w_f | l_s | w_s | K [E. μm] | m [ng] | f_n (Cmsol) |
|---------|-----|-------|-------|-----|-------|-------|-------|-------|----------------------------|----------|------------------|
| RES #1 | 5 | 44 | 16 | 2 | 21 | 2 | 20 | 2 | 0.010 | 9.02 | 1.41 MHz |
| RES #2 | | 44 | 16 | 2 | 16 | 2 | 20 | 2 | 0.010 | 8.70 | 1.47 MHz |
| RES #3 | | 84 | 16 | 2 | 21 | 2 | 20 | 2 | 0.010 | 16.6 | 944 kHz |
| RES #4 | | 84 | 16 | 2 | 31 | 2 | 40 | 2 | 0.001 | 17.5 | 471 kHz |
| RES #5 | | 84 | 32 | 2 | 31 | 2 | 40 | 4 | 0.010 | 37.1 | 918 kHz |
| RES #6 | | 80 | 32 | 2 | 22 | 4 | 40 | 4 | 0.010 | 34.9 | 948 kHz |
| RES #7 | | 80 | 32 | 2 | 42 | 4 | 40 | 4 | 0.010 | 39.6 | 841 kHz |
| RES #8 | | 164 | 32 | 2 | 22 | 4 | 40 | 4 | 0.010 | 65.2 | 918 kHz |
| RES #9 | | 164 | 32 | 2 | 32 | 4 | 40 | 4 | 0.010 | 67.6 | 859 kHz |
| RES #10 | | 164 | 32 | 2 | 42 | 4 | 40 | 4 | 0.010 | 69.3 | 780 kHz |
| RES #11 | | 164 | 64 | 2 | 32 | 4 | 40 | 4 | 0.010 | 137 | 706 kHz |
| RES #12 | | 164 | 64 | 2 | 42 | 4 | 40 | 4 | 0.010 | 142 | 680 kHz |
| RES #13 | | 248 | 128 | 2 | 32 | 4 | 60 | 8 | 0.024 | 401 | 473 kHz |
| RES #14 | | 248 | 128 | 2 | 32 | 4 | 80 | 8 | 0.010 | 410 | 420 kHz |

2.6 Design and Simulation Summary

The theoretical background of the gravimetric resonator based rare cell detection sensors is explained. Then, the design limitations and the critical parameters for the design geometries are stated. By the support of FEM analysis of COMSOL Multiphysics software the resonance characteristics and operation limitations are simulated. Finally, the 14 different designs of the final generation are introduced. The final resonator designs span a wide variety of resonator geometries for push towards the limitations of the fabrication process flow. If the resonators survive after the procedure they will give a wide range of test opportunity with controlled parameter alternatives. The final design proof masses differ from $44 \times 16 \mu\text{m}^2$ to $248 \times 128 \mu\text{m}^2$, and the natural resonance frequencies span the resonance spectrum starting from 220 kHz up to 1.47 MHz.

CHAPTER 3

FABRICATION

In this chapter, the previous generation fabrication processes and newly proposed fabrication flow of the rare cell detection resonator devices are presented. At the beginning of this chapter, the previous generation process flows are presented in a consecutive manner and the related issues of the previous generation fabrication flows are determined. According to the experiences, limitations, and failures of the previous generation process flows, a new generation process flow for the fabrication of the resonator has been developed. Finally, the problems encountered during the new generation fabrication process flow are briefly discussed and have been solved with the changes in the process flow or with the layout mask modifications.

In all generations of the resonant cell detection devices, the fabrications benefits from the SOI (Silicon-on-Insulator) technology, the glass micromachining, the wafer bonding, and the surface micromachining [71, 72]. The main goal is to fabricate a bioactivated gold site on the resonant sensor. Meanwhile, the first microchannel fabrication is developed and processed with the soft fabrication techniques with PDMS (Polydimethylsiloxane) micromolding. Although, the PDMS soft fabrication techniques are simplistic; the sealing of the bonding site and alignment to the bottom resonators are problematic. Thus, the microchannel formation is achieved with wet etching techniques, curved inside the glass in the final process flow. As the final step of the process flow, a biocompatible polymer with superior properties of electrical insulation and high hydrophobic characteristics is coated on to the suspended resonator devices and patterned. This polymer is Parylene-C and the coating greatly

benefits the insulation and isolation of the resonant behavior with real time and in fluid sensing.

The active layer silicon for the resonator fabrication is chosen to be as thin as possible for decreasing the mass of the proof mass with bioactive site is formed onto. The gravimetric sensor sensitivity can be maximized with smaller mass of the resonator so the relativistic change on the resonant characteristics can be detected.

The first fabrication claim would be a Dissolved Wafer Silicon Micromachining (DWSM) based process with a low cost starting wafer and fabricating the resonator structure with a differing doping distribution on the silicon wafer. The thickness of the silicon resonator device can be determined by this distribution. The structure can be patterned by the Deep Reactive Ion Etching (DRIE) and the resonator can be released by a wet etch with the use of differing etch characteristics of doped and undoped silicon layers. Although, the DWSM process is advantageous with the low price of fabrication; the wafer level uniformity of the DRIE patterning can be problematic from the beginning. Also, the precision of the doping characteristics of the systems will result in varying thicknesses of resonator devices which will cause losing the reproducibility and equivalency of the processed devices.

Consequently, a 5 μm active layered SOI is preferred as the starting root wafer. The SOI wafer oxide layer can be used as an etch stop layer for DRIE patterning and the reproducibility and equivalency of the resonator structures can be achieved with this specialized wafer. The buried oxide layer can also be used as a sacrificial layer for releasing suspended devices like resonators. Also, nowadays MEMS top-down mechanical or chemical micromachining techniques can not achieve uniform layer, as required, down to 5 μm with grinding, lapping or polishing [73]. The SOI wafer active layers can be manufactured down to 3 μm for 4" wafer but the uniformity of the final grinding cause problems and a slight increase of the thickness to 5 μm active layer benefits considerably both for final uniformity and the fabrication constraints. In all generations, the 5 μm active layer silicon of SOI wafers with 2 μm buried silicon oxide layer and a 350 μm silicon back handle layer are used henceforth.

The second main requirement for the gravimetric resonant sensors would be the reliable signalization with the device layer and the control electronics with a low noise and parasitic capacitance characteristics for the proper capacitive actuation of the resonator based sensors. Different methods of intermediate insulating parylene layer or suspension bridge like conduction of metal layers are tried throughout the fabrication flow generations.

Parylene coating is the main insulating layer with the high conformal coating possibility and the biocompatibility around the sensor. Also, parylene is benefited for the hydrophobic characteristics and in fluid measurement of the resonators. Even so, the parylene coating is the trickiest point of the gravimetric resonator cell detection devices. The proper insulation should be done after the devices are released and then parylene can penetrate in between the fingers and anchors of the resonators and also insulate the microchannel for parasitic affects.

Finally, the microchannel formation with proper microfluidic characteristics is crucial for the choice of the fabrication steps. The microchannel should be aligned to the resonator structures with lowest possible contact area to the outer silicon structures and gold contact lines for the signalization. In order of fluid flow, the channel has to be sealed strongly for holding fluid under continuous flow. The microchannel have to be wide and deep enough for cells to be flood without any clogging affect; and contrarily the microchannel have to be low volumetric for decreasing the required volume of examining fluid sample.

3.1 Previous Generation Process Flows

Originating from the first designs of BioMEMS group's rare cell detection devices, we are aiming to develop a gravimetric resonator based sensor with a high mass sensitivity with a bioactive gold layer on top of the resonant sensor proof mass [71, 72]. Also, the sensor is advantageous with an insulating and hydrophobic coating of Parylene-C. Through past years there were some generations of designs that we tried to generate a design with attributes of biocompatibility, reproducibility, low cost, and

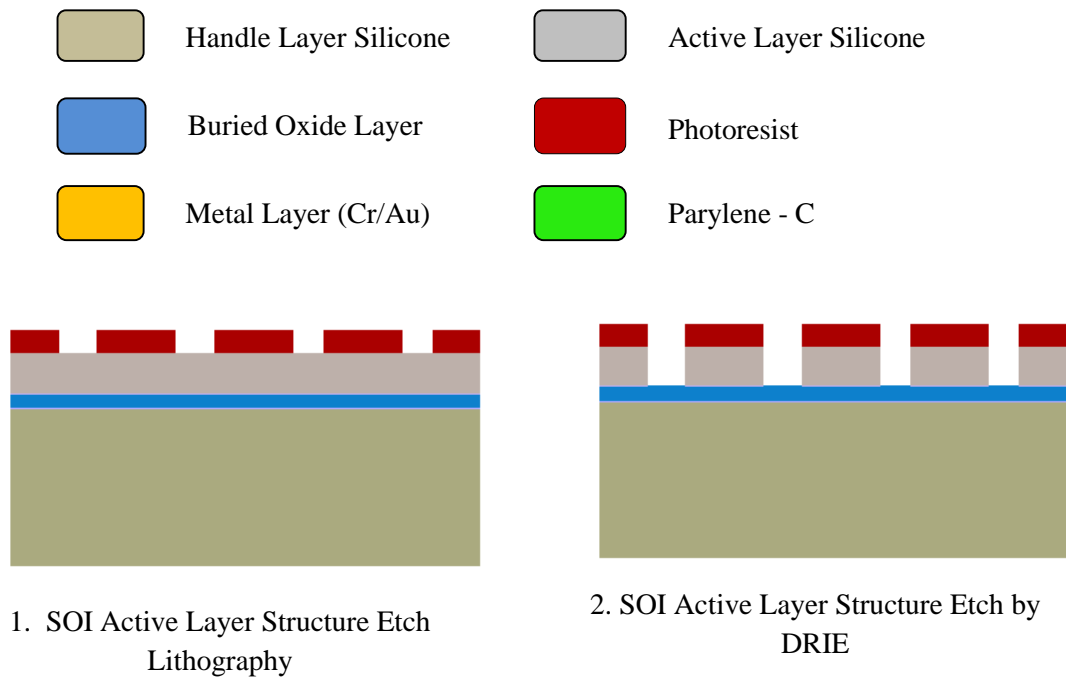
high fabrication yield. There were three generations of designs proposed, fabricated and investigated before. In light of the foregoing, the 4th generation design is proposed and solved many problems occurring in the past processes. Still, understanding the previous designs is beneficial for explaining the improvements and advantages of the final generation of process flow proposed.

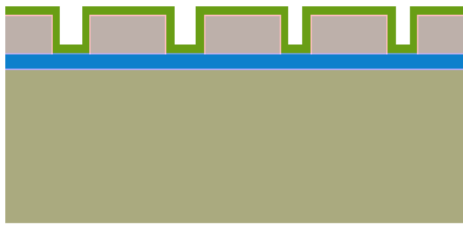
The first process flow base on a single SOI wafer with all the connections and resonator structures are designed on the wafer itself. The second process flow makes use of the anodic bonding technique and the handle layer is the glass wafer underneath. So the handle layer of the SOI can be removed. The third generation process flow take root of the glass wafer handle layer design but the contact lines are also buried inside the glass wafer through recess gaps and a different perspective of sacrificial layer is proposed. On the other hand, the parylene coating as a general isolation layer is added to the procedure but the parylene patterning on the suspended structures cause a drastic loss of working devices. There were some steps that the process engineer could not actively control the efficiency of the result of the procedure. Thus, the ultimate process goal become achieving some working devices out of a whole wafer.

The 4th and the last generation process flow benefits from a more straight forward point of view which gives the efficiency control to the production engineer. The flow makes benefit of the anodic bonding and the glass handle layer approach and also the parylene coating for the isolation and insulating the resonators from the flowing fluid. Additionally, the microchannel is carved inside the glass wafer and the resonator active sites are facing inside the glass wafer gaps.

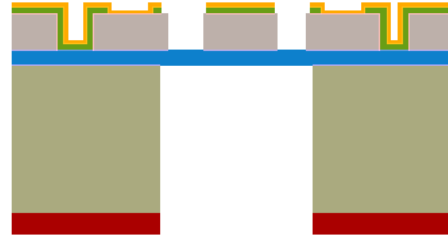
3.1.1 First Generation Process Flow

The first generation process flow bases on a single SOI wafer with all the connections and the resonator structures are designed and patterned on the wafer active layer itself [72]. The flow starts with the patterning of the SOI active silicon layer with DRIE etching. The sharpness of the lithography is crucial on this step that the structure layer which forms the resonators with 1 μm feature size. After this step, the SOI wafer is etched under DRIE down to the buried silicon oxide etch stop layer. The etch uniformity is provided with the buried oxide layer but there is a trade off on this issue; the oxide layer also results in notching affect which damages or thins the finger and anchor springs of the resonators. The process flow used to fabricate the first generation resonators is given in Figure 3.1.

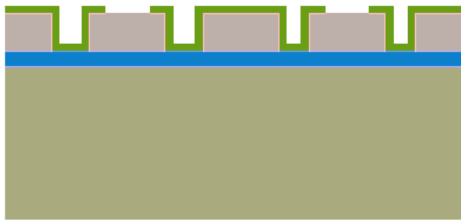




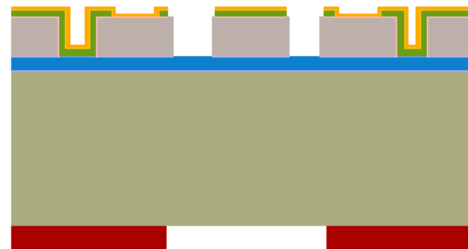
3. Coat Parylene - C Polymer with Parylene Coating System



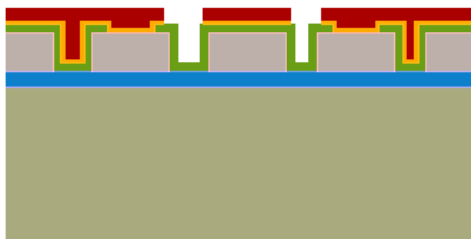
6. Parylene- C Etch with Metal Masking by RIE and Backside Lithography for Release



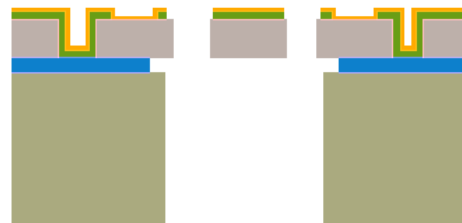
4. Lithography and Pattern Parylene - C with Reactive Ion Etching (RIE)



7. Backside Handle Layer Etch by DRIE



5. Cr/Au Metal Coating with Sputtering and Pattern Metal with Wet Etch



8. BHF Release of the Resonators from Both Sides of the Wafer

Figure 3.1: First Generation Process Flow.

After the structural layer is patterned by DRIE, a conformal coating of Parylene-C polymer is done as an insulating layer before the metallization is done on to active silicon layer of the SOI wafer. The Parylene-C is coated by PDS 2010 Parylene Coating System which is basically a Low Pressure Chemical Vapor Deposition System (LPCVD). Then, Parylene is patterned with a lithography process and dry

etching under RIE system with masking layer of photoresist. Afterwards, Cr/Au metal coating is done under Sputtering system. Chromium layer is coated as an adhesion layer for conducting gold layer. Another choice could be titanium for the adhesion layer but the cleaning procedure with the piranha ($\text{H}_2\text{SO}_4:\text{H}_2\text{O}_2$ - 1:1) solution and release procedure with buffered hydrofluoric acid (BHF, $\text{HF}:\text{NH}_4\text{F}$ - 1:7) etches away the titanium layer underneath. The metal layer is patterned with lithography and wet metal etch technique. The metal layer is also used as a mask for cleaning the Parylene-C remaining between resonator fingers and anchor sites under RIE dry etching.

The remaining residues of parylene and metal between fingers hinder the release step under BHF so the wafer handle layer is etched down to buried oxide layer with backside aligned lithography. Under DRIE with photoresist masking, the resonator sites are patterned. Then, etching the silicon oxide layer and so the release of the resonators with BHF and drying steps under hot methanol drying method are done consecutively. The backside etch of the handle layer is developed after it is observed that the etch rate with only penetration through fingers and anchors are not enough for BHF release. The release site optimizations have been the major setback for this procedure. The release could not be done without increasing the BHF etch time periods considerably and this create a high over etch rate under the anchor sites of the resonators which even cause breakages.

The etch sites formed through the backside handle layer result in a different problem. These holes prevent the vacuum holding of the wafer and further processes or measurement probe setup applications become highly difficult or even impossible.

The DRIE notching effect is one of the major problems for this procedure. The notching effect is the undesired over etch under the DRIE etched walls with ions reflecting from insulating buried silicon dioxide layer of the SOI. These ions continue to over etch the DRIE patterned structure after the active layer silicon is etched. The notching effect is observed and inspected deeply in [74], and this effect is shown in Figure 3.2. The DRIE passivation and etch cycles have to be optimized for preventing this effect. Also, the varying gap spaces under DRIE etch fields create the non-uniform etch rates and fast etched sites become more open to this problem.

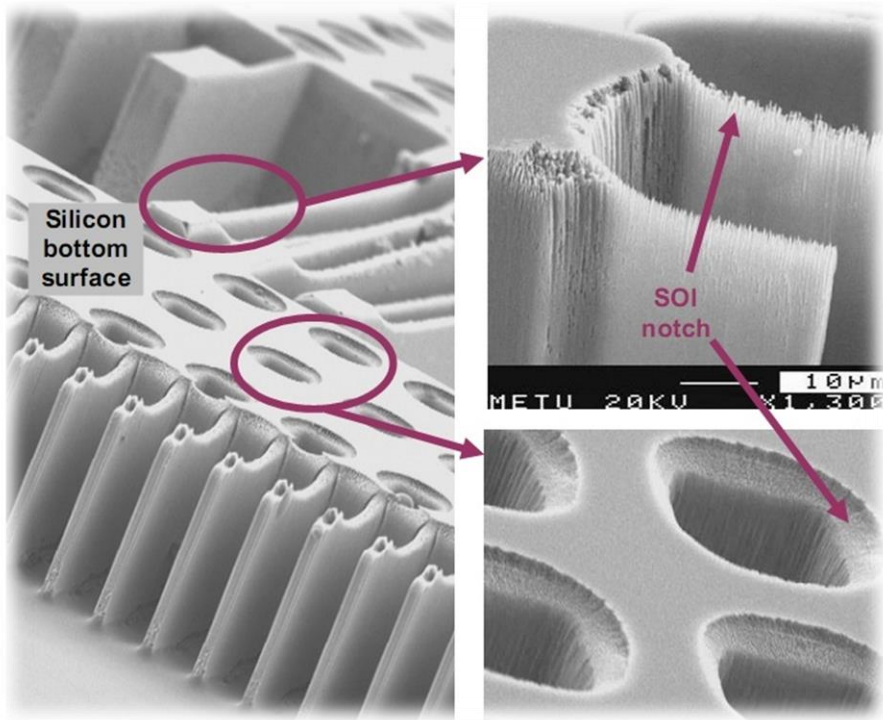


Figure 3.2: Illustration of DRIE Notch Effect [74].

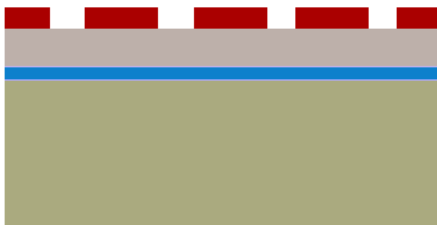
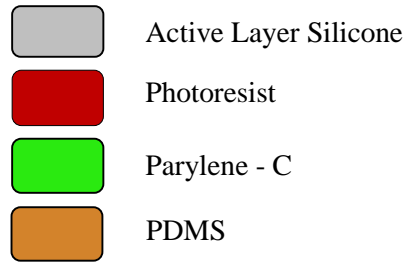
Nevertheless, the parylene coating brings up some final problems for the procedure. There is an adhesion problem coming from the low adhesive characteristics between gold and parylene. Parylene is easily peeling off during some wet procedures. Also, parylene will not withstand temperatures higher than 95°C which is relatively low temperature for the standard MEMS fabrication techniques. This limitation of the parylene layer hinders the process engineer for some necessary over heating steps. Therefore, the soft and hard baking steps are rearranged and the device parylene layer hydrophobicity characteristics are protected.

3.1.2 Second Generation Process Flow

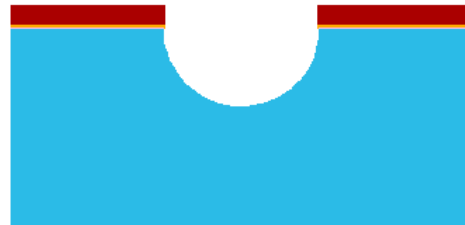
The second generation process flow makes use of the anodic bonding technique and the handle layer becomes the glass wafer underneath [72]. So this allows the handle layer of the SOI to be removed and the structures are still remaining durable. The new procedure is similar to the first generation SOI only process flow as the formation of the resonators on the SOI wafer. The major difference is patterning a glass wafer with recess gaps for the suspended resonators to move freely. The process flow used to fabricate the second generation resonators is shown in Figure 3.3.

The process starts with the lithography and the patterning of the active silicon layer of the SOI wafer. Then, separately, the glass wafer is coated with Cr/Au metal layer for wet etch protection layer. Lithography for the metal etch is done and the metal masking layer is patterned with wet metal etch chemicals. Afterwards, pure HF etch is done for shaping the recess gaps which will be aligned under resonator sites.

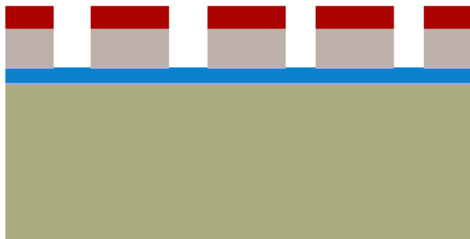
As the intermediate step, the structure patterned SOI wafer and the recess gap patterned glass wafer are aligned to each other and wafer bonded with anodic bonding of glass to silicon. With the use of EVG 501 wafer bonder, the substrate silicon is biased with 1000V, 1500 N piston force is applied on the glass and silicon wafer pair, and 400°C of bonding temperature is applied on the substrates of the wafers. Then, the backside handle layer is etched away with DRIE and with patterning metal mask; the buried oxide layer is etched with RIE or BHF. The RIE dry etch will be more confine for this step but there is a remaining residue of burned photoresist which could not be removed. On the other hand, BHF wet etch of the oxide layer is a cheaper way but with high undercut over etch trenches. Then photoresist is stripped and Cr/Au metal is sputtered for metal routing metallization. Metal coating is patterned and the metal connections are formed from the contact sites of the structure to the wire bonding contact pads of the devices. Finally, the buried oxide layer is wet etched under BHF solution for releasing the devices.



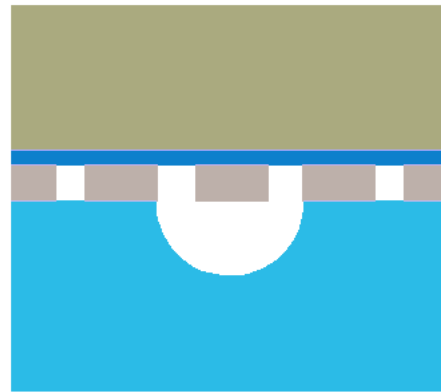
1. SOI Active Layer Structure Etch
Lithography



4. Lithography and Pattern Metal Masking
Layer, and then HF Wet Etch of Glass
Recess Gaps



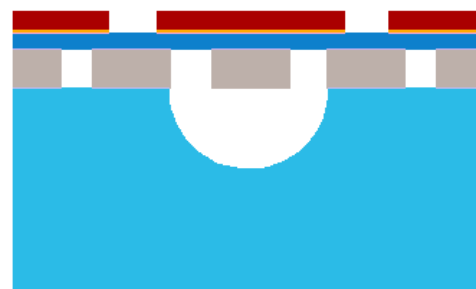
2. SOI Active Layer Structure Etch by
DRIE



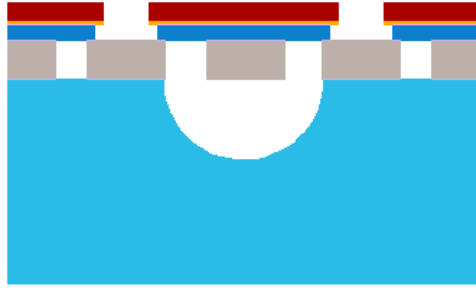
5. Anodic Bonding of the Patterned Glass
and the SOI Wafers



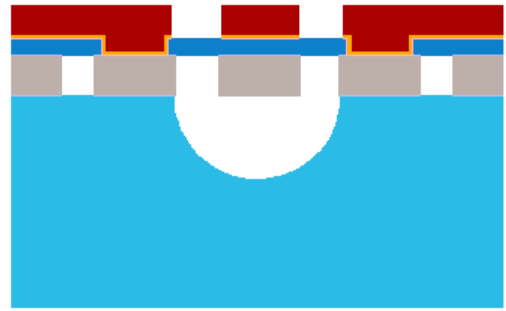
3. Cr/Au Coat of the Glass Wafer for the
Metal Mask for the Glass Wet Etch



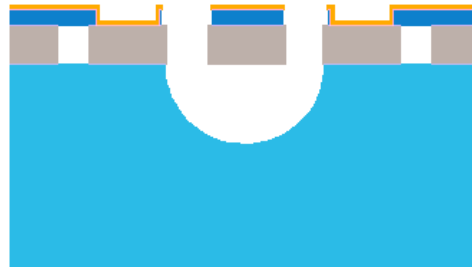
6. Remove Backside Handle Layer Silicon
Under DRIE



7. Metal Coat and Pattern Metal Mask Layer and Pattern Buried Oxide Layer with RIE or BHF



8. Metal Coat on Contact Opening and Lithography for Metal Routing



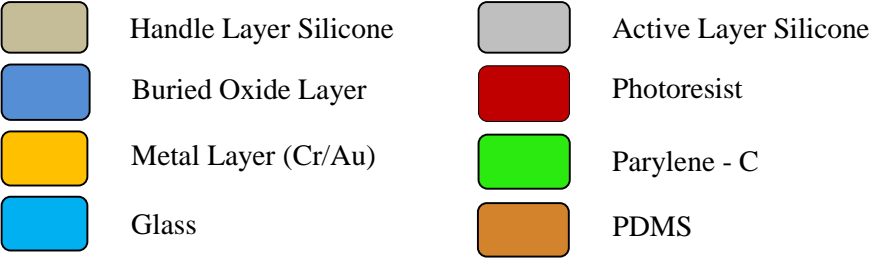
9. Oxide Patterning and Release the Resonators under BHF

Figure 3.3: Second Generation Process Flow.

After this device fabrication, the microchannels are created separately with a different soft lithography technique of PDMS micromolding. The process steps for the fabrication of the microchannel on top of the resonator devices for the second generation resonators are shown in Figure 3.4.

In this procedure, a prime silicon wafer is etched under DRIE for PDMS micromolding. The PDMS (Polydimethylsiloxane) molding technique is a well known and cheap technique for creating biocompatible microchannels. The silicon wafer will be used as a master wafer for the molding patterns and this wafer can be used repetitively after single DRIE etching. Then, widely known soft lithography procedure starts with pouring PDMS on top of DRIE patterned silicon master wafer. The PDMS will be degassed and cured on top of this master wafer. Then, the pattern

will be mirrored on to the hardened PDMS mold structure. PDMS mold is then peeled off from the silicon master and after oxygen plasma activation of the PDMS mold, the microchannel is aligned and bonded under optical microscope.



1. Lithography for DRIE Patterning of the Silicon Master Wafer



3. Pour, Degas, and Cure the PDMS Mold on to the Master Silicon Wafer

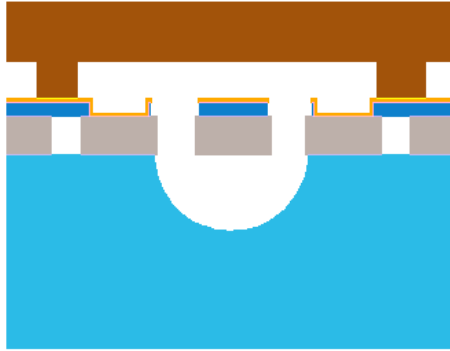


2. DRIE Etch of the Silicon Master Wafer for PDMS Molding



4. After Curing Peel Off PDMS Mold as a Whole Wafer

Figure 3.4: PDMS Microchannel Preparation for Second Generation Process Flow.



5. Plasma Activate and Bond PDMS Mold on Resonator Devices in Die Level

Figure 3.4: PDMS Microchannel Preparation for Second Generation Process Flow.

(continued)

The second generation fabrication flow has some major problems which prevent the resonators work properly. Also, the parylene-C coating is eliminated due to some fabrication problems and low rate of remaining standing suspended structures. The insulation and isolation coating of parylene-C does not exist; so in fluid applications with these devices would be highly problematic with the capacitive and shorting effects of the fluid conductivity. Additionally, the design is not benefiting from the

The first major problem is the resistive coupling of the metal lines between drive and sense ports of the resonators. Moreover, the adhesion strength of the wire bonding pads is not achieved to be low. Thus, the connection metal routing lines are not working properly through the devices.

The oxide layer remaining under the bioactivation gold sites also etches and causing the bioactivation areas to be lift-off after long BHF release etch. Thus, the bioactivation of the gold could not be preserved. Nevertheless, primal resonance characterization tests have been conducted with clean silicon resonators [72].

3.1.3 Third Generation Process Flow

The third generation process flow take root of the glass wafer handle layer design but the contact lines are also buried inside the glass wafer through recess gaps and a different perspective of sacrificial layer is proposed [71]. This solution is proposed for solving the resistive coupling problem of the drive and sense ports of the devices. On the other hand, the parylene coating as a general isolation layer is added to the procedure but the parylene patterning on the suspended structures cause a drastic loss of working devices. Parylene-C is used for the hydrophobic insulating and isolating coating on the structures. Additionally, separate masks and steps are conducted to open the proof mass gold area and the bonding pads for preventing some plasma damage on the wire bonding pads. The process flow representation can be investigated in Figure 3.5.

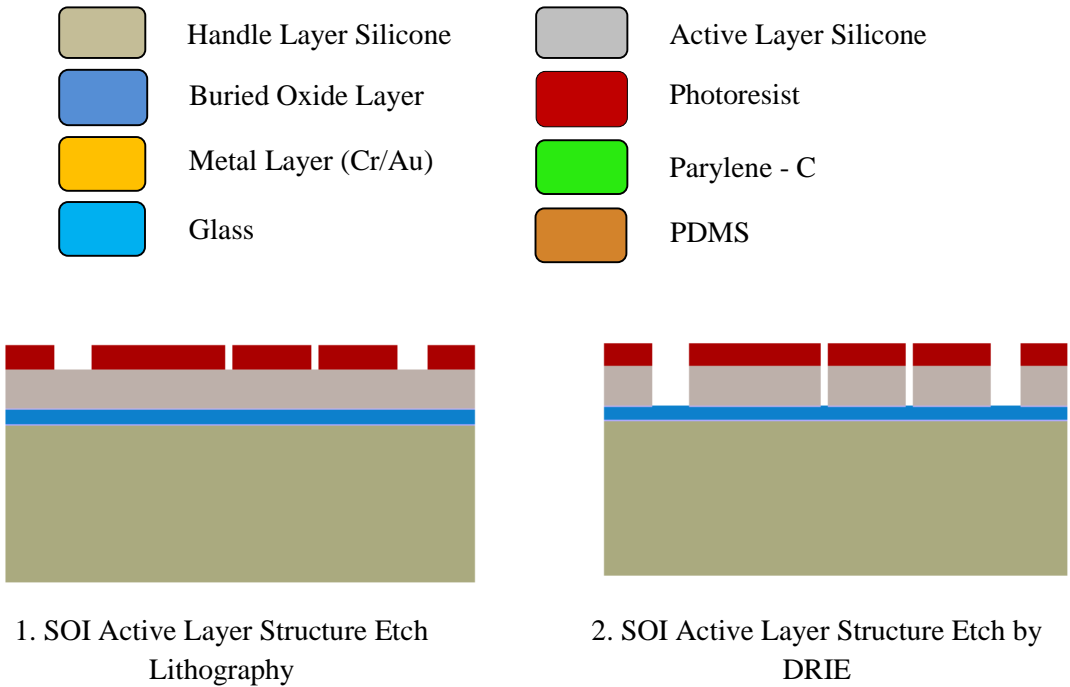
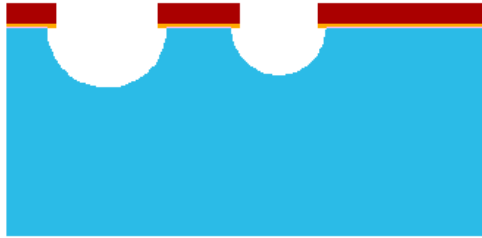


Figure 3.5: Third Generation Process Flow.



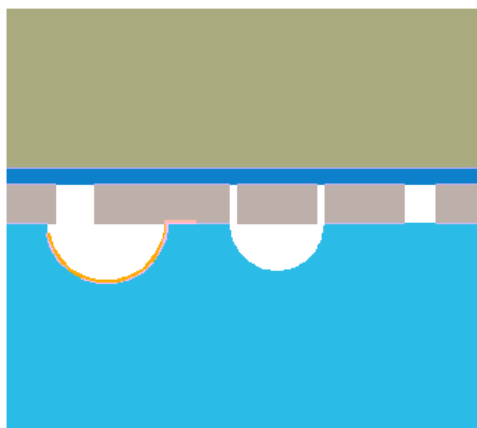
3. Metal Mask Coat and Lithography for Recess Etch on Glass



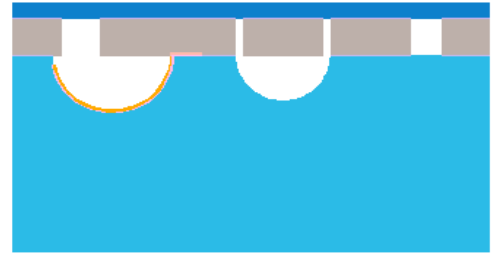
4. Recess Gap Etch on Glass with Metal Mask Under pure HF



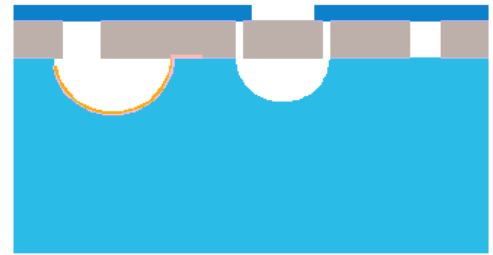
5. Routing Metal Lines Coat and Pattern Inside Recess Gaps



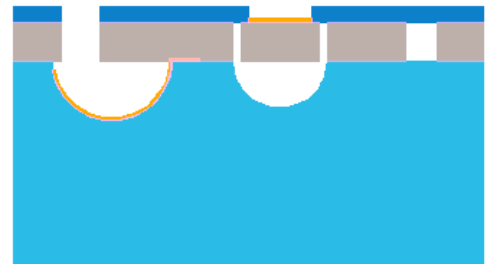
6. Anodic Bonding



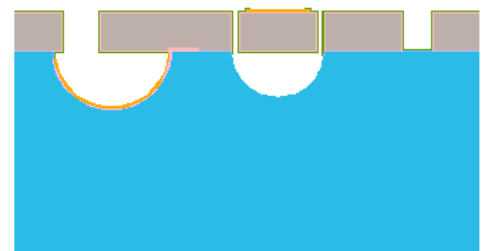
7. Backside Handle Layer Removal in DRIE



8. Buried Oxide Layer Etch on Resonators with RIE



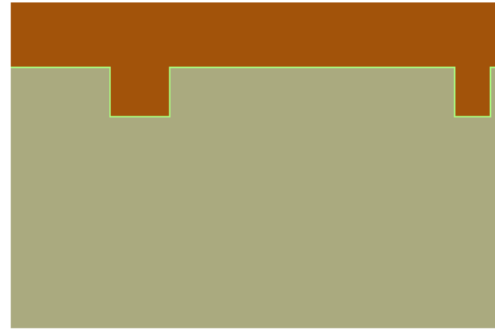
9. Bioactivation Metal Coat and Pattern on the Proof Mass of the Resonators and Pad Window Opening



10. Release the Resonators Under BHF, Parylene-C Coat and Pattern on the Bioactivation Metal



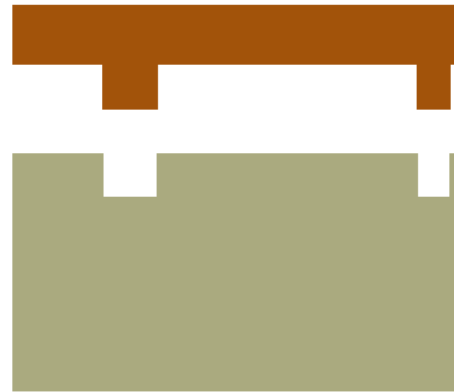
11. Lithography for DRIE Patterning of the Silicon Master Wafer



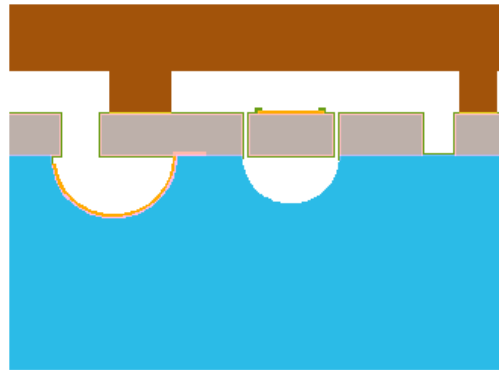
13. Pour, Degas, and Cure the PDMS Mold on to the Master Silicon Wafer



12. DRIE Etch of the Silicon Master Wafer for PDMS Molding



14. After Curing Peel Off PDMS Mold as a Whole Wafer



15. Plasma Activate and Bond PDMS Mold on Resonator Devices in Die Level

Figure 3.5: Third Generation Process Flow. (continued)

The process starts with a resonator structure formation with DRIE dry etching after lithography of the structure patterns (See Figure 3.6). In parallel, the glass is etched for the recess gaps with the usage of metal masking layer. Lithography for the metal etch is done and the metal masking layer is patterned with wet metal etch. Afterwards, pure HF etch is done for shaping the recess gaps which will be aligned under resonator sites for obtaining resonator suspension. The issue for this step is HF etch sites of the wafer level non-uniformity and lateral etch of HF under metal mask layer (1:1.6 - deep through: sideway). The setup do not allow us to take out the wafer in the same way, so this cause reproducibility problems.

Then, a new Cr/Au layer of the metal contact lines and pads are coated and patterned inside this isolation recesses. During the glass recess etch, the recess gaps for the metal contact lines are also etched and so the metal lines are buried inside the glass wafer for preventing resistive coupling mentioned in the 2nd generation flow.

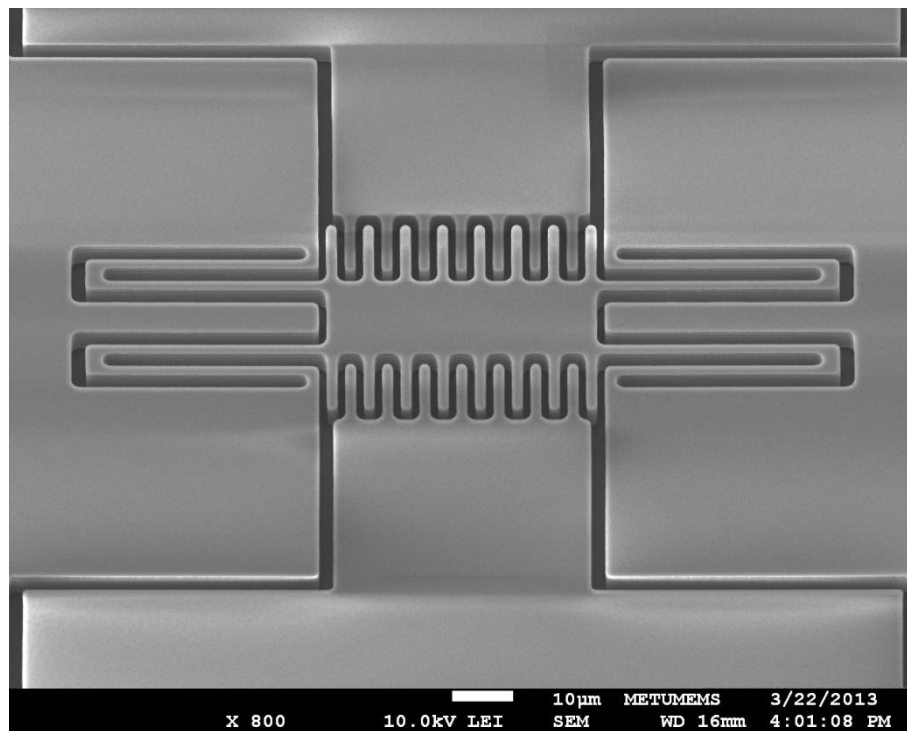


Figure 3.6: SEM image of the 3rd generation resonator device after DRIE structure is etched.

At this point, the separate wafers of SOI and glass are patterned and ready for anodic bonding. Piranha cleaning for the both SOI and glass wafers are done and additionally, another very short BHF native oxide etch is done for SOI wafer. Right after this native oxide etch, the anodic bonding alignment is done and without delaying the bonding is performed at 350°C, 1200 V is applied to the wafers and a piston force of 1500 N is used. No flags are put in between the wafers or another method are used to be able to apply the bonding voltage to the SOI device layer [75].

Afterwards, the handle layer is removed with DRIE dry plasma etching and the most problematic part of this flow starts. The thin and stressed oxide layer will be holding the resonators during many wet and plasma processes after the handle layer removal. This creates cracks throughout the wafer and will cause drastic loss of working devices at the end. Then, the buried oxide layer is patterned and the bioactivation sites will be etched with RIE for gold layer to be contact the resonator silicon layer for preventing peel off like in the previous generation process flows. As mentioned, next step is coating Cr/Au metal layer and with a lithography and wet metal etch, the bioactivation metal sites are patterned on top of the proof mass of the resonators. Then, another wet process of pad opening window lithography is done and the pad windows are etched with consecutive steps of RIE for 2 μm buried silicon oxide etch and DRIE for 5 μm active silicon etch. The process continues with the release of the resonators with BHF wet etch and methanol drying steps.

As the final step, parylene-C is coated with parylene coating system and lithography on suspended devices is done for parylene to be etched under RIE for cleaning the gold on top of the bioactivation sites of the resonant sensors.

The thin parylene layer is to open the top field of the proof mass of the resonators, for allowing cells to be captured on the gold layer. Another lithography with wet processing is done and a final RIE is applied for etching the openings of the parylene layer. The resonators are released at this step, so the processes required to be done very carefully. Also, a thick spin coating of positive photoresist, SPR 220-7, is used for this step for properly removing parylene under RIE before the removal of the photoresist masking layer. The processing of this thick photoresist cause trouble and

the soft baking of the devices are done by gradually increasing the temperature to prevent breakages due to outgassing of the resist and inner microchannel air traps.

To sum up, for the 3rd generation fabrication flow, there are some steps that the process engineer could not actively control the efficiency of success of the throughput of the procedure. Thus, the ultimate process goal become achieving some working devices out of a whole wafer.

3.1.4 Problems with the Previous Generation Process Flows

There are many setbacks for the 3rd generation process flow which hinder the general performance of the biosensors. The first issue is the DRIE process time optimization of the notching effect. There is a fluctuation of the etch rate of the system so the procedure is lacking the inspection under SEM by which etch of the device can be assured with proper quality. The trials for the DRIE etch time optimizations are started from the beginning for the preparation of the 4th generation process development. The devices are etched with DRIE in varying etch rates and periods and the etch profile is deeply inspected. In Figure 3.7, dry etch of the bare silicon wafer can be observed from a broken side on the anchors. The notching effect is a major problem in the past but incomplete etch under DRIE can be also problematic at the final step of the releasing the resonators. The Figure 3.8 shows the semi developed resonators caused by this under etch issue. Under SEM inspection, the Figure 3.9 indicates the remaining residue of the active silicon layer on top of silicon dioxide layer. Actually, there is a trade-off that these residues are the counter issue for the notching effect which cause loss of the resonator finger and anchor structures. After the optimizations, both the notching and under etch issues are solved (See Figure 3.10). The SEM inspection is also required to be added to the process flow as a fundamental step for the next generation process flow.

Additionally, the active device layer resonator structures are processed with a mask of differing thickness of lines around resonator sites. This issue prevent appropriate results with the optimization of the DRIE etch rates and that will cause the resonators

to be weakened and thinned at the anchor parts, in DRIE etching of the active silicon layer.

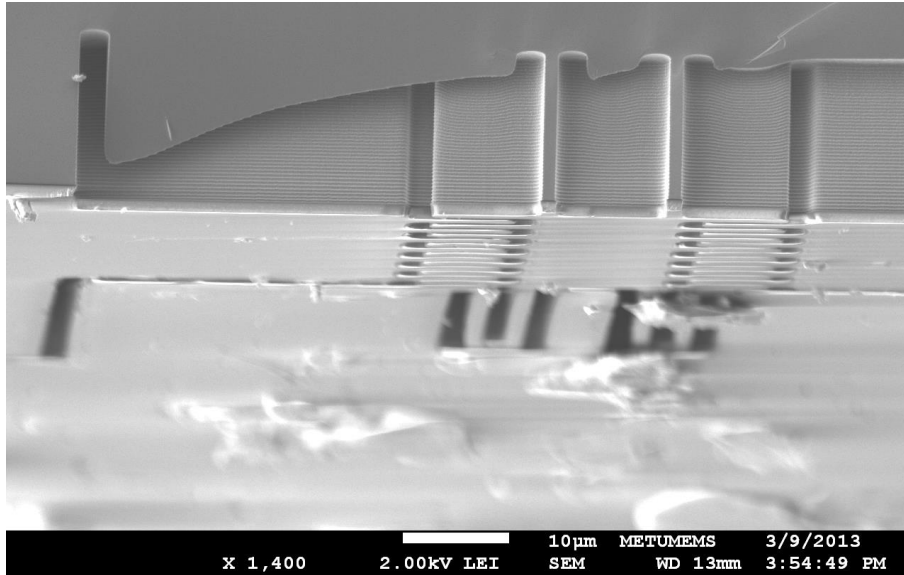


Figure 3.7: Broken wafer for the inspection of DRIE etch profile optimization trials for the prevention of the notching effect.

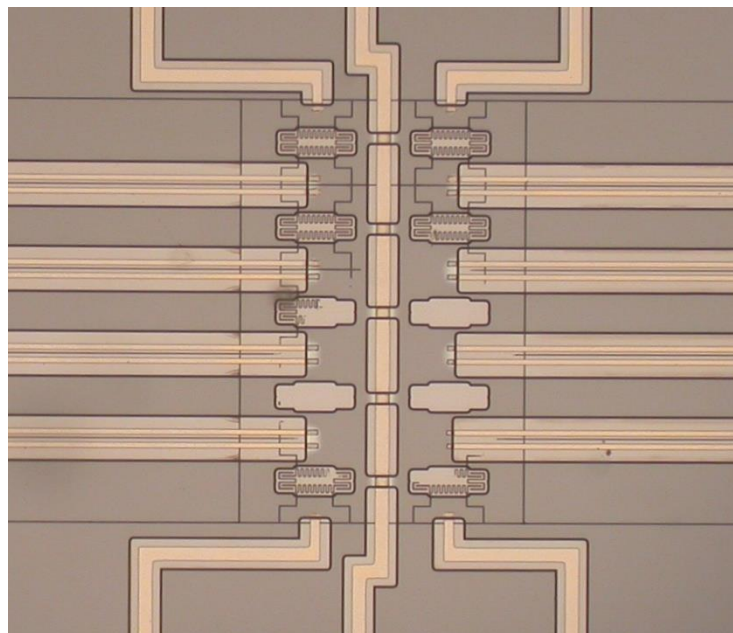


Figure 3.8: Active silicon layer is not etched completely and the resonators are not formed properly with under etch in DRIE.

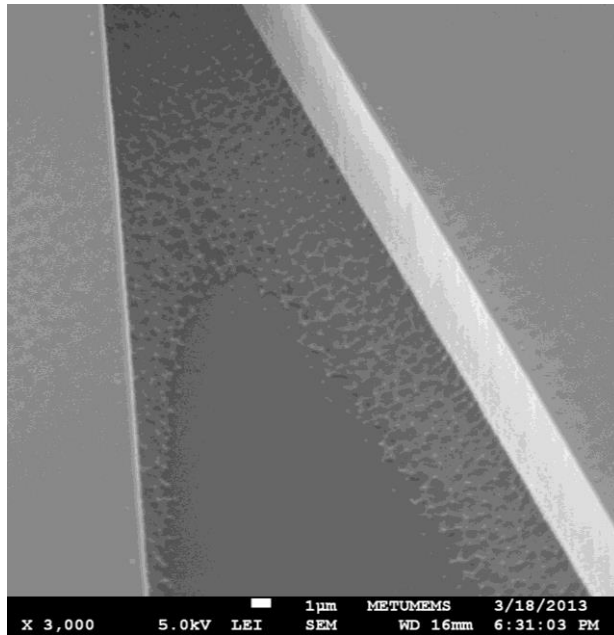


Figure 3.9: Remaining silicon residue after DRIE etch on the varying etch spaces without optimization. These residues are the counter issue for the notching effect which cause loss of the resonator finger and anchor structures.

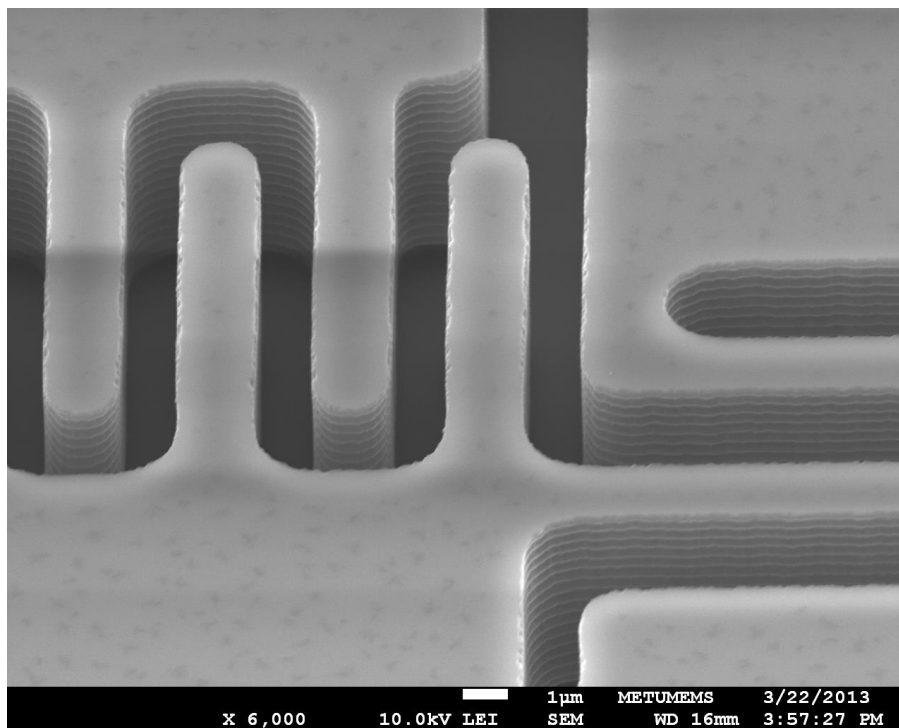


Figure 3.10: Proper etch on the corner sites of the anchor and fingers after optimizations are done for the specific structure mask of the resonator features.

The second issue for the 3rd generation fabrication flow is the anodic bonding causing high rate of burning and sparking between fingers of the resonators and metal lines, resulting in huge amount of loss of the contacts and resonator finger damages as represented in Figure 3.11. This can be solved by connecting all wafer level lines for whole wafer. (See Figure 3.12a for the previous generation metal mask and Figure 3.12b for the new metal mask) The second issue is the pad line hindering of the metal layer on the drive and sense electrode anodic bonding area, we need to shorten the lines, so the area of bonding can be increased.

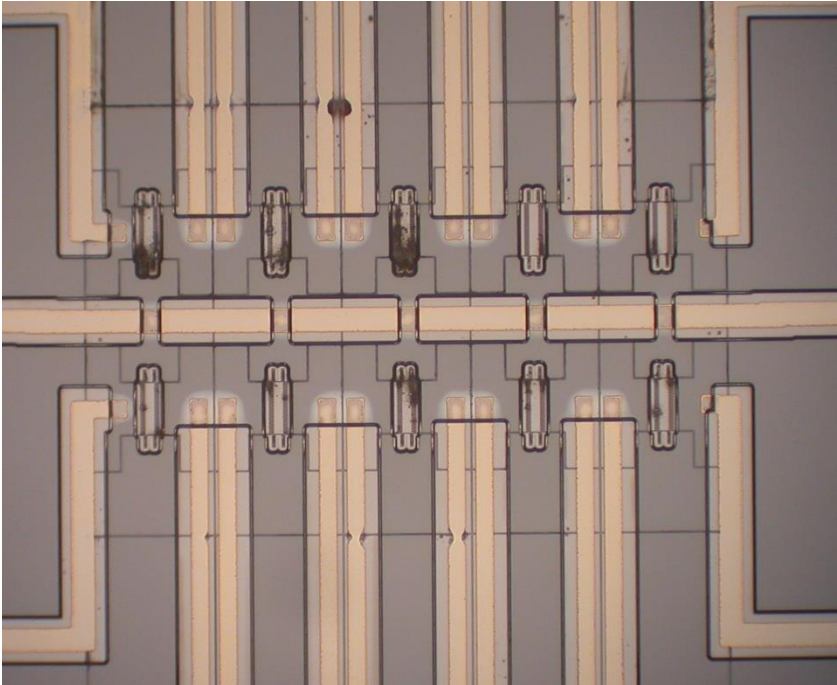


Figure 3.11: After anodic bonding due to floating areas on the bond surface, high rate of burning and sparking between fingers of the resonators and metal lines, resulting in huge amount of loss of the contacts and resonators

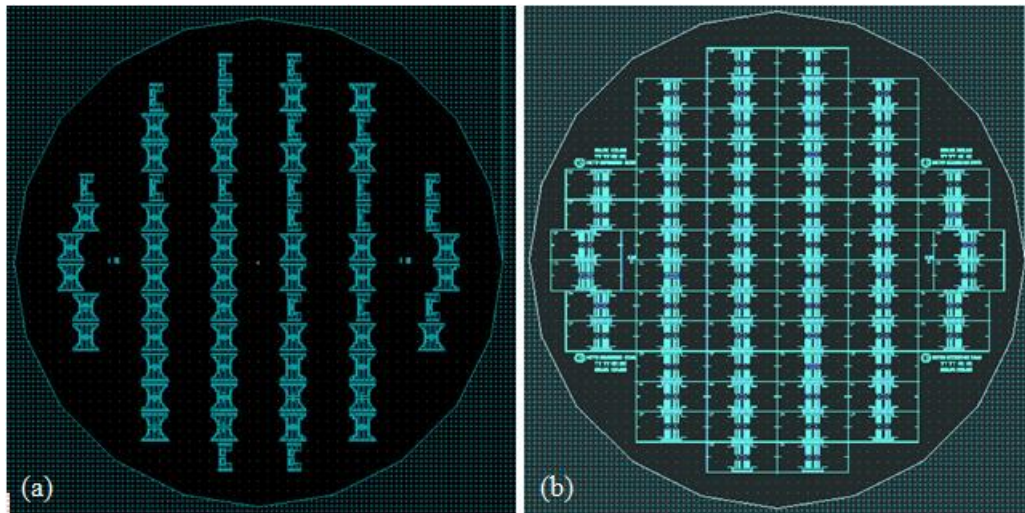


Figure 3.12: (a) Metal routing lines mask can be seen, the die level metal lines are not connected so at the state of the anodic bonding, there are many floating pads remaining on the active silicon layer of the SOI and this results in sparking during the anodic bonding. (b) Metal routing lines mask can be observed for the 4th generation flow, the die level metal lines are all connected in the new design. Also there are no floating areas remaining.

Moreover, the ruptures of the oxide layer were observed especially in the bond pad regions (See Figure 3.13). The main reason for these ruptures is the overheating at the step of DRIE etch with only 2 μm stressed oxide layer is supporting the nearly suspended structures. In order to solve this issue, modifications have been made in the DRIE and glass recess masks. The arrangements of the layout solved the issue in some extent, but the fact of the very weak and stressed layer of buried silicon dioxide layer of the SOI continue to cause problems. Even so, the solution adds another mask and an additional wet lithography process so the problem continues. The stress on the oxide and many compulsive wet processes do not allow the solution to work, so for the next generation process flow we need to consider a new point of view for reaching and contacting the metal pads.

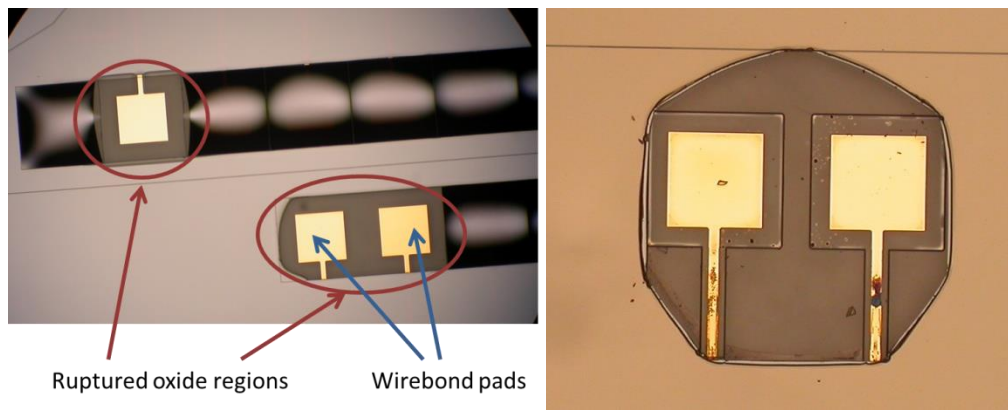


Figure 3.13: Rupture oxide regions above bond pads after backside DRIE. [71]

After the backside handle layer removal with DRIE, a window is aimed to be opened on the oxide layer on the proof mass. This is done under RIE dry etching. Another problem related with the oxide layer emerged at this step. Throughout the wet lithography processes the oxide cracks and the liquids penetrate from these cracks and cause bubbling or wide ruptures on the photoresist and the oxide layers. As a solution, an additional 200 nm oxide layer is deposited under PECVD with low stressed mixed frequency recipe. This additional layer of oxide is aimed to fill the the cracks and seals the microfractures in some aspect and increase the number of functional devices. Although, the solution works slightly, it does not increase the functional device number considerably (See Figure 3.14). On the other hand, the new process mask set is drawn under consideration of this issue so the breakages do not occur even if the additional oxide layer is not introduced.

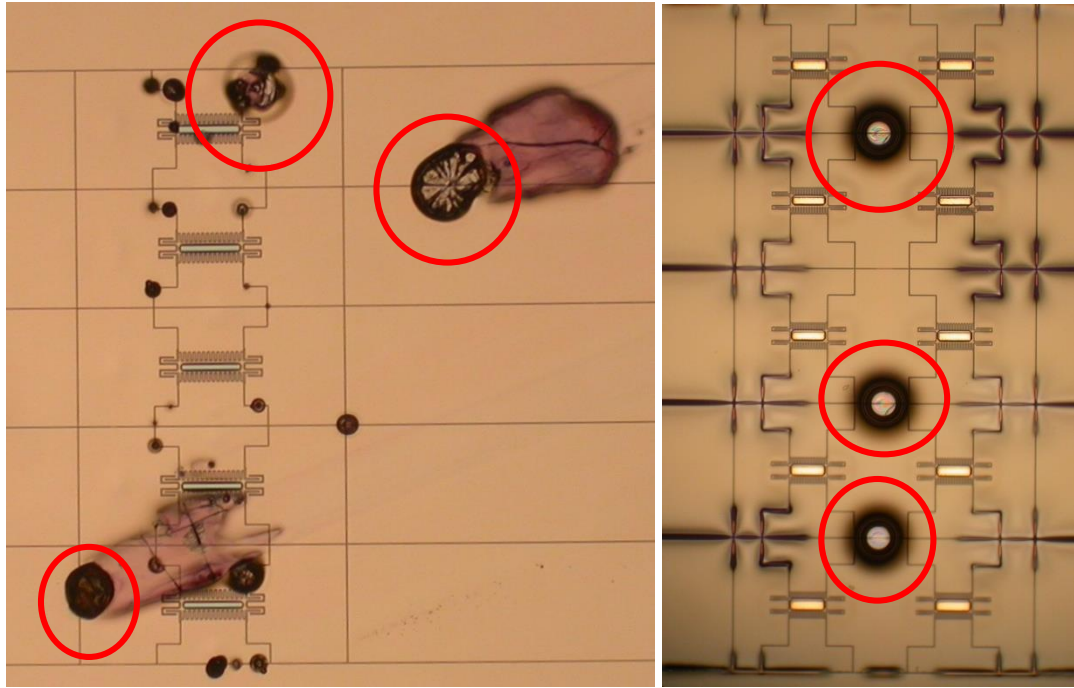


Figure 3.14: After the lithography, photoresist penetrated the oxide layer through microfractures marked with red throughout the wafer and again rupture the oxide layer after the baking step.

The final steps of BHF release and the parylene patterning are the last wet processes which are the most catastrophic steps of all. The suspended resonators can not withstand the effect of these consecutive steps. Most of the resonators are lost at these steps. At the last steps, with suspended structures, the choice is always on the side of dry process but the long oxygen plasma processes damage the chromium adhesion layer underneath the bioactivation gold site, and BHF release step can undercut the and leaving bare silicon. As seen in Figure 3.15, the gold on top of the many proof masses are lifted off. On the other hand, the bond anchor sites of the drive and sense ports are not proper for these applications. The ports can easily be broken after BHF release etch and result in another loss of device (See Figure 3.16).

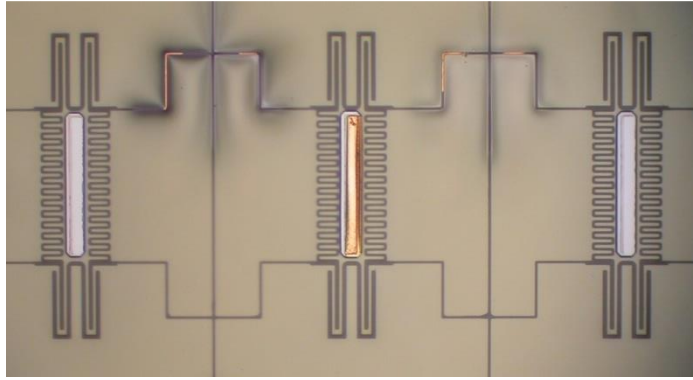


Figure 3.15: Chromium is etched under long oxygen plasma steps for photoresist strip and the bioactivation gold site on top of proof mass of the resonators are lifted off.

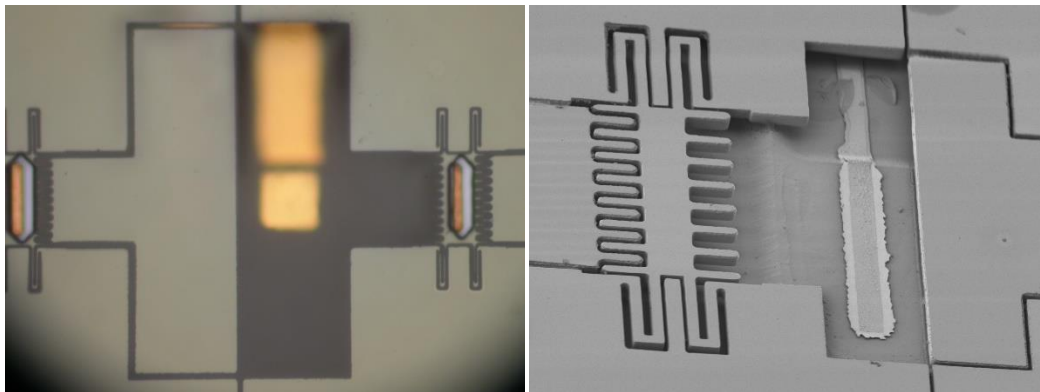


Figure 3.16: BHF release wet etch undercut the bond sites glass and the weak spots like gold connection areas are vulnerable for breakage.

The major problem of this process is thinning the backside handle layer silicon at the very beginning of the process. This causes cracks on the SiO_2 and even breakages of major parts. This restricts our opportunity of reproducing the process or stripping a misalignment. Thus prevents the wet processes success. Even at the last step, we do two processes of wet and photolithography with thick photoresist and at this stage the pads and released layers are opened and fluid easily penetrate through the recess lines.

The requirement of decreasing the number of wet processes after anodic bonding imposes us to choose dry oxygen plasma instead of wet PR strip. However, the Cr adhesion layer is slowly etched with a considerable under cut. As a result, at the final

step of releasing in BHF, the bioactivation Cr/Au pads raptured. If we continue with this process, we need to increase the chromium (Cr) thickness under gold pads. Also, there is a trade-off between dry oxygen plasma being a dry process and the under-cut etches of chromium adhesion under layer.

3.2 New (4th) Generation Process Flow

The 4th and the last generation process flow benefits from a more straight forward point of view which gives the efficiency control to the production engineer. The flow makes benefit of the anodic bonding and the glass handle layer approach and also the parylene coating for the isolation and insulating the resonators from the flowing fluid. Additionally, the microchannel is carved inside the glass wafer and the resonator active sites are facing inside the glass wafer gaps. The new generation process flow can be examined in Figure 3.17.

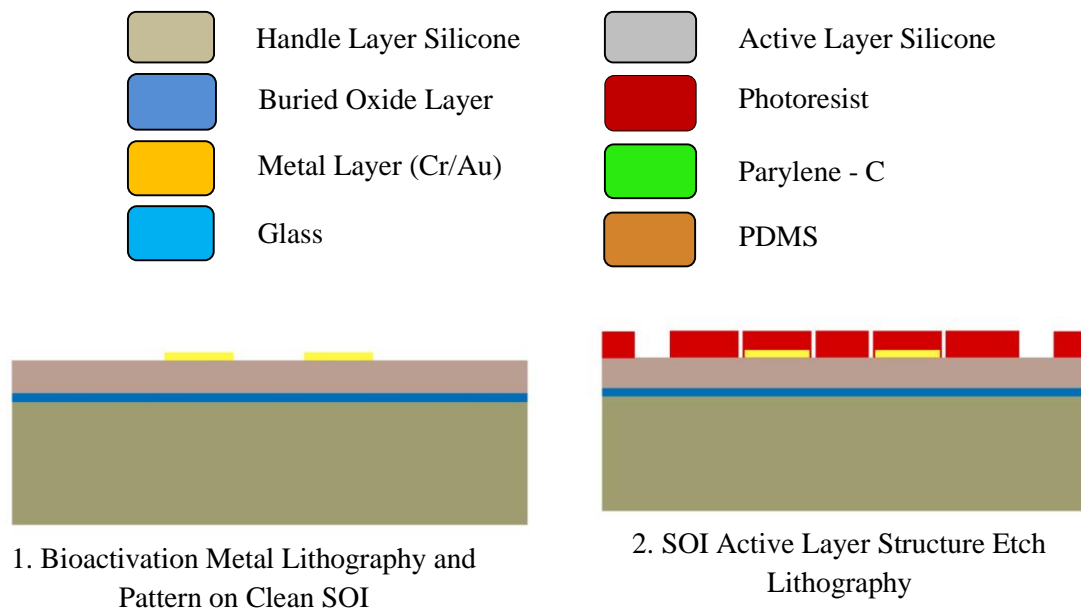
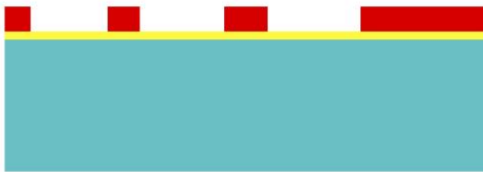


Figure 3.17: New Generation Process Flow.



3. SOI Active Layer Structure Etch by DRIE with Bioactivation Metals Appear on Proof Masses of the Resonators



4. Metal Mask Coat and Lithography for Recess Etch on Glass



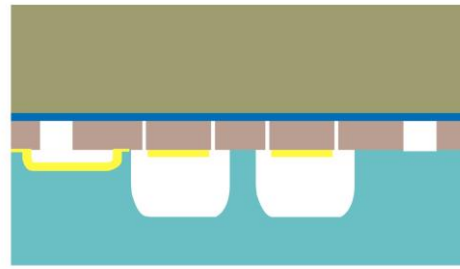
5. Recess Gap Etch on Glass with Metal Mask Under Pure HF



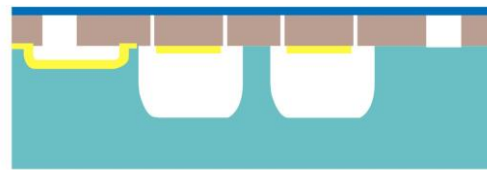
6. Microchannel Etch Inside the Glass with Metal Mask Under Pure HF



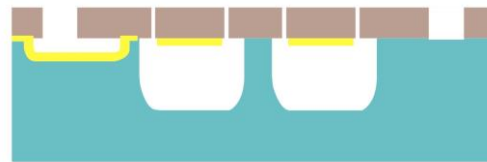
7. Routing Metal Coat and Pattern inside the Recess Gaps



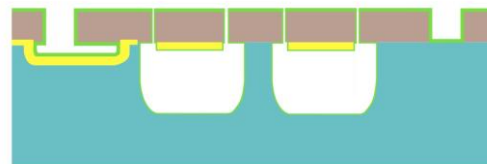
8. Anodic Bonding



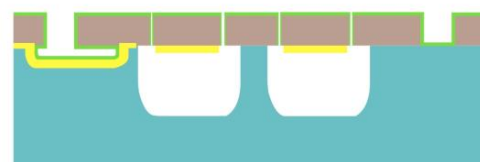
9. Silicon Backside Handle Removal with DRIE



10. Release the Resonators by BHF and Hot Methanol Dry



11. Parylene-C Coat and Pattern with Oxygen Plasma



12. Parylene-C Pattern with Oxygen Plasma



13. Wire Bond Pad and I/O Caps Open with DRIE and RIE (Optional if necessary)

Figure 3.17: New Generation Process Flow. (continued)

As a start, the SOI and the glass wafers are cleaned under DI water rinse and then in piranha cleaning for completely removing the dust and organic residues on the wafers possibly coming from the manufacture steps. Then, the SOI wafer is etched in BHF for a very short time for native oxide removal for increasing adhesion quality. Then, the SOI wafer is coated with Cr/Au metal layer by sputtering and photolithography for bioactivation sites metal patterning is done on the clean SOI active silicon with wet metal etching or exchanging the photolithography and Cr/Au coating steps and lift-off procedure (See Figure 3.18). Especially, after the metal etch patterning, an extra gold wet etch is done for a short time so the diffused gold residues which can penetrate through the chromium layer are etched away from the surface.

Continuing with the SOI wafer, active device layer DRIE lithography is developed on the bioactivation metal islands. The active device layer resonator structures are etched with a mask of differing thickness of lines around resonator sites. This issue causes the resonators to be weakened and thinned at the anchor parts, in DRIE etching of the active silicon layer. (See Figure 3.19) Thus, as mentioned in the previous sub chapter, the structure mask is prepared considering this fact and the optimization of the notching and under etch trade off can be disposed. Then, the DRIE etch rates are optimized with trial Silicon and SOI wafers. The critical dimensions are achieved with the DRIE etching method developed in METU-MEMS facility [76]. The resultant etch rates are at a minimum notching rate measured under SEM with not more than 5% loss of dimensions. Besides, the SEM inspection of the resonators are also done for a cross check for all the DRIE etches (See Figure 3.20).

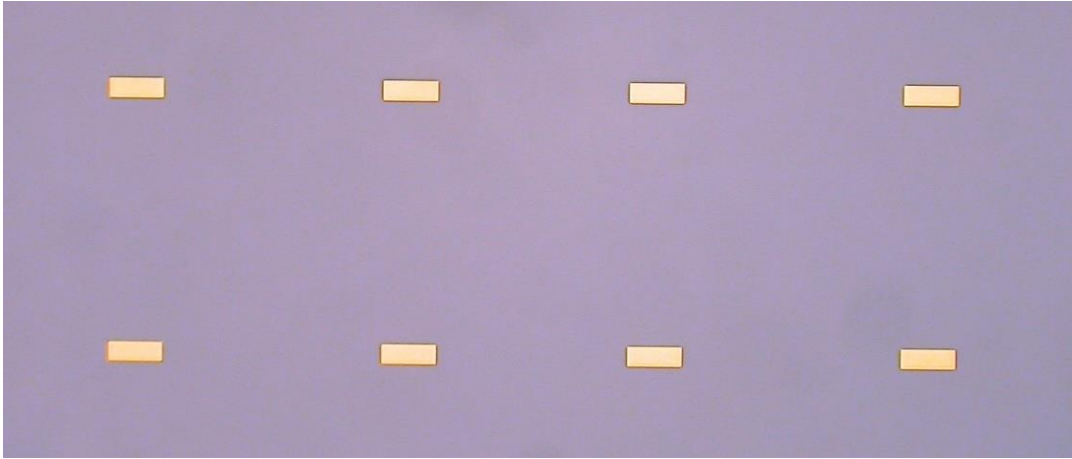


Figure 3.18: Bioactivation metal patterned on clean SOI active layer silicon side.

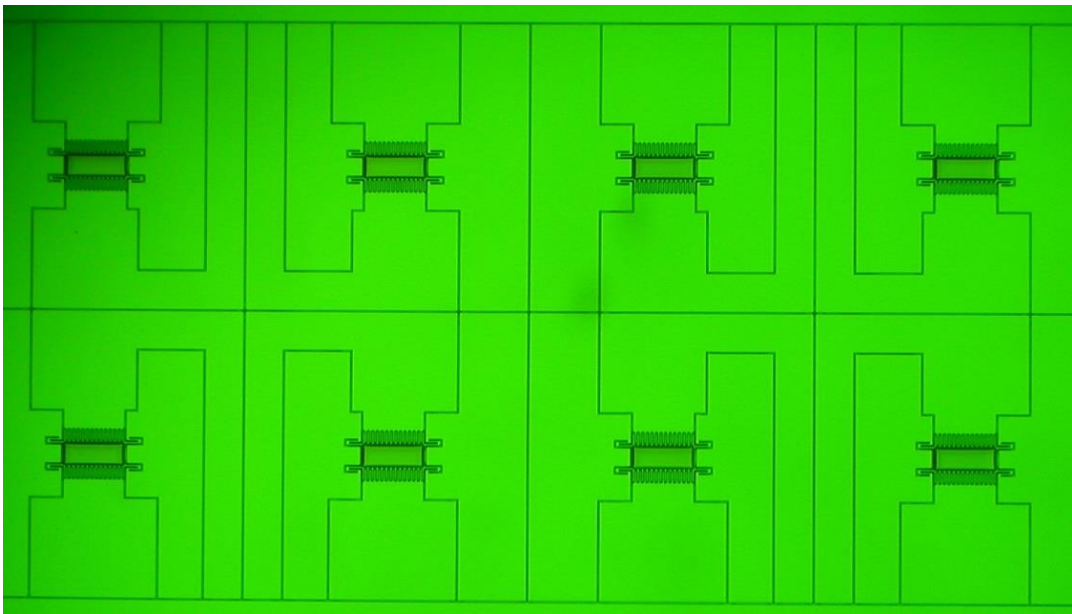


Figure 3.19: SOI active layer structure DRIE etch lithography.

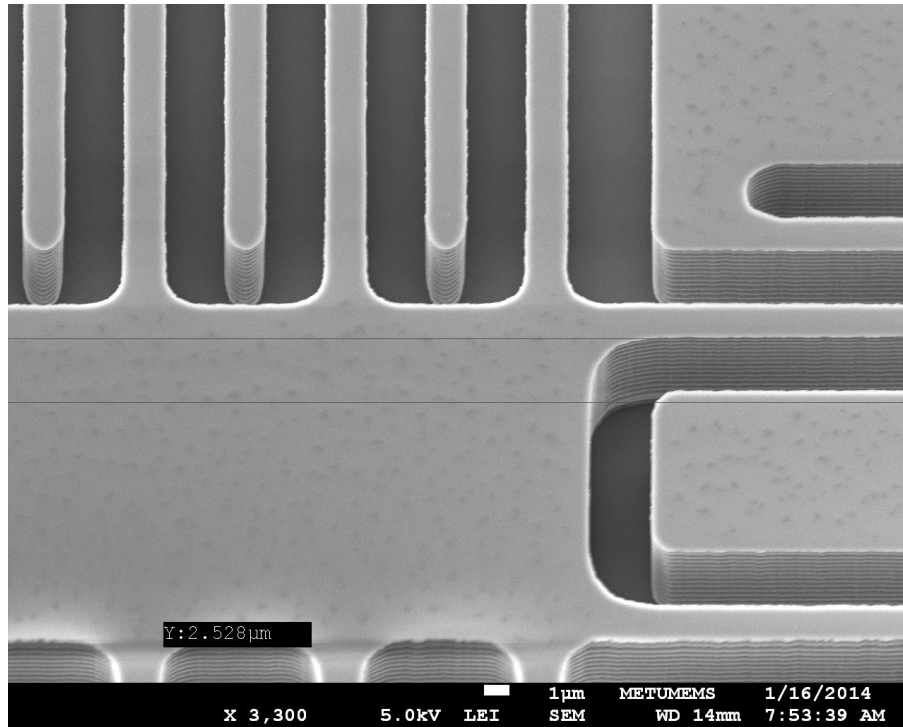


Figure 3.20: SEM inspection of SOI active layer structure DRIE etch on the test resonator.

Meanwhile, the glass wafer is etched in BHF for 1 minute for adhesion improvement for the metal masking layer. Then, after dehydration and Cr/Au coating under sputtering the recess etch metal masking layer is patterned with lithography of $3\ \mu\text{m}$ of SPR 220-3 photoresist. Afterwards, the photoresist is hard baked and remove the residual photoresist in the trenches with descum procedure with oxygen plasma under 1 Torr pressure, 150 W power for 3 minutes. After the metal etch procedure for patterning the metal masking layer, the opening glass sites are etched with pure HF for $5\ \mu\text{m}$ recesses to be created (See Figure 3.21). During the etch of the glass for uniformity, the etching medium is stirred continuously with a magnetic fish. At the end, the Cr/Au metal masking layer is stripped and the recess gaps are appeared for free movement of the resonating structures and preventing the shorting between active silicon layer and the metal routing lines (See Figure 3.22).

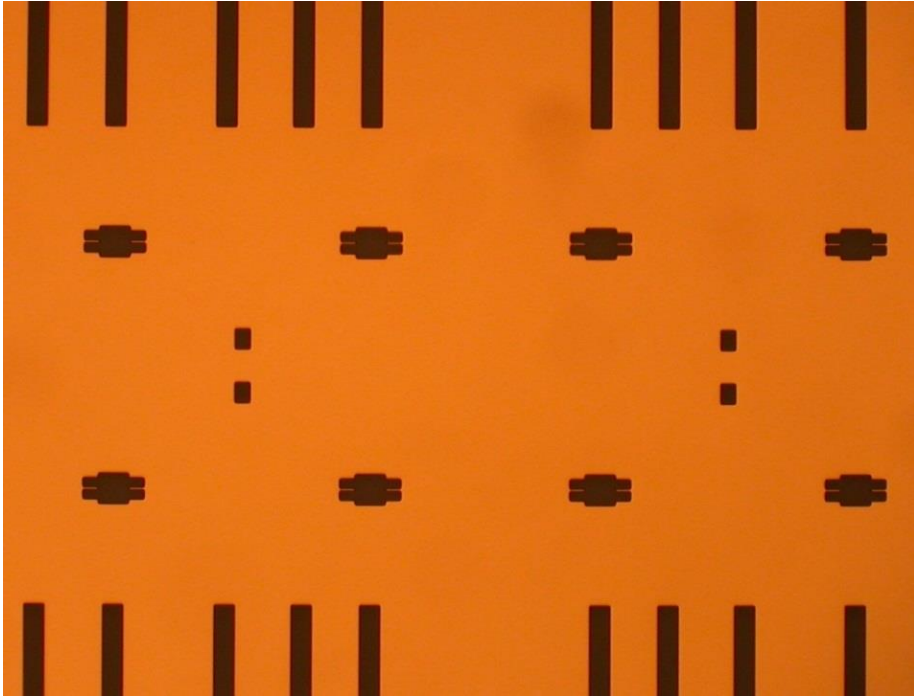


Figure 3.21: Recess etch Cr/Au metal masking layer with Au and Cr layers are etched. The resonator sites and the tips of the drive, sense and ground lines can be seen.

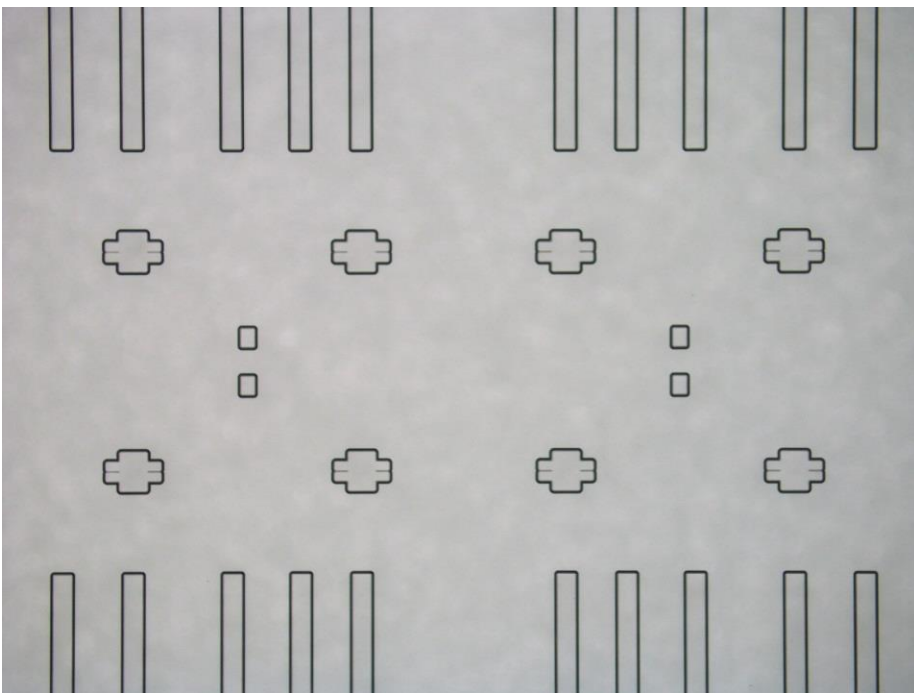


Figure 3.22: Recess etch on the glass wafer with metal masking for pure HF wet etch with 5 μm deepness after the Cr/Au metal masking layer is stripped.

In the past, the recess gaps are drawn without taking into account of wet pure HF etch lateral expansion so the recess gaps are shorting the metal lines with some extra lithography and etching contamination. The metal lines are crowded and differing greatly with the longitude. The new mask set is prepared for recess gaps are minimum 100 μm apart from other lines and so there is no possible of shorting. Also in the final design, the recess lines are comparable in longitude and they are drawn in a simpler manner. (See Figure 3.23)

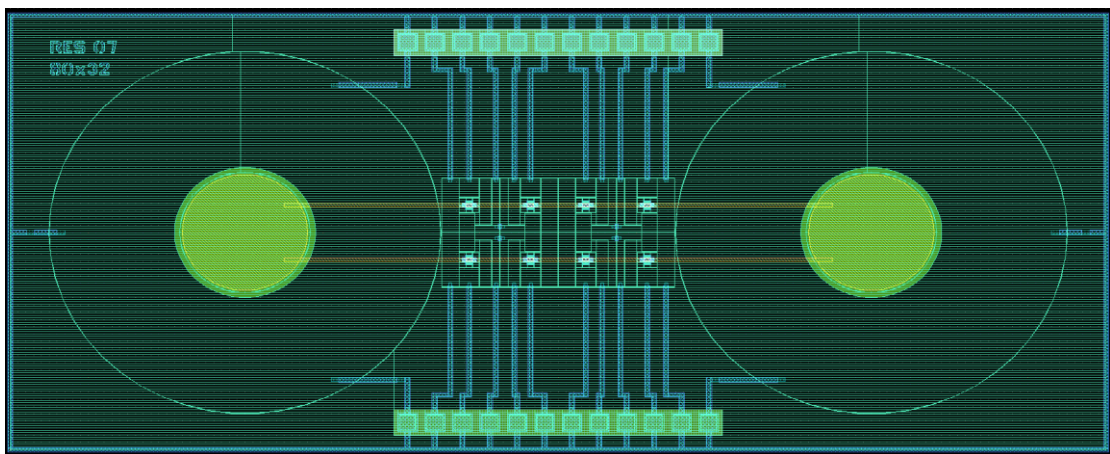


Figure 3.23: The general top view of the resonator mask steps for process flow 3rd generation. The blue lines show the recess gaps and the metal lines that will be carved inside the glass wafer.

Proceeding, the glass metal masking layer is stripped off then, a new Cr/Au layer is sputtered on the glass wafer for the aim of metal masking the microchannel pure HF etch. The mask for the recess and microchannel sites does not correspond so we do not need an extra thick photoresist for this step, we prefer to use spray coating of S1813 with 4.5-5.0 μm thickness for the lithography of the metal masking layer. The edges of the etch sites can not be covered with standard spin coating and this edges become exposed to the wet metal etchant and so on the wet HF etchant for microchannel which result in deep wells on the edges of the recess gaps. The spray coating covers the waviness of these recess etch sites conformably and prevent the

deep undesirable etch sites. After the metal etch, the microchannel is carved inside the glass wafer with not more than 50 μm deepness on the original channel line and not more than 60 μm lateral undercut widening and the total microchannel wideness to be 170 μm (See Figure 3.24).

Afterwards, the metal mask layer is etched away again and the Cr/Au coating and patterning is repeated for routing metal and wire bond pads to be fabricated (See Figure 3.25). As in the previous step the lithography is done with spray coating due to 50 μm deep topographic transitions on the wafer. In all these wet metal etch steps the diffused gold penetrating through the chromium are etched with an extra gold etch step is added at the end of the Cr/Au wet etches.

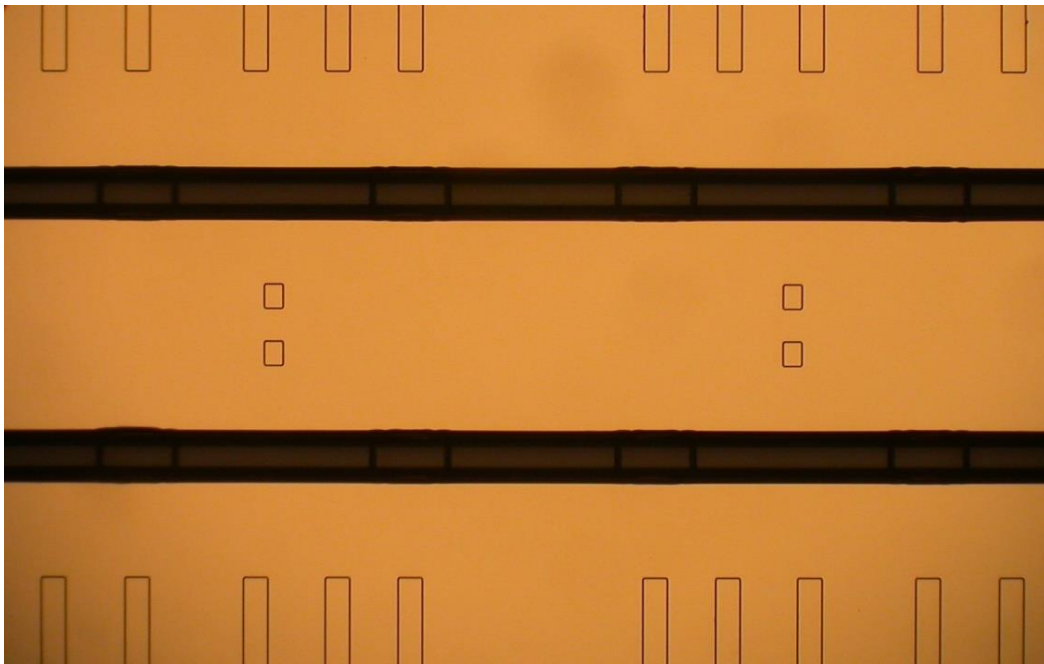


Figure 3.24: Microchannel carved inside on the recess patterned glass wafer with 50 μm deep and not more than 170 μm wide.

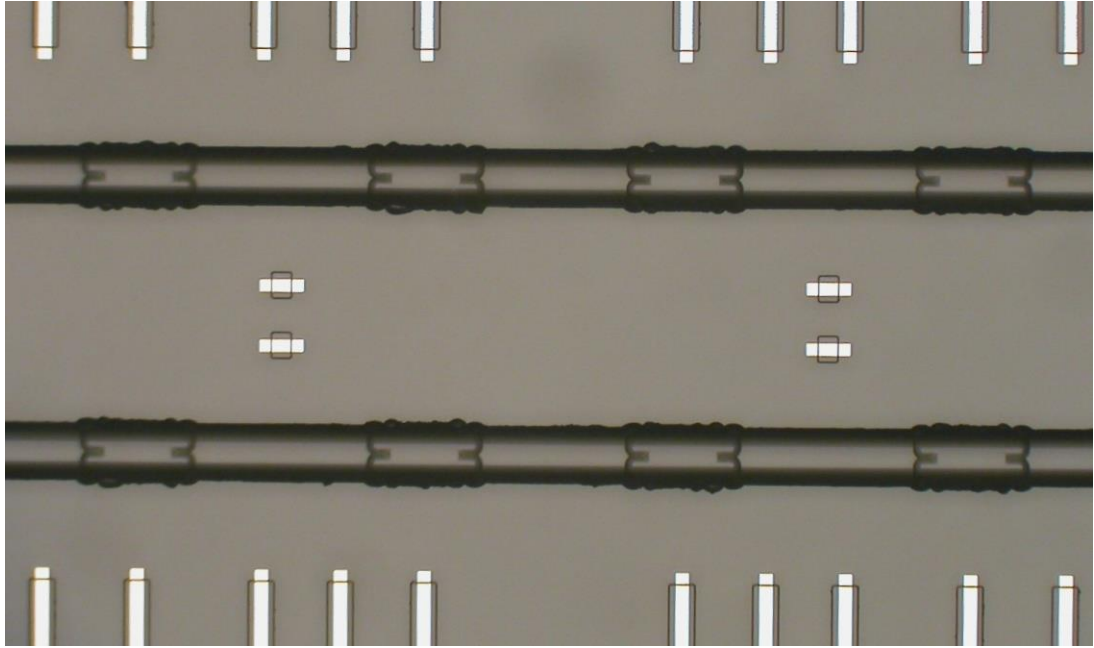


Figure 3.25: Microchannel carved inside on the recess patterned glass wafer with routing metal lines and wire bond pads are patterned.

Then, SOI active layer silicon and the active side of the glass wafers are required to be cleaned for high quality of anodic bonding. The SOI and glass wafer are cleaned in a 1:1 piranha ($\text{H}_2\text{SO}_4:\text{H}_2\text{O}_2$) solution for 20 and 10 minutes respectively. The wafer of SOI with bioactivation gold patterned on the resonator structures can not stand after the gold treatment of piranha due to under etch of chromium layer underneath gold sites. Afterwards, the SOI wafer and the glass wafers are treated for shallow etch under 1:7 BHF for removal of the native oxide layer grows on the both wafers in normal conditions. The shallow etch is done for not more than 1 minute for both SOI and glass wafers, and is aimed for achieving better contact quality in between routing metal lines and the SOI active device layer [75]. Also, the etch for the glass wafer is done as a final cleaning of the gold residues remaining from the metal etch procedure for routing metal patterning. Also, for glass wafer short BHF etch is used for final assuring of the removal of the diffused gold residues.

As the intermediate step, the structure patterned SOI wafer with bioactivation metal patterned on top of proof masses and the recess and microchannel gap patterned glass wafer are aligned to each other. Then, wafers are bonded with anodic bonding of

glass to silicon. EVG 501 wafer bonder system is used in this process and a bias voltage of 1200V, piston force of 1500 N, and bonding temperature of 370°C is applied on the wafers.

The anodic bonding cause high rate of burning and sparking between fingers of the resonators and metal lines, resulting in huge amount of loss of the contacts and resonators. This can be solved by leveling the voltage applied which can be done by shorting all lines for whole wafer which is done in the last mask set. All lines that are connected and they are prepared as to be separated with the dicing lines (See Figure 3.12). If we remember the previous preparation section of the final process flow, the second issue about the anodic bonding is the pad line hindering of the metal layer on the drive and sense electrode anodic bonding area, we have shorten the lines, so the area of bonding can be increased. The final anodic bond is achieved to be strong and can be observed in Figure 3.26.

The third issue is the graphite residues remaining after anodic bonding; an additional step of piranha cleaning can be done afterwards but this does not clean all the graphite residues and piranha cause residues at this stage so we do not prefer to use it. Moreover, piranha cleaning before the bonding is crucial and it is necessary to make sure of there are no residues remaining before anodic bonding. Otherwise, this residues cause local breakages on the wafer. Also, the anodic bonding quality has been increased by increasing the bond area achievable with updating the mask. On the other hand, the bond strength is also increased with increasing bonding temperature at the state of the anodic bonding to 370°C and better results are observed.

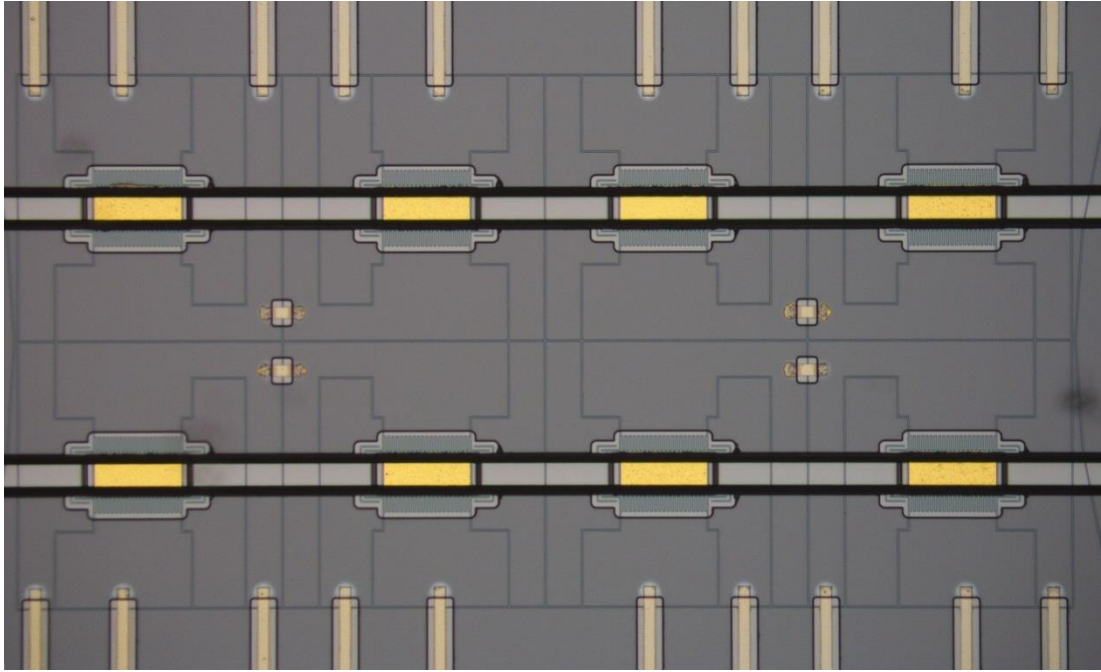


Figure 3.26: Resonator sites can be seen after anodic bonding. The microchannel is carved inside the glass wafer and the bioactivation gold layers are appearing on the resonators. Sparking is not occurring between fingers of the resonators and it does not burn off the contact lines.

Then, the 350 μm thick backside handle layer is etched away with DRIE and then, the buried oxide layer is etched with RIE or BHF (1:5) for releasing the resonator sensors. The RIE dry etch will be more confine for this step but there is a remaining residue of burned photoresist which could not be removed on the outer ring of the wafers. After wet BHF release is done, the wafer is cleaned in water for a long time for the remaining BHF is dissolved away from the microfluidic channels. Lastly, the drying process is done in acetone, isopropyl alcohol (IPA), and methanol respectively and finally dry at 70 $^{\circ}\text{C}$ with methanol is vaporized on the surface. (See Figure 3.27)

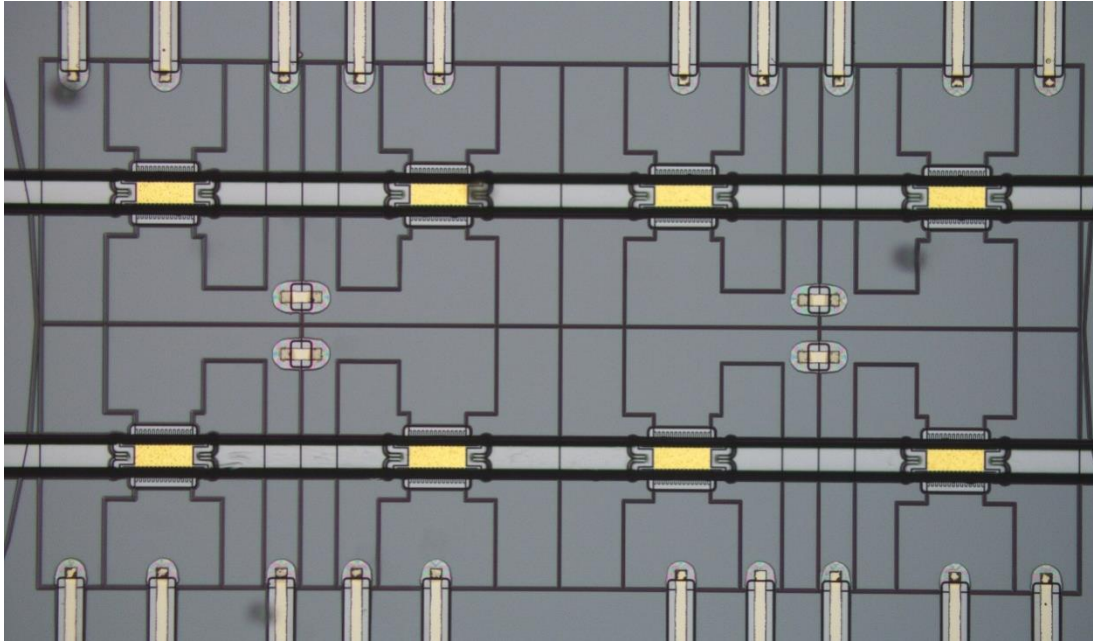


Figure 3.27: After the DRIE backside handle layer removal and BHF release are done. The BHF over etch can be observed around pad contact areas.

As the final step, after the device is released, a thin parylene layer is coated in parylene deposition system. The resonators are coated with Parylene-C for a thin layer around $0.5 \mu\text{m}$ with I/O holes are blocked by MicroSoup-95 solution which is anti-adhesion agent for the parylene polymer and even after the solution is degassed under vacuum of the parylene coating system, the parylene penetration is prevented considerably. At the last step, the wafer is etched under no masking layer inside the oxygen plasma for an optimized short period. Normally, this measure of thickness of parylene-C etches in 30 minutes but the gold facing inside the microchannel etches away in not more than 5 minutes. Higher time periods cause also loss of the in between finger and anchor parylene coating layer. In fact, the SEM analysis shown in the next sub chapter, indicate that the remaining parylene is around $0.4 \mu\text{m} \pm 0.05 \mu\text{m}$ thickness of Parylene-C is remaining on the finger and anchor side walls. Thus, the hydrophobic characteristic of the parylene coating will remain for in fluid processes adequately.

There is only a final optional step of contact pad and input-output opening after the parylene is deposited, is remaining. The wet processes after the release are decreased

considerably, the I/O and pad opening step is also optional. I have prepared the SOI patterns with mechanically breakable structures; this will cause the silicon active layer to be peeled off after the BHF oxide release of the devices. The I/O pads are peeling off really easily but the pad openings are not removed relatively. I have another precaution for that issue, and all the pads have a 30 μm radii opening on the corner for removing with probe tips which is working for the chips.

3.3 General Remarks on the New (4th) Generation Process Flow

For this process flow, the main advantage will be working on SOI and Glass wafers independently and the anodic bonding, the handle layer removal, and the BHF release steps will be done at the very last steps. It is possible to work only on these suspended devices for I/O openings of the microfluidic channels. This result in much more fine fixtures to be processed and also alignments can be done with around 1 μm sensitivity.

The SOI DRIE patterning could be done in the first step. Unfortunately, the photolithography is more challenging because of the topography form the patterning of DRIE is greater. Also, the penetration of the commercial metal etchants present a difficulty inside 2-4 μm wide and 5 μm deep etch sites; there is remaining metal non-etched residue in between the fingers and anchors as seen in the SEM inspection of these wafers. (See Figure 3.28) This problem is solved by switching the bioactivation patterning step with the DRIE structure patterning step in the order of process flow. The trials are done for both lift-off and metal etch procedures and the results are fruitful for both the fabrication steps. The bioactivation lines can be fabricated by both of the processes.

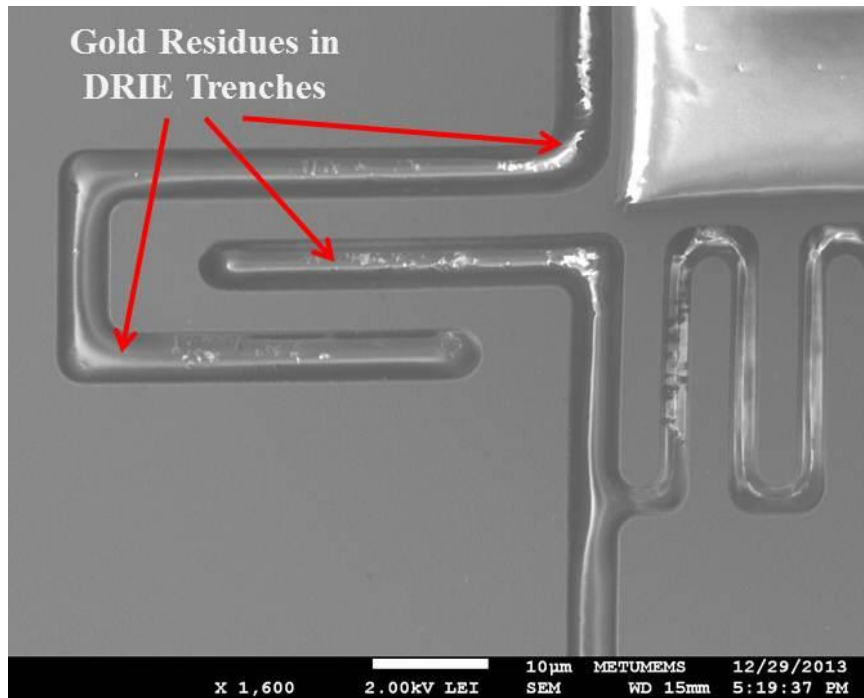


Figure 3.28: Gold residues between the fingers and DRIE etch sites due to penetration challenge of the metal wet etchants in between deep DRIE trenches.

The lift-off process is used for cross checking the proof mass resistive coupling problem for the shorting observed after metal etch gold residues and the diffused gold sites. The lift-off procedure hinders this problem with protective 3 µm SPR 220-3 photoresist layer which does not let gold diffuse into the silicon. Also, for the metal etch patterning, an extra extended time for diffused gold etch is used with considering the effect of deep undercut created under bioactivation gold sites. This cause an extra 1-2 µm over-etch which will decrease the area of bioactivation field for the small fields 3-4 µm from all sides. Besides, the minimum bioactivation gold sites on proof mass fields (40 µm x 10 µm) can be protected with both methods (See Figure 3.29).

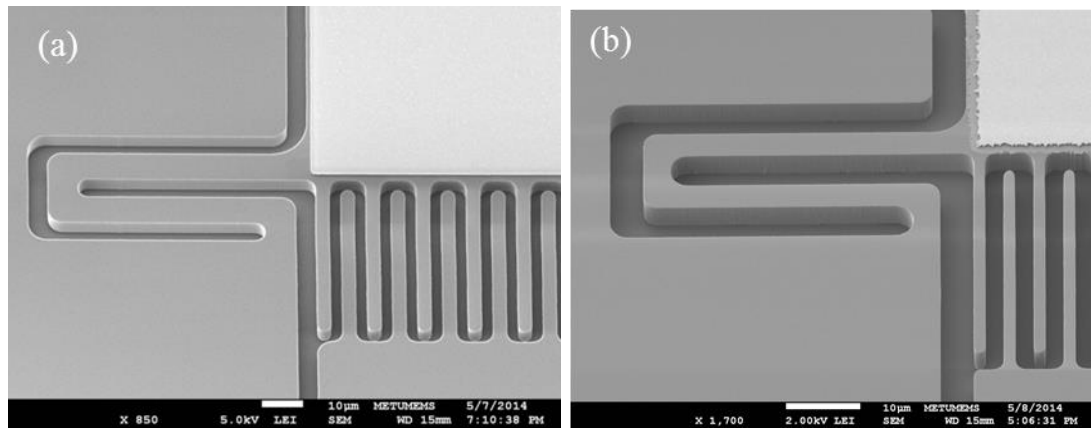


Figure 3.29: The bioactivation structures compared under SEM, (a) the twisted edges can be easily observed with lift-off patterning; and on the other hand, (b) the metal etch over etch of the gold sites with increased diffused gold etch times. Cr under the gold bioactive sites can be observed.

The other issue with the method is the spin coating dispersing. The cavities deeper than about 10 µm, result in thinning of the resist at convex corners and accumulation inside the cavity create problems with exposure and with leaving insufficient resist thickness on the sidewalls during etches. Even thick photoresist usage could not solve the issue. The deep trenches are occurred after the recess etch under HF wet etch, and then microchannel etch with deeper HF wet etch the trenches become more obscene. These dispersing of the photoresist cause some discontinuities at the contact lines of metal routing as seen in Figure 3.30. This problem is solved with the spray coating usage.

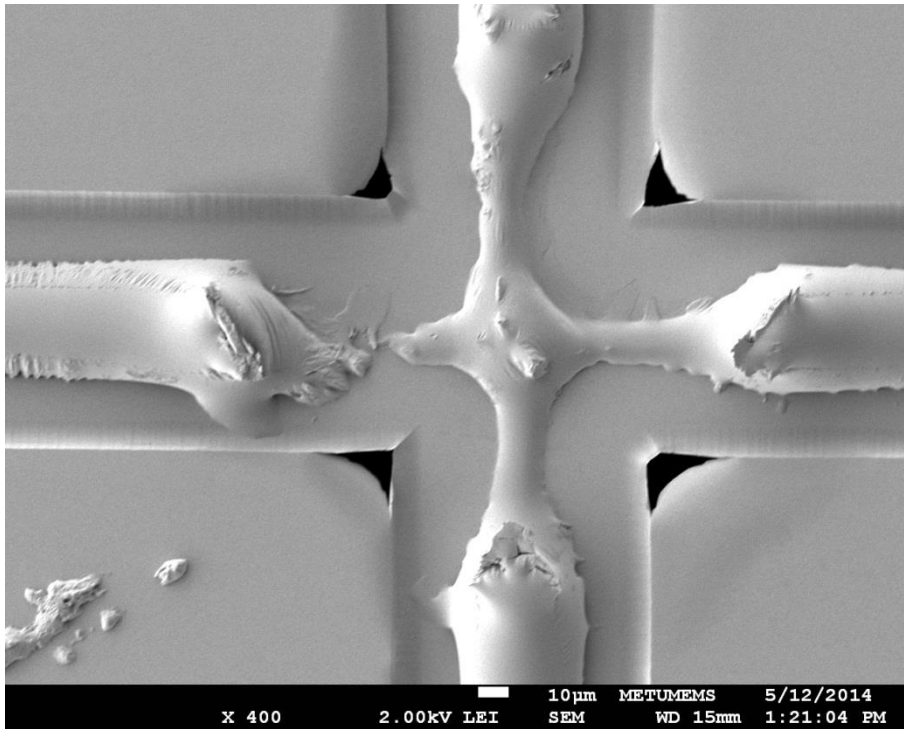


Figure 3.30: The spin coating of photoresist with cavities on the field create some trenches under HF wet etch and then at the next spin coating steps, the metal routing lines become trimmed and even become discontinuous.

3.4 Fabrication Summary

As a summary, the chapter explains the previous generation fabrication flows for the resonator gravimetric rare cell detection devices. Furthermore, the problems of these fabrication flows are inspected and the solutions are explained in detail. Then, the issues required to be solved for the increase of the throughput of the fabrication is expressed. Under the light of these experiences, a new fabrication flow is presented. As a result, a resonator with a gold layer proper for bioactivation on the proof mass area is achieved with high throughput rate after the fabrication steps. The processing on the active side of the wafers give the advantage of better alignment rate with 1 μm precision and low loss of features due to over etching through the new generation fabrication flow process steps. The SEM image of the device and optical photograph with microchannels are given in Figure 3.31 and Figure 3.32 respectively.

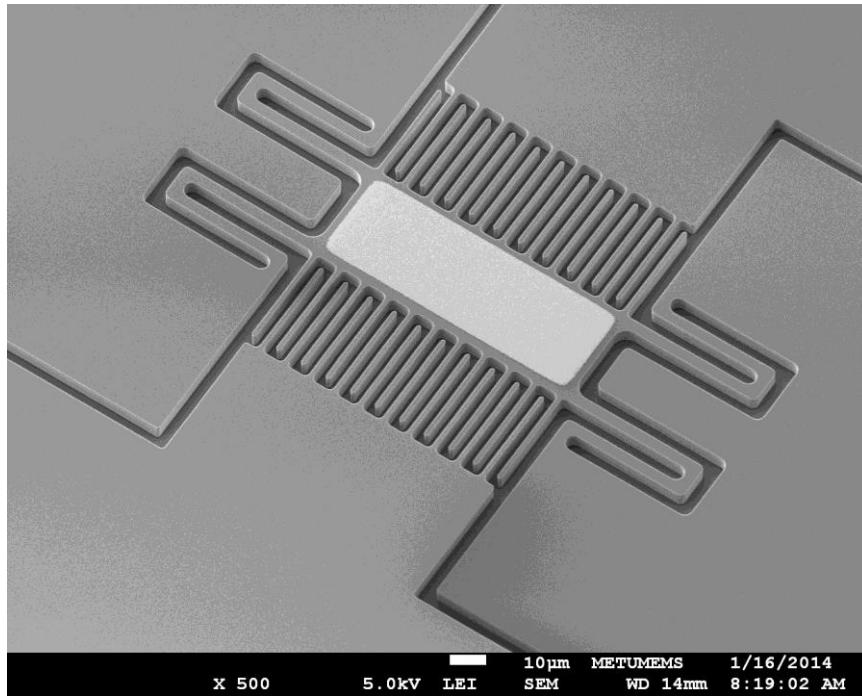


Figure 3.31: SEM image of resonant mass sensor device with bioactivation gold is standing on the proof mass of 4th generation process flow.

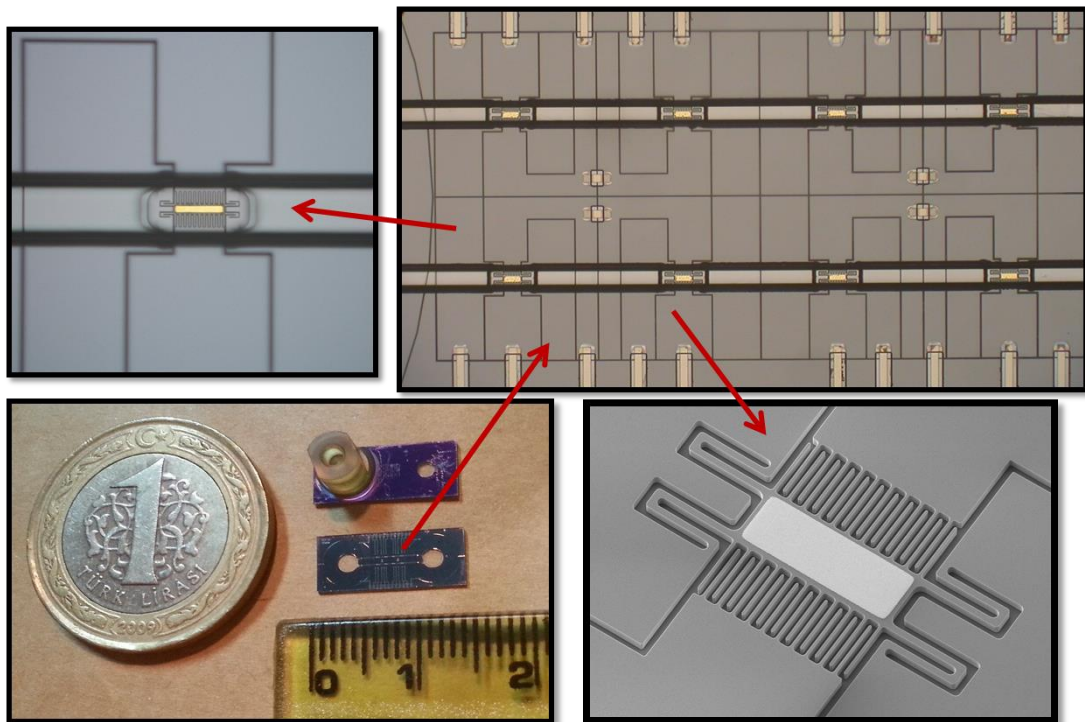


Figure 3.32: The photograph of resonant mass sensor device integrated with microfluidic channel cap and electrical connections in the 4th generation process flow. One of the input and output ports are mounted on the holes of the glass microchannel with white epoxy.

CHAPTER 4

EXPERIMENTAL RESULTS

This chapter starts with the check-out tests for the novel method for Parylene-C coating and patterning on the inner bioactivation gold sites with validation analysis under SEM and EDS. Then, the chapter continues with the experimental results of the cell detection resonators with the resonance spectrum and open loop analysis of the resonance behaviors. The resonators are examined for device operation status with and without parylene coating. Then, the analysis of the devices is done for in fluid operations. This step is divided to fluidic leakage tests of parylene hydrophobicity and electronic tests of the resonator devices under fluid flow. The interface circuit for amplifying the signal is also given.

4.1 Parylene Cleaning Except on the Inner Bioactivation Gold Sites

The main aim for this novel process is the parylene cleaning on top of the bioactivation layer. Also, the parylene deposition uniformity is problematic. Therefore, close inspection under SEM (Scanning Electron Microscopy) and EDS (Energy Dispersive X-Ray Spectroscopy) analysis are done for clarifying this uncertainty.

The uniformity tests are done in a detailed manner for PDS 2010 Parylene Deposition System. The results show not more than %10 deviations around the aimed value of the parylene coating. The major issue for the new process flow of the

resonator cell detection devices is the penetration of the parylene-C through 2-3 μm gaps between fingers and the anchor sites.

The parylene layer is desired to be as thin as possible as explained in the design chapter. Various coating trials and optimization of the thin coating process have been made. Dimer amount and wafer position inside the coater is varied in these trials. As a result, uniform coating for thickness values as low as 0.3 μm has been successfully performed. On the other hand, the thickness of the parylene layer after this novel method is thinned with oxygen plasma and due to avoiding possible uniformity problems; we used a thicker coating of 0.5 μm for the starting thickness of coating.

The deposited parylene-C surface is hydrophobic, with a contact angle around 100-110°. However, fluorine based plasma treatment with SF_6 or CF_4 can be used to change the surface to be super hydrophobic up to contact angles of 130-155° as mentioned in the study of Chen *et al.* [77].

The Cell Detection Resonator devices with parylene coating and removal from the bioactivation sites are tested and optimized. The distribution of the parylene coating is inspected and the EDS analysis are done for varying points of care from backside and top side of the resonators. The resonators with bioactivation gold sites are fabricated on the inner side of the proof mass and the walls of the fingers of the resonators are aimed to be coated with parylene-C. The parylene-C coating will hinder the penetration of the fluid which is flowed on the resonators through microchannel structures. Meanwhile, the inner bioactivation sites are cleared from parylene-C coating.

The trials are done with 0.5 μm parylene-C coating. The input and output openings are opened after BHF release. This high rate of penetration of parylene can be problematic. The procedure is developed taking into account that the penetration of a polymer vapor is lower than the penetration of the oxygen plasma. This effect is tested and approved. Besides, the process idea is not only depending on this fact; it is also supported by another practical way of blockage; from I/O holes by MicroSoup-95 (1:50 in DI) solution droplets which is the anti-adhesion agent for the parylene polymer and even after the solution is degassed under vacuum of the parylene

coating system, the parylene penetration is prevented considerably. Then, through the vacuum process it degasses and so I/O holes are opened for the oxygen plasma treatment process. Only coating will be occurred with penetrating parylene through resonator fingers and anchor sites. Thus, the coating on the inner bioactivation gold will be thinner than the outer proclaimed resonator top side and in between fingers. This thin parylene coating will prevent the flowing fluid in between resonator fingers or the separation parts of the resonators [69].

The thickness of the main parylene-C coating is as expected 0.5 μm on the top side but it will decrease when the parylene penetrate in to the fingers and coat the inner backside of the proof mass and also the glass microchannel inner walls. This decrease, through 5 μm active silicon layer which is the thickness of the active silicon of the SOI wafers we use. We observe the thickness of the SOI resonator structures with SEM before. This penetration is observed and measured to be around 0.05-0.08 μm for the inner sides after the coating of 0.5 μm is coated from the top side. The thickness of the coating of parylene becomes to be around 0.1-0.3 μm for the in between fingers. In fact, our novel method makes use of this distribution on the critical sides of parylene-C coating. The oxygen plasma treatment can be used for the cleaning of this parylene layer [78]. The Figure 4.1 shows that the resonators can be observed after tape-check for observing the inner parylene coating thickness. Parylene is coated and after oxygen plasma treatment the resonator finger side walls parylene coating still remains in an aspect. The blur effect is caused by the parylene layer coated on the sidewalls of the resonator fingers. If the treatment increased the parylene layer becomes so thin that the SEM blur created cause of the insulation of parylene disappears.

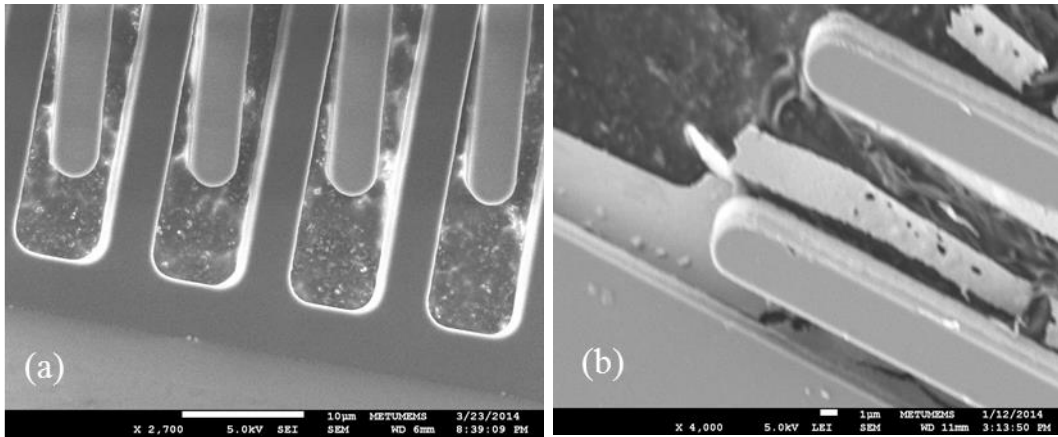


Figure 4.1: The view of the resonators can be observed after tape-check for observing the inner parylene coating thickness. (a) Parylene is coated and after oxygen plasma treatment the resonator finger side walls parylene coating still remains in an aspect. (b) If the treatment increased the parylene layer becomes so thin that the SEM blur created cause of the insulation of parylene disappears.

The aim of the trials are done for clearing the field of bioactive gold site on the inside of the channel so even a small portion of parylene residue will prevent the bioactivation field from the chemical functioning process.

Thus, EDS analysis is used for controlling the results of the oxygen plasma treatment. The inspections are done in four differing plasma treatment states and one without parylene coating state as the control group. The EDS analysis is done for Carbon (C) and Chlorine (Cl) atoms of the parylene-C molecule, the remaining Hydrogen atoms can not be observed under EDS analysis (See Figure 4.2). The field of interest with certain EDS analysis are done shown on the SEM image of the resonator after tape-check; inside the blue box is called “Middle” measurements, in between blue and red boxes is called “Edge” measurements and in between green and red boxes is called “Outer” measurements. The measurements are done in these fields with the average of 5 different point measurements and for 6 different dies of sampling.

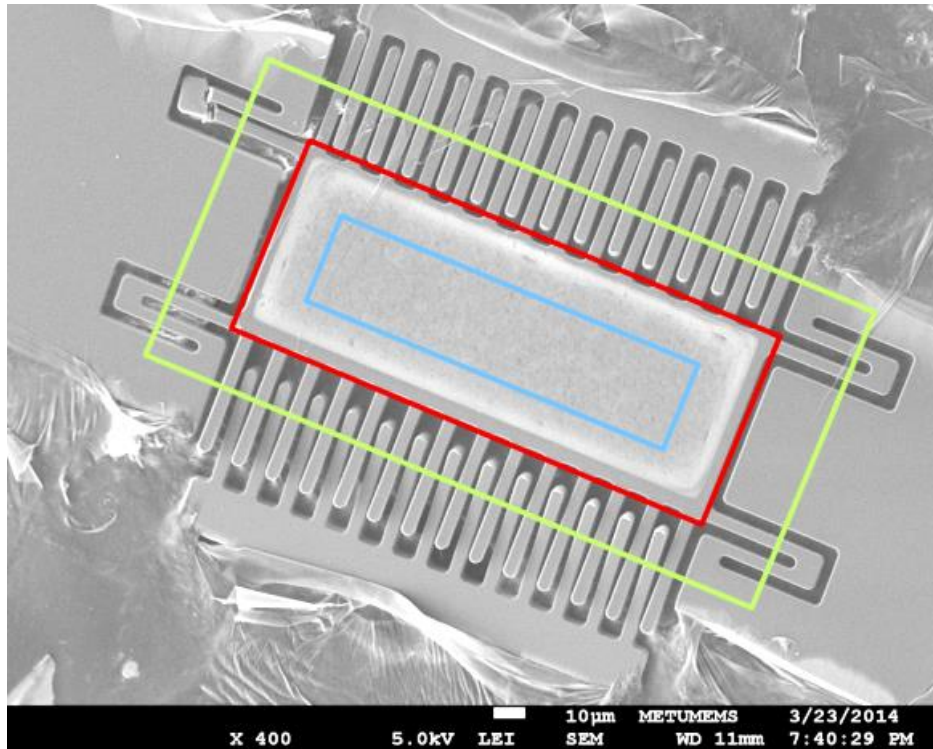


Figure 4.2: The field of interest with certain EDS analysis are done shown on the SEM image of the resonator after tape-check; inside the blue box is called “Middle” measurements, in between blue and red boxes is called “Edge” measurements and in between green and red boxes is called “Outer” measurements.

The EDS inspections are done for 4 different stages of oxygen plasma treatment after parylene-C coating. The oxygen plasma treatment is done under 1 Torr vacuum conditions and under 300 W power is applied. The first stage is no oxygen plasma treatment after Parylene-C, the second state is 2 minute of oxygen plasma treatment which is not enough and for observing the middle state. The third state is the optimized parylene cleaning, 5 minutes for 0.5 µm parylene-C coating which clears the inner parylene layer on the bioactivation gold site. The fourth state is 30 minutes of oxygen plasma etch which is the required period for all the parylene inside and outside the microchannel cleared.

During the measurements, the top sides of the resonators are also inspected and the results show the parylene is still remaining on the top side of the resonators. (See Figure 5) Also the thickness of the parylene on the top side of the resonators and the

thickness coated between fingers are critical for the applications. The coating aimed for 0.4 μm for the Figure 6 and the thickness between fingers are measured to be around 0.45 μm after coating. And after 5 minutes of oxygen plasma treatment which is enough for removing the inner parylene coating.

Table 4.1: Average values for the percentage of the EDS analysis for 3 different location intervals. The values are average of 5 measurements each for 6 dies (30 measurements)

| Location (Average of 5 point measurement) | Oxygen Plasma Treatment Time (minutes) | Si (%) | Au (%) | C (%) | Cl (%) |
|--|---|---------------|-------------------|------------------|-------------------|
| Middle Field | No Parylene | 5 | 95 | 0 | 0 |
| | No Plasma | 3 | 52 | 36 | 9 |
| | 2 min | 6 | 65 | 24 | 5 |
| | 5 min | 4 | 96 | 0 | 0 |
| | 30 min | 5 | 95 | 0 | 0 |
| Edge Field | No Parylene | 99 | 0 | 0 | 0 |
| | No Plasma | 22 | 45 | 27 | 6 |
| | 2 min | 34 | 51 | 12 | 3 |
| | 5 min | 35 | 58 | 6 | 1 |
| | 30 min | 99 | 0 | 0 | 0 |
| Outer Field | No Parylene | 99 | 0 | 0 | 0 |
| | No Plasma | 83 | 0 | 10 | 7 |
| | 2 min | 89 | 0 | 8 | 5 |
| | 5 min | 93 | 0 | 5 | 2 |
| | 30 min | 99 | 0 | 0 | 0 |

The results on the general average shown in the Table 4.1 and the general trend can be observed as the 5 minutes of parylene etch is enough for clearing the backside gold bioactivation layer on the proof mass. The middle of the proof mass gold is all cleaned after the 5 minutes oxygen plasma treatment. This is the case for all the top parylene is still remaining on the finger sites; the parylene is seemingly increased through the edges and outer regions. The finger sites are cleared in some aspect but the parylene is not completely removed.

The inspections under EDS are also checked under SEM imaging but the blurring effect caused of the astigmatism problem due to non-conductive characteristics of Parylene-C, prevent the inspection sharpness. The thickness of the parylene on the fingers is hard to observe, so the measurements for the thickness are not reliable but it gives information about the average thickness distribution. The measurement of thickness of the parylene layer on the resonators from the top view before the oxygen plasma treatment; the coating thickness is around 0.45 μm , after the oxygen plasma treatment (See Figure 4.3a) the view of the resonator coating thickness can be observed to drop to 0.31 μm . (See Figure 4.3b)

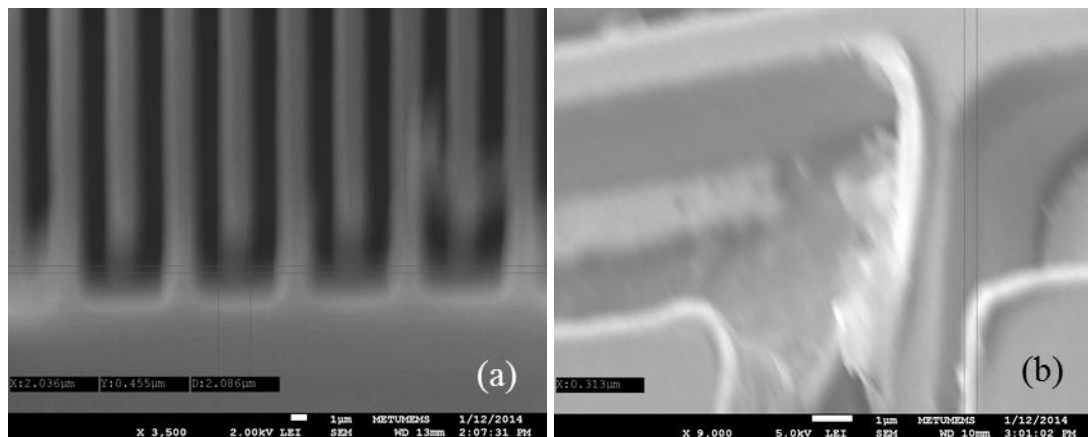


Figure 4.3: The measurements for the thickness are not reliable but it gives information about the average thickness distribution. (a) The measurement of thickness of the parylene layer on the resonators from the top view before the oxygen plasma treatment is around 0.45 μm , after the oxygen plasma treatment (b) resonator coating thickness is dropped to 0.31 μm .

Thus, for completing the proof, the EDS and SEM observations show the polymer remaining on the biocompatible microchannel, the final stage of the proof is the tests of fluid flow. The system is also tested under pressurized fluid flow and we did not observe any leakage. As a result, this novel method can be used for parylene coating for creating a hydrophobic surface and this will hinder the penetration of the fluids between the fingers. The optical view of the resonator are shown in Figure 4.4, after the parylene coating and then removal of parylene on the bioactive sites with short oxygen plasma treatment.

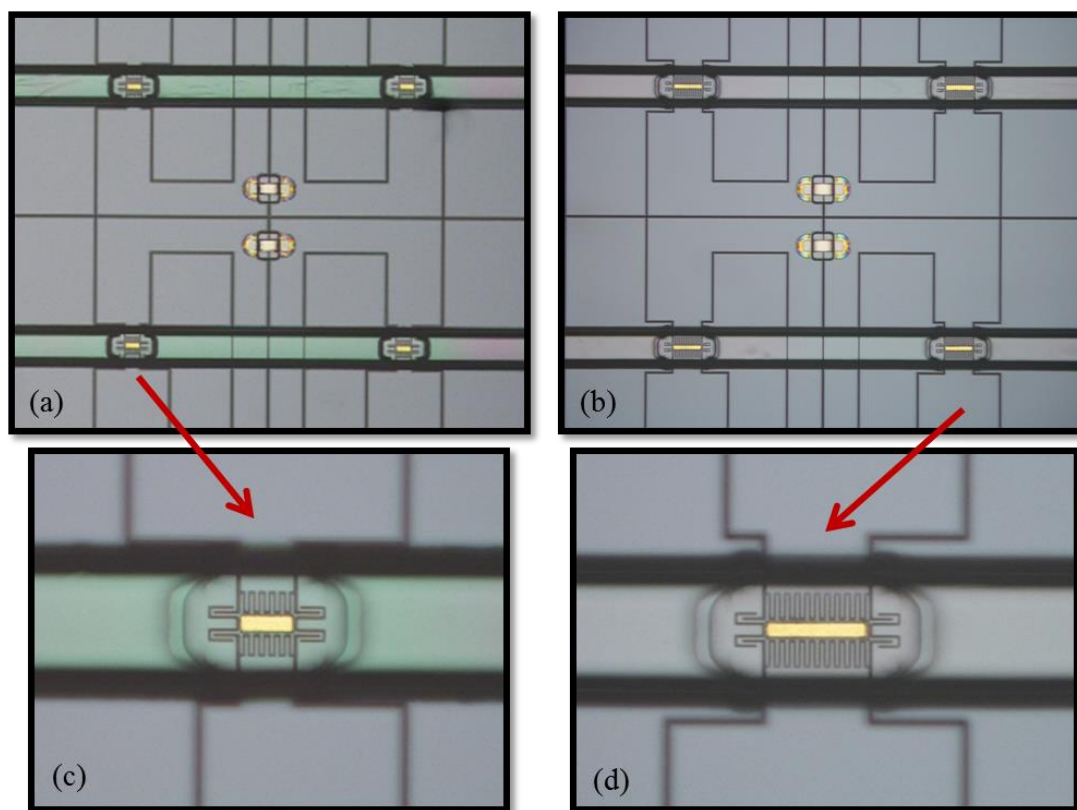


Figure 4.4: The resonator devices are shown under optical microscope, (a) after parylene coating, (b) after parylene is etched with short oxygen plasma treatment. (c) and (d) are the focused images for parylene coated and plasma treated devices respectively.

4.2 Interface Circuit

As mentioned in Chapter 2, the general current output of the cell detection resonator devices are too low. For conducting the tests, we need to implement the open loop operation of the resonators with a certain level amplification for resonance spectrum tests. The system is designed by Ekrem Bayraktar and Deniz Eroğlu for the previous generation applications [71, 72].

As mentioned in the previous chapters, the sensitivity requirements are force the designs of the resonator mass to be as small as possible which result in high natural frequency and low gain signal output. In order to accomplish to see the resonance characteristics of the devices, we need to amplify the injected nano ampere level current form the resonators.

Indeed, at this stage current is required to be converted to voltage which can be done with a transimpedance amplifier (TIA). The natural frequencies of the resonator devices that we fabricate are in the range of 200 kHz to 1.5 MHz, and TIA circuit can be optimized for the need of high frequency operation as in the resonator designs. For improving the signal to noise performance, the current noise of the OPAMP requires to be minimized and magnitude of the TIA feedback resistor needs to be maximized. Accordingly, the commercial OPAMP, OPA 656 from Texas Instruments, is chosen with the specifications of low current noise and wide bandwidth operation spectrum. Besides, the feedback resistance for the TIA package is chosen to be 1 M Ω which is highest possible resistor value for the intended operational bandwidth. The parasitic capacitance and the feedback resistor with 1 M Ω resistance is connected in parallel of the TIA circuit, has a much smaller impedance compared to the resonator input capacitance so higher bandwidth operation can be achieved with TIA circuit systems.

Closed loop operation is also possible with this configuration. If we connect a differentiator which adjusts the phase difference caused by the transimpedance amplifier; and gain stages for raising the signal and a comparator stage at the end as a

loop will operate in close loop. The study on this issue is not concluded yet, it is remained for the future work.

Our main goal in this thesis is to test the newly fabricated resonators if they are in operating condition or not. Thus, the open loop measurements of resonance spectrums are applicable for our situation. Therefore, the measurements are done only the TIA circuit with a capacitance is added in order to eliminate the stray.

The test setup for the resonance spectrum tests is shown in Figure 4.5. Each resonator has three pads of access; drive, sense and proof mass. A network analyzer, Agilent 5495A, gives an excitation AC signal of 15 dBm to the drive pad of the resonator. The proof mass of the resonator is biased with DC input at the level of 100V. Then, the emerging output signal of the sense pad is amplified with the TIA circuit. The TIA system is also kept operational with a DC supply of $\pm 5V$. The converted voltage output of the TIA interface circuit is then fed to the network analyzer.

The network analyzer sweeps the frequency and records the magnitude and phase responses of the resonator for the frequency spectrum. The resultant data is exported as the real and imaginary components of the polar coordinates of the resonance frequency measurement. Thus, by individually calculating the difference between the drive resonance spectrum and the stationary condition of the setup; the resonance characteristic can be obtained by extruding the setup noise. The resulting resonance peak has no more than 3 dB gain and it is impossible to use the values directly for quality factor calculation. Keeping in the mind that the resonator die will have capacitive crosstalk between fingers and fields of silicon on the resonator; the steady state or 0V biased signal is vector subtracted from the result. Actually, the gain of the circuit is around 118 dB which means that the resultant magnitude of the resonator is 118 dB lower than the measured value.

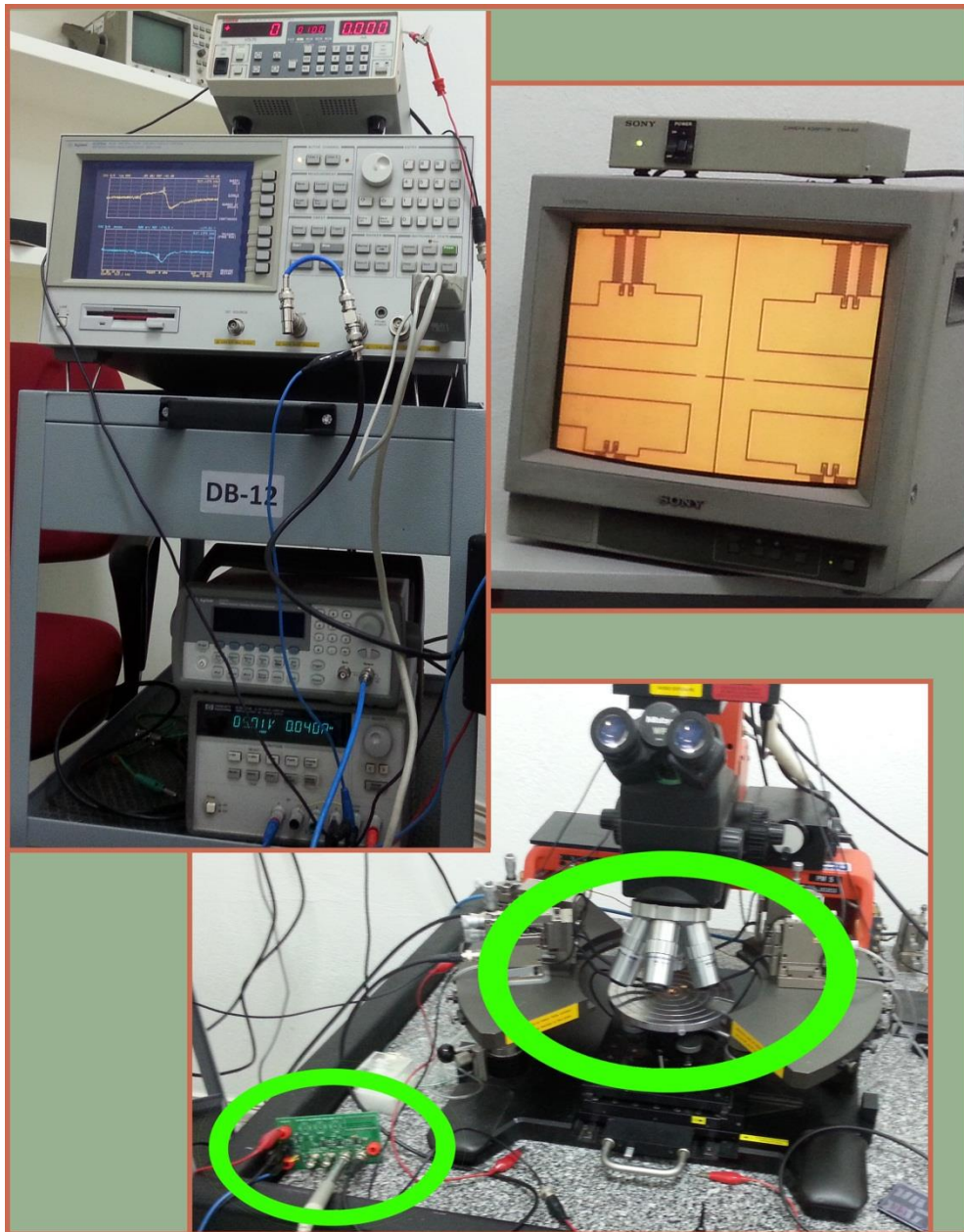


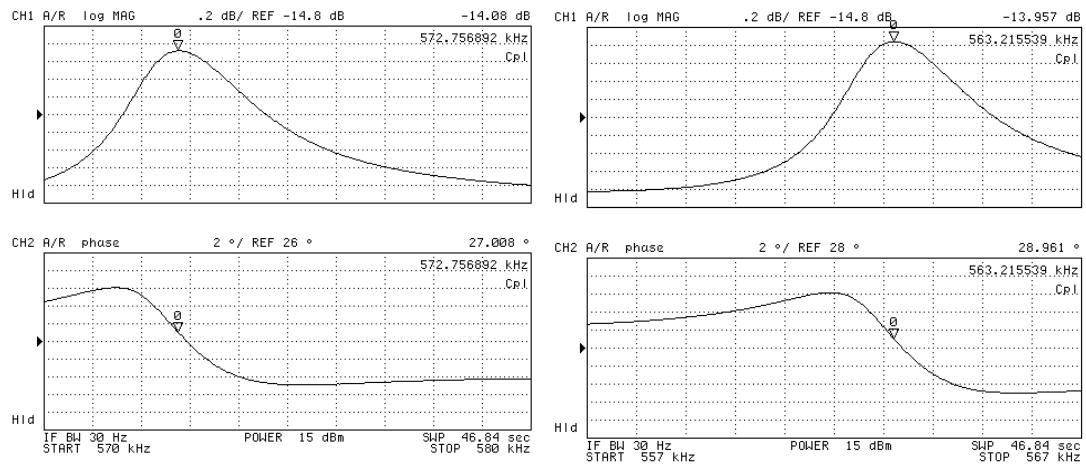
Figure 4.5: Resonator measurement setup is shown, with the network analyzer, DC supplies, and the interface TIA circuit. The device is measured with the network analyzer under probe station. The measured devices and the read-out circuit with TIA interface integrated are identified in green circles.

4.3 Test Results

Under open loop operation the resonator devices are tested, and the natural frequency and the quality factor of the devices are obtained. The designs of the resonators are slightly changed and the variety of the resonator designs are increased for the fabrication check points. The contribution of the design changes are summarized in Chapter 2. Although, 14 different designs are drawn for defining the limitations of the fabrication; 3 of them, Res #1, Res #4, and Res #10, are drawn for cross checking the resonator characteristics with the previous generation fabrications. Uniformity, linearity and mass detection abilities are reported for the gravimetric resonator design of BioMEMS group.

The measurements are done with differentiation analysis of the frequency spectrums of steady condition (zero applied bias) and operation mode (90-100 V bias applied) of the resonators. The resonance characteristics of the resonators are extracted as polar coordinates from the network analyzer and then, the magnitude and phase components are subtracted separately. Since, we assume that the steady condition noise caused from the setup and the circuitry, by these means, the contribution is eliminated. The investigations of the quality factor are done after these extractions completed.

The similar resonator designs show similar results with the previous generation fabrication measurements. The results with and without parylene are similar that the parylene coating shift the natural frequency of the resonator slightly with the increase in the mass of the resonator. Even for Res #14 and Res #13 resonators (248 μm x 128 μm proof mass) which have the largest proof masses, and the lowest minimum mass sensitivity; the mass of Parylene-C layer can be measured. In Figure 4.6, the shift of resonance peak can be observed for Res #7 design, from 572.8 kHz to 563.2 kHz after parylene coating.



(a)

(b)

Figure 4.6: The magnitude and phase measurements of (a) the resonator without coating and (b) with parylene coating are done for RES #7 device by direct observation of network analyzer. The shift of natural frequency is observed from 572.8 kHz to 563.2 kHz after parylene coating.

After the proper parylene coating is achieved with the novel Parylene-C coating method mentioned in the previous section; the in fluid trials are done for parylene coated devices with the new novel method. The buckling and the microfluidic channel operation under fluid flow are tested. As a start, the observation of microchannel sealing is tested by injecting water and IPA through microchannels carved inside the glass. The parylene coating which generates sufficient level of hydrophobicity should prevent the leakage on the resonator fingers and anchors [69]. After the leakage tests, the results are as expected. The novel parylene coating method that we proposed is working properly as required. In Figure 4.7, a simple test is done with simple capillary flow. The fluid flow injected from the input hole, and with capillary force the water come out of the output hole of the resonator die.

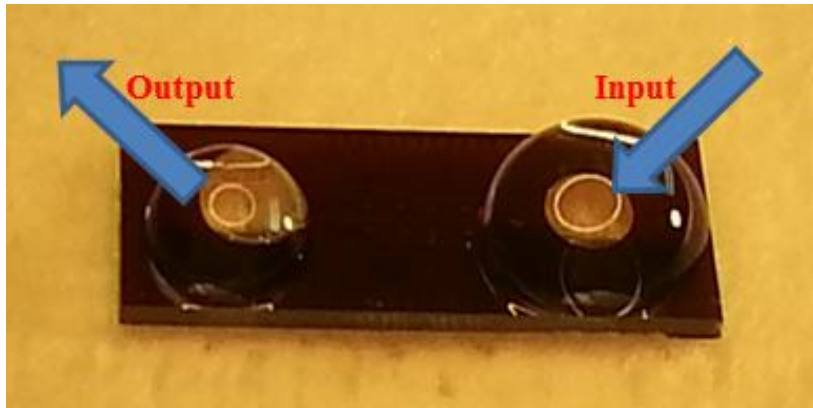


Figure 4.7: The capillary flow test is done with injecting DI water with syringe from one end of the microchannel and without any leakage water come out from the other end of the microchannel

Afterwards, the electronic tests with fluid inside the microchannel which are previously presented in previous generation studies have to be achieved, and we meet the goal. Actually, we have encountered a wide range contamination of the gold routing lines are shorted to the substrate active silicon that the operation of the contact pads are hindered. The BHF can not be cleaned from the narrow gaps of 5 μm silicon active layer and this result in operational problem during the measurements, we measure the system with directly contacting the silicon parts after laser cutting the routing metal connections to the proof mass. In this way, the measurements of the resonators including fluidic tests are successfully completed.

The resonance characteristics under fluidic operation are tested with and without parylene coating. As expected the resonance characteristic of the resonator under fluid without any hydrophobic coating can not withstand the fluidic damping. On the other hand, the characteristics of the parylene coated resonators are shown in Figure 4.8. The green line shows the resonance magnitude of the resonator under air damping, the red representation shows the resonance characteristics after parylene coating, and the blue line shows represents the resonance under fluid operation with parylene. The resonance natural frequency shift from 229.3 kHz to 221.5 kHz but the quality factor is also decreased from 764.3 to 573.0. The resonance frequency of the resonator with parylene coating is 221.6 kHz, and that is very close to the resonance

characteristics of the resonator under air damping with parylene coating. This result shows that the resonators are operational under fluid operation but the quality factor of the in fluid operation degrades considerably to 198 compared to over 750 quality factor levels of the resonators in air. However, the quality factor is improved compared to the previous studies of previous generation observations which have quality factors at the level of 50-70 inside fluidic environment [71]. The result supports the claim that the novel method of parylene coating prevents the liquid leakage in between gaps of fingers and anchors sufficiently.

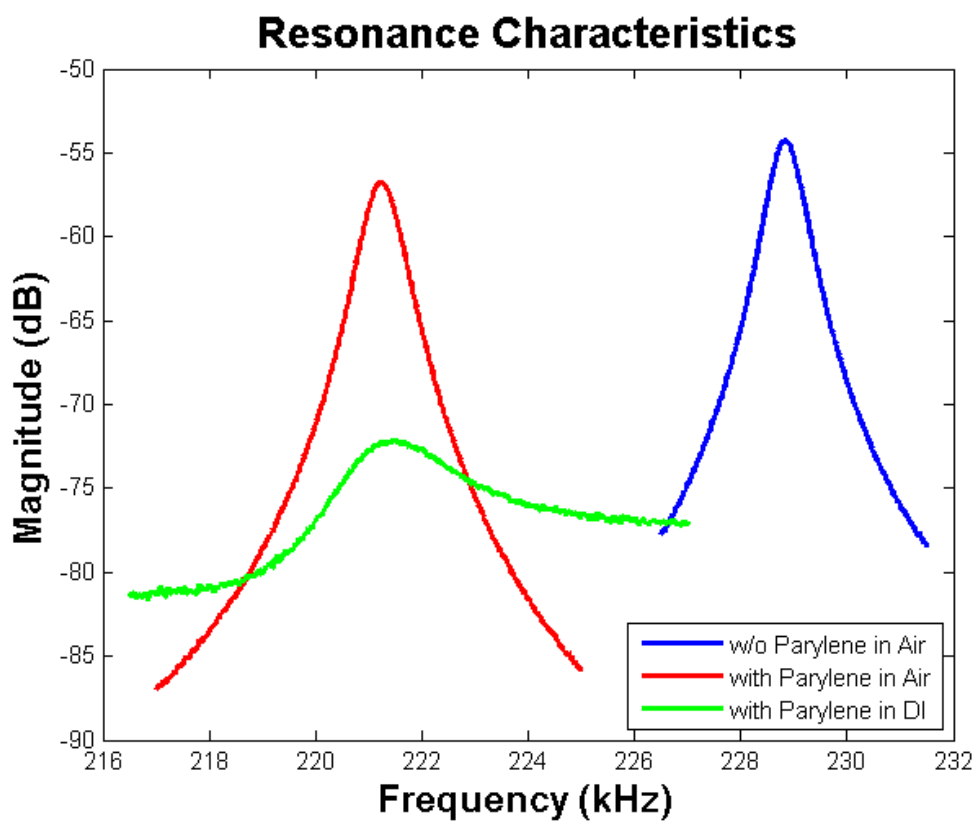


Figure 4.8: The mass of parylene can be observed with shift of resonance peak of the gravimetric resonator sensor. The resonance frequency is shifted down from 229.3 kHz (green) to 221.5 kHz (red) and the quality factor is also decreased from 764.3 to 573.0. The resonator with parylene coating under fluid flow shows 221.6 kHz resonance frequency and the quality factor drop to 198.4.

Also, the quality factor of many resonators benefit from the new fabrication flow. The damage free and contamination free fabrication method results in reproducible and reliable designed systems. The optimization of DRIE and so preventing notching effect for finger fabrication, produce sharper finger geometries. Thus the amplitude of the signal and the quality factor fruitfully benefit from these improvements. We can find resonators with quality factor of 1000 or higher which the quality factor was not increased above 750 in the previous generation fabrication flows. The comparison is shown in

Table 4.2 for the control group of similar architecture resonators. The resonators of the previous generation fabrication are stated as RCD and the new generation resonator devices are denoted as RES code. Also, for finger placement efficiency the proof masses of the new designs are changed slightly which causes a shift of the simulated natural frequencies of the similar designs with the previous and new generation fabrication flows. Firstly, the fabrication success for the smaller resonators with high natural frequencies is very close to null for the previous generation fabrication flow, many of them break during the fabrication. There is no recorded measurement of the smallest proof mass designs with $40\ \mu\text{m} \times 15\ \mu\text{m}$ proof mass. On the other hand, the yield of small sized resonators is high for the new fabrication flow and we achieve to measure the characteristics of the designs which are presented in

Table 4.2.

As mentioned before, the designs are changed with a view to increase the fabrication strength. Also, the proof mass areas are set for maximum number of finger placement so the capacitive sensing signal increases slightly and the amplitude of the magnitude of the resonators increases. The fabrication limits are tested for the smallest ($44\ \mu\text{m} \times 16\ \mu\text{m}$ proof mass) and the largest ($248\ \mu\text{m} \times 128\ \mu\text{m}$ proof mass) resonator designs. Both designs show reliable results. The smallest proof mass ($44\ \mu\text{m} \times 16\ \mu\text{m}$) designs can be properly measured first time. Also, the Cr/Au layer is adhered properly for bioactivation possibilities with no sticking problem (See Figure 4.9). Since the read-out circuitry show worse signal to noise ratio at the higher frequencies close to 1 MHz and the low capacitance values decrease the amplitude of the sensing

signal; the resonance characteristics are weak but they are convincing for the operation constraints.

Table 4.2: Comparison for the resonator controlling designs with the previous generation fabrications

| Resonator ID | Proof Mass (μm^2) | COMSOL (f_n) | Measured f_n | Quality Factor (Q) |
|---|--|----------------------------------|----------------------------------|-------------------------------|
| RCD #2 (3rd generation) | 40 x 15 | 1.71 MHz | - | - |
| RES #1 | 44 x 16 | 1.41 MHz | 806 kHz | 289 |
| RCD #4 (3rd generation) | 80 x 15 | 460 kHz | 258 kHz | 247 |
| RES #4 | 84 x 16 | 471 kHz | 232 kHz | 660 |
| RCD #5 (3rd generation) | 160 x 30 | 760 kHz | 563 kHz | 282 |
| RES #10 | 164 x 32 | 780 kHz | 537 kHz | 1033 |

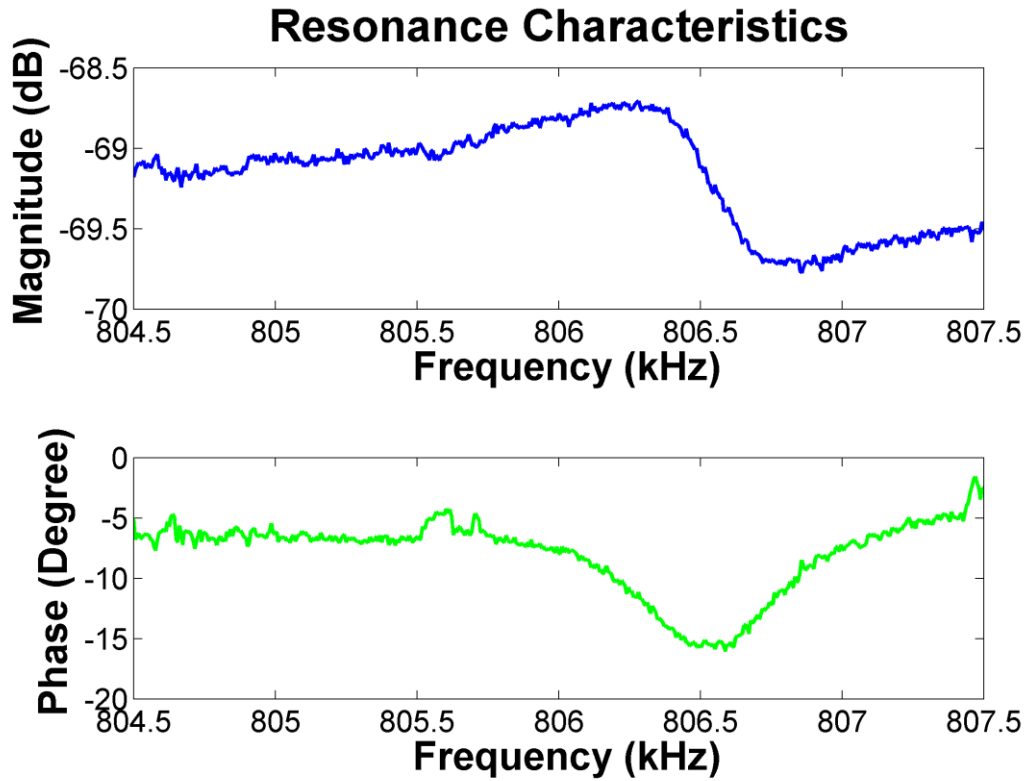


Figure 4.9: The magnitude and phase components of the resonance characteristics of RES #1 design with $44 \times 16 \mu\text{m}^2$ proof mass area and with natural frequency of 806 kHz and quality factor of 289.

On the other hand, the fabrication limits are tested on the opposite side with the largest resonators. The microfluidic channel embedded on top of the geometry and the higher bending possibility make them vulnerable for the fluidic applications. Moreover, the small minimum mass sensitivity could have caused eliminating the clinical functionality for these resonators. However, the measurements show that with the lowest resonance frequencies the devices show high durability for the fluidic operations and the low natural frequencies make them suitable for measurements with low signal to noise ratio. Therefore, the largest proof mass ($248 \times 128 \mu\text{m}^2$) devices RES # 13 and RES #14 are used for start-up tests of the read-out circuitry (See Figure 4.10).

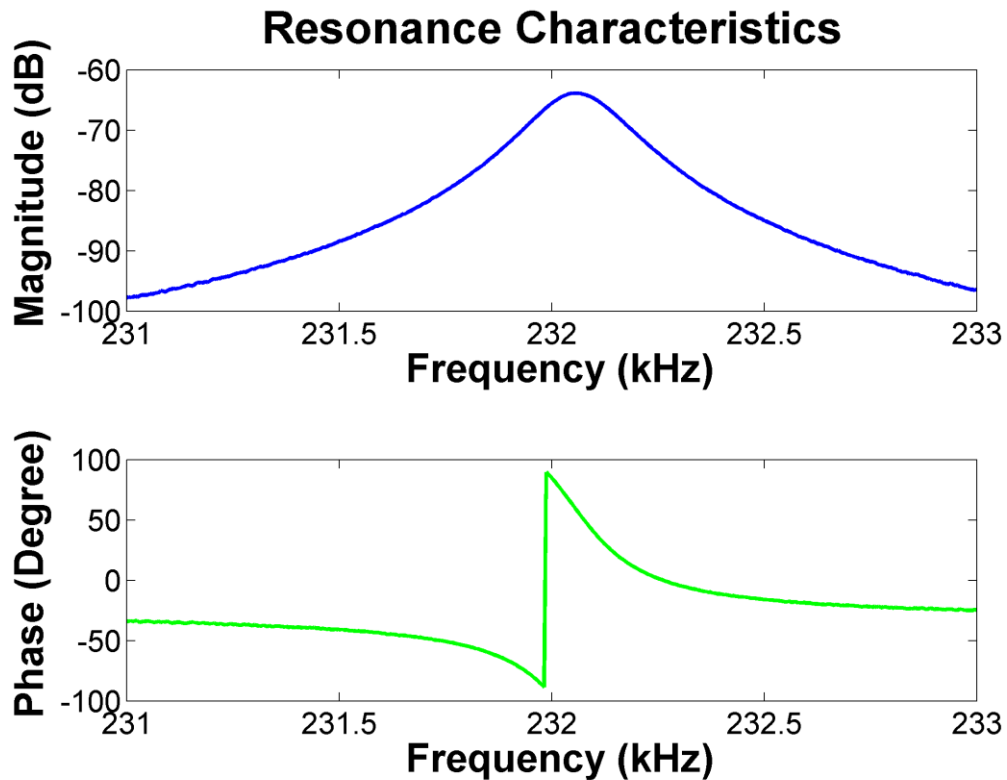


Figure 4.10: The magnitude and phase components of the resonance characteristics of RES #13 design with $248 \times 128 \mu\text{m}^2$ proof mass area and with natural frequency of 232 kHz and quality factor of 862.

Secondly, the simulated resonators' natural frequencies with COMSOL software show an undeniable shift with the measured natural frequencies, which is highly dependent on the simulation conditions and fabrication contamination of the resonators. Also, the simulations are done for bare silicon resonator devices, without any gold bioactivation coating. The effect of the Cr/Au coating is simulated in the COMSOL software and for instance; RES # 14, the natural frequency is calculated to be 420 kHz with bare silicon, if we introduce the Cr/Au (30 nm / 300 nm) layer to the simulation, the simulation results shift to 276 kHz and the measured natural frequency is around 229-233 kHz for this design. The final shift can be caused of fabrication and contamination during measurements. The previous generation studies lose many of the bioactivation gold sites up to the point of measurement so the results show more consistency with the bare silicon simulations.

4.4 Fabrication Yield Definition

Yield is defined as the number of working units coming out of a process divided by the number of fabricated units going into that process over a specified period of time. In this study, the final total yield can be defined as multiplication of each fabrication step yield results [79]. High process yields are essential for the production of reliable chips at a profit. Typically, the yield is defined for starting from fabrication level to packaging level and even to the transportation and selling level. For this thesis, the working devices for the yield are defined as the properly fabricated devices tested with visual inspection for defects after fabrication; and then, the resonance characteristics of the devices have to be in the range of expectation, under air damping.

The wafer fabrication yield is commonly limited by the number of process steps, wafer breakage and warping ratio, process variation, and process defects [79]. The number of process step is inversely proportional with the wafer fabrication total yield parameter because the each fabrication step is not perfect and contributes to the problems of the fabrication flow. The most important issue is the handling of the wafers during fabrication. The wafer breakage and contamination during process periods are not a major issue with silicon based substrates but the wafer surfaces must remain flat without any stress [80]. On the other hand, SOI wafers as used for the fabrication of the resonator devices has high stress from the silicon dioxide buried layer.

Other factors that cause a loss of yield can be defined as wafer diameter, die area, circuit density, crystal defect density, and process cycle time. These factors required to be as minimal as possible [80]. Besides, the wafer edge dies encounter many process defects for the wafer level uniformities are not perfect for all fabrication steps mentioned above. The fabrication yield in this thesis is mentioned after assembly and the final tests of resonance.

4.5 Fabrication Yield Results and Summary

As mentioned above, the yield in this thesis is considered as the final throughput ratio after the fabrication and resonance tests. According to the yield inspection of this study, the resonators are considered to be working if there is no major fabrication damage controlled under SEM and optical microscope analysis, and then, electronically they have to show a resonance peak with high quality factor ($Q > 500$) after the parylene layer coating and patterning. After these inspections, if the resonator holds these requirements, it is recorded for the resonator devices in wafer level map. These results are inspected in this section.

The resonators are closely inspected for the frequency analysis for the deviation characteristics depending on the fabrication diversity. Each die on the wafer encounter different conditions through the etching and deposition steps so a deviation is expected but the uniformity of the fabrication can be observed with this aspect. The data show consistency with the previous generation design simulations and measurement values. In fact, the resonators with same resonator dimensions deviate in %1 range of the measured natural frequencies depending on the layout placement on the wafer. For the previous generation results, there was a deviation in %5 range around the natural frequency for the same coded resonators depending on the location of the wafer placement.

This observation support the fabrication improvement, as seen on the SEM analysis through the whole wafer the DRIE etching profiles and the Cr/Au bioactivation layer uniformity are very similar. The yield percentage of the each process step is recorded so the total yield of fabrication can be inspected. With the measurements, the die to die mass variation through the wafer localizations is also proven similar. The non-uniformity coming from the process steps are mostly take root from the deep wet HF etches for recess gaps for metal routing lines and microfluidic channel fabrication. However, this wet etches non-uniformity only causes 8% deviation of microchannel dimensions at most. The SOI wafer correspondingly the resonators are not directly subjected to the HF etch but the lateral widening of the channel affect the fluidic flow sparingly.

Moreover, the wet etch and photolithography capabilities of the METU-MEMS facility is high and the process yield for each step is around 98% considering die level loss for 4 inch wafer fabrication flow. Although, the yield is high, all the wet etch and photolithography processes suffer from edge level process errors, so the extreme cases of resonator designs with smallest and largest proof mass areas are placed at the edge of the wafers. In Figure 4.11, the wafer map of the new generation process is given, the highest rate of loss of the specific location are revealed to be die location 27, 32, 33, and 38.

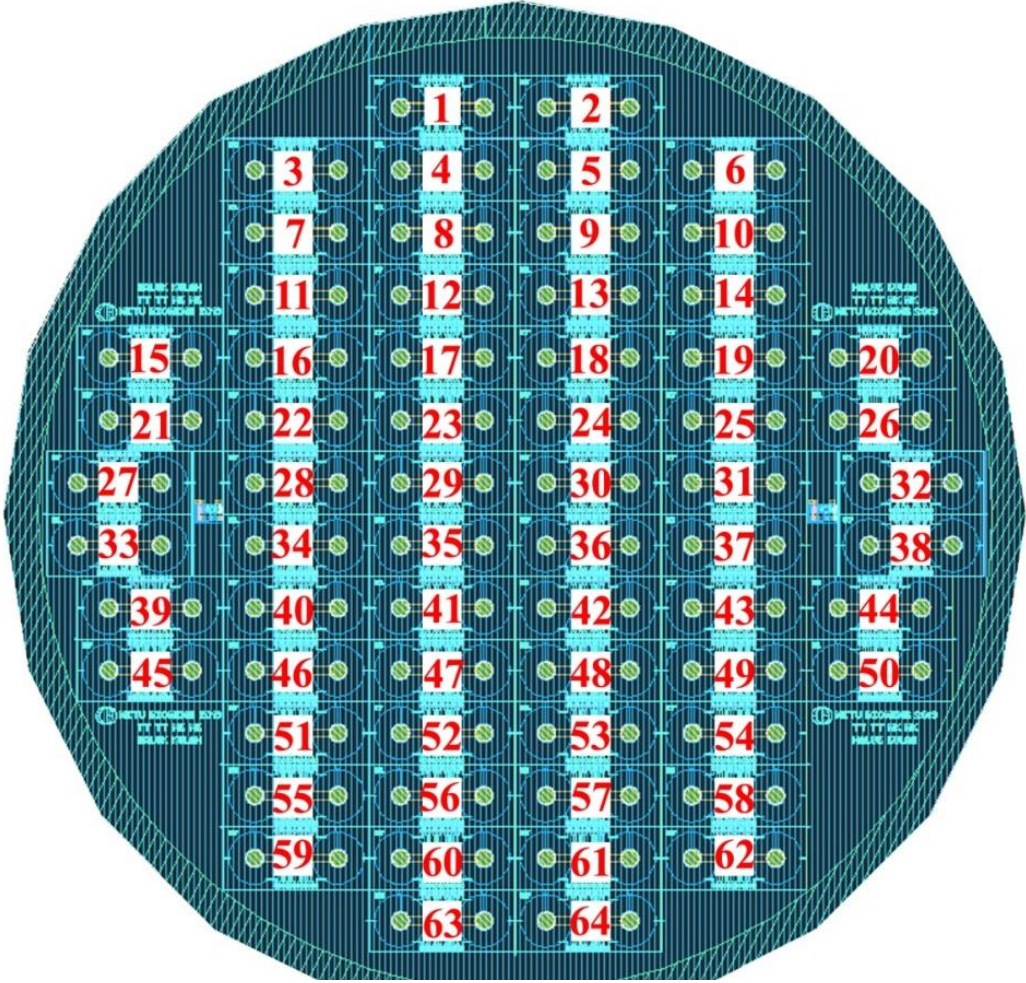


Figure 4.11: The wafer map with numerical representation of 64 dies with 14 different architectures of resonators are placed.

The gold bioactivation alignment and peeling off losses are observed to be confined to a low rate of 6% for the first trials of fabrication with metal etch. Further improvement is achieved with the lift-off technique and increasing the thickness of the adhesion layer of chromium to 30 nm from 15 nm that the loss of bioactivation fields are eliminated for most of the whole process wafers.

The other mainstream critical process steps are glass routing metallization that the spray coating solution explained in Chapter 3 solved the loss completely. Besides, the anodic bonding step needs further improvement, the stress of SOI wafers with thin active layer as in our application are under very high level surface stress and the anodic bonding process become the bottleneck for the wafer breakages [77]. Also, the sparking effect is still burning around 5-10% of the resonators throughout the whole wafer.

The final obstacle is the silicon backside handle layer removal and the BHF wet etch release of buried silicon dioxide layer of SOI. The general fabrication level yield is considerably high. Thus, it is validated that the wafer level uniformity of the fabrication is satisfactory for the new fabrication flow. The previous generation (3rd generation) fabrication process total fabrication level yield is around 5% or less but with the new fabrication flow if we do not consider the anodic bonding breakages caused by wafer stress specifications, the fabrication yield is high as 85-90% calculated for the total of 16 wafer level processes.

CHAPTER 5

CONCLUSION AND FUTURE WORK

In this thesis, a new fabrication process flow is presented for the gravimetric resonator sensors used for cell detection applications. The resonator designs are revised in geometry and evolved for the fabrication requirements. The results of the yield improvements are ramped up considerably. It is obvious that after many fabrication and design generations, the process performance reach to a certain level of maturity and reproducibility.

As a summary, the research objectives achieved throughout this thesis study are as follows:

- The new approach for the fabrication process flow taking root from improving each and only step; fruitfully increase the total yield of the fabrication. Experience from the previous generation fabrication flows, the yield which is not more than 5%, become as high as 90% for the low stressed SOIs.
- The novel method for hydrophobic conformal parylene coating other than the bioactivation field on the proof mass increases the quality factor of the device inside the fluids by preventing the fluid penetration in between the comb fingers and spring beams. As well, the thin parylene layer is useful for isolating the electronic circuit with the fluid environment. The accuracy and

the reproducibility of the novel method is shown with detailed EDS and SEM analysis and the in fluid tests prove that the method is operating as expected.

- The destructive wet processes on the suspended devices are eliminated completely with the new process flow. The requirement of the wet processes on suspended structures is eliminated with the newly proposed novel parylene patterning method.
- The resonance spectrum measurements for characterization of the resonators are performed in air and water environment. The advantage of the hydrophobicity of the parylene-C layer is demonstrated under fluid flow. The tests show that the devices are operational with relatively acceptable performance attributions.
- The amplification of the sensing signal beam for different designs with the new fabrication is validated and even the fabrication boundaries of the smallest and largest designs are successfully fabricated and tested in terms of the resonance characteristics.
- The new design of the resonators with strengthened folded spring anchors are eliminated the breakages or the ruptures and so the endurance of the devices increased considerably.
- The encountered problems during the fabrication processes have been accumulated the experiences and manipulations are done for the solutions on both the mask layout and the fabrication process flow. The aimed device attributes are achieved with proper patterning of parylene on top of the bioactivation gold sites on the proof masses of the resonators. The biocompatible parylene coated glass microchannel is also anodic bonded and aligned on top of the device layer.
- The sparking problem is decreased considerably with the new configuration of the resonators and the shorting all the wafer level components to each other. There is still a space for improvement but at this stage, the enhancement is obvious.
- The new fabrication method makes use of a glass microchannel which offer high control on the alignment with respect to the resonators. Thus, precise

control on the microchannel geometry provides a negligible leakage, and better optical transparency compared to the PDMS microchannel architectures.

- Different approaches are used for metal patterning of the bioactivation gold sites. The lift-off method is tried in comparison with the standard metal etch procedure. Both methods have advantages relative to each other and none of the procedures influence the yield considerably.
- The SOI buried oxide stress has a dominant effect on the yield of the fabrication. The stress results of different companies are tested during the fabrication and it is concluded that low buckling of wafer with oxide stress is required for the success of the fabrication process.

Finally, future work on this topic can be summarized as:

- The contamination of the metal routing lines and pads with releasing under BHF hinder the usage of active test setups with wire bonding. Some procedures are tested for cleaning but none of them achieved the requirement properly. Still, increasing the recess gaps on the routing metal lines at the design level will most probably solve the problem.
- The anodic bonding process step requires to be optimized further for the proper reproducibility. Yet, the SOI wafer stress is highly affecting the fabrication yield and required to be examined.
- There is an opportunity of improvement for parylene layer hydrophobicity, with double or triple coating and etching under plasma cycle repetitions for higher coating uniformity. Also, addition of the fluorine based plasma exposure during the oxygen plasma application can be beneficial with higher hydrophobicity degrees.
- The sparking damages of the resonators can still be improved. By the new arrangements, the sparking effect is decreased but not eliminated completely. The placement of the resonators with the drive and sense pads needs to be revised.

- The yield can be increased further if a shadow masking and alignment technique can be developed for the final parylene patterning step with the previous generation fabrication flow is also another promising idea.
- The crosstalk between the resonator drive, sense and proof mass electrodes arise from the capacitive coupling. This problem will prevent the closed loop operation capability of the resonators, so a new layout design is required to be modeled by taking the resistive and capacitive crosstalk issues into account.
- Experiments with different biological analytes like cancer cells, proteins, complex organic molecules, and toxins needs to be performed with the new resonator based devices under water environment. Then, we need to test the functionality of the devices under buffering medium, human serum, and finally whole blood environments.
- Packaging of the resonators will be done with proper fluidic inlet and outlets with production level approaches. This will benefit the general portability, lower the cost of the fabrication, and open a way to the mass manufacturing of these devices. At this stage, with closed and properly contacted systems by wire bond pads, the signal to noise ratio will improve, and as a result, the general sensor performance will boost considerably.

REFERENCES

- [1] S. S. Saliternan, “Fundamentals of BioMEMS and Medical Microdevices,” *The International Society of Optical Engineering SPIE Press*, USA, 2006.
- [2] R. Bashir, “BioMEMS: State-of-the-Art in Detection, Opportunities and Prospects,” *Advanced Drug Delivery Reviews*, vol. 56, pp. 1565-1586, 2004.
- [3] A. Manz, N. Graber, and H. M. Widmer, “Miniaturized Total Chemical Analysis Systems: A Novel Concept for Chemical Sensing,” *Sensors and Actuators B*, vol. B1, pp. 244–248, 1990.
- [4] N. T. Nguyen, S. A. M. Shaegh, N. Kashaninejad, and D. T. Phan, “Design, Fabrication and Characterization of Drug Delivery Systems Based on Lab-on-a-Chip Technology,” *Advanced Drug Delivery Reviews*, vol. 65, no. 11-12, pp. 1403-1419, 2013.
- [5] N. Maluf and K. Williams, “An Introduction to Microelectromechanical Systems Engineering,” *Artech House Inc. Press*, USA, 2nd edition, 2004.
- [6] K. Menon, R. A. Joy, N. Sood, and R. K. Mittal, “The Applications of BioMEMS in Diagnosis, Cell Biology and Therapy: A Review,” *BioNanoScience*, vol. 3, no. 4, pp. 356-366, 2013.
- [7] J. H. Wang, C. H. Wang, W. S. Ling, L. Jheng, S. W. Wang, and G. B. Lee, “Integrated Microfluidic System for HIV Detection,” *IEEE 25th Conference on Micro Electro Mechanical Systems (MEMS)*, France, pp. 961-964, 2012.
- [8] L. Beker, Ö. Zorlu, N. Göksu, and H. Külah, “Stimulating Auditory Nerve with MEMS Harvesters for Fully Implantable and Self-Powered Cochlear Implants,” *Transducers & Eurosensors XXVII: The 17th International*

- Conference on Solid-State Sensors, Actuators and Microsystems*, Spain, pp. 1663-1666, 2013.
- [9] S. H. Lee, J. H. Jung, Y. M. Chae, and J. Y. Kang, "Fabrication and Characteristics of Implantable and Flexible Nerve Cuff Electrode for Neural Interfaces," *4th International IEEE Conference on Neural Engineering (EMBS)*, Turkey, pp. 80-83, 2009.
- [10] E. Nuxoll, "BioMEMS in Drug Delivery," *Advanced Drug Delivery Reviews*, vol. 65, no. 11-12, pp. 1611-1625, 2013.
- [11] J. Zhou, A. V. Ellis, and N. H. Voelcker, "Recent Developments in PDMS Surface Modification for Microfluidic Devices," *Electrophoresis*, vol. 31, no. 1, pp. 2-16, 2010.
- [12] W. C. Kuo, and C. W. Chen, "Fabrication Suspended High-Aspect-Ratio Parylene Structures for Large Displacement Requirements," *International Journal of Automation and Smart Technology*, vol. 4, no. 2, pp. 105-112, 2014.
- [13] S. Bhattacharya, J. Jang, L. Yang, D. Akın, R. Bashir, "BioMEMS and Nanotechnology Based Approaches for Rapid Detection of Biological Entities," *Journal of Rapid Methods and Automation in Microbiology*, vol. 15, pp. 1-32, 2007.
- [14] E. Lagally, "Microfluidics and Nanotechnology: Biosensing to the Single Molecule Limit," *CRC Press*, USA, 2014.
- [15] S. C. Hur, A. J. Mac, and D. Di Carlo, "High Throughput Size Based Rare Cell Enrichment Using Microscale Vortices," *Biomicrofluidics*, vol. 5, pp. 22206-22216, 2011.
- [16] Z. Mei, S. H. Cho, A. Zhang, J. Dai, T. F. Wu, and Y. H. Lo, "Counting Leukocytes from Whole Blood Using a Lab-on-a-Chip Coulter Counter," *Annual International Conference of the IEEE Engineering in Medicine and Biology Society (EMBC)*, USA, pp. 6277-6280, 2012.

- [17] K. Khoshmanesh, S. Nahavandi, S. Baratchi, A. Mitchell and K. Kalantar-zadeh, "Dielectrophoretic Platforms for Biomicrofluidic Systems," *Biosensors and Bioelectronics*, vol. 26, pp. 1800–1814, 2011.
- [18] V. Lecaute, A. K. White, A. Singhal, and C. L. Hansen, "Microfluidic Single Cell Analysis: From Promise to Practice," *Current Opinion in Chemical Biology*, vol. 16, pp. 381-390, 2012.
- [19] J. Chen, J. Li, and Y. Sun, "Microfluidic Approaches for Cancer Cell Detection, Characterization, and Separation," *Lab on a Chip*, vol. 12, pp. 1753-1767, 2012.
- [20] T. S. Pui, Y. Chen, C. C. Wong, R. Nadipalli, R. Weerasekera, S. K. Arya, H. Yu, and R. A. Rahman, "High Density CMOS Electrode Array for High Throughput and Automated Cell Counting," *Sensors and Actuators B: Chemical*, vol. 181, pp. 842-849, 2013.
- [21] C. L. Chang, S. I. Jalal, W. Huang, A. Mahmood, D. E. Matei, and C. A. Savran, "High Throughput Immunomagnetic Cell Detection Using a Microaperture Chip System," *IEEE Sensors Journal*, vol. 14, no. 9, pp. 3008-3013, 2014.
- [22] N. M. Toriello, E. S. Douglas, N. Thaitrong, S. C. Hsiao, M. B. Francis, C. R. Bertozzi, and R. A. Mathies, "Integrated Microfluidic Bioprocessor for Single-Cell Gene Expression Analysis," *Proceedings of National Academy of Sciences (PNAS)*, vol. 105, pp. 20173-20178, 2008.
- [23] T. J. Chen, J. C. Chang, Y. C. Chang, and F. G. Tseng, "High Density Monolayer Cells Self Assembly Chip for High Throughput Rare Cell Detection," *IEEE 26th Conference on Micro Electro Mechanical Systems (MEMS)*, China, pp. 923-926, 2013.
- [24] F. Fernandez, O. G. Lopez, E. Tellechea, A. C. Asensio, J. F. Moran, and I. Cornago, "Regenerable Plasmonic Biosensor Based on Gold Nanolines Pattern and Common Laboratory Spectrophotometer," *IEEE Transactions on Nanotechnology*, vol. 13, no. 2, pp. 308-313, 2014.

- [25] J. Musayev, C. Altiner, Y. Adıgüzel, H. Külah, S. Eminoglu, and T. Akin, "Capturing and Detection of MCF-7 Breast Cancer Cells with a CMOS Image Sensor," *Sensors and Actuators A: Physical*, vol. 215, pp. 105-114, 2014.
- [26] H. Feng, S. Sang, W. Zhang, G. Li, P. Li, J. Hu, S. Du, and X. Wei, "Fundamental Study of Micro-Cantilever for More Sensitive Surface Stress Based Biosensor," *Key Engineering Materials*, vol. 562, pp. 334-338, 2013.
- [27] A. Boisen, and T. Thundat, "Design and Fabrication of Cantilever Array Biosensors," *Materials Today*, vol. 12, no. 9, pp. 32-38, 2009.
- [28] K. C. Cheung, and P. Renaud, "BioMEMS for Medicine: On Chip Cell Characterization and Implantable Microelectrodes," *Solid State Electronics*, vol. 50, pp. 551-557, 2006.
- [29] T. Sannomiya, T. E. Balmer, C. Hafner, M. Heuberger, and J. Voros, "Optical Sensing and Determination of Complex Reflection Coefficients of Plasmonic Structures Using Transmission Interferometric Plasmonic Sensor," *Review of Scientific Instruments*, vol. 81, pp. 53102-53111, 2010.
- [30] W. Zhang, H. Feng, S. Sang, Q. Shi, J. Hu, and G. Li, "Structural Optimization of the Micro Membrane for a Novel Surface Stress Based Capacitive Biosensor," *Microelectronic Engineering*, vol. 106, pp. 9-12, 2013.
- [31] S. Sang, Y. Zhao, W. Zhang, P. Li, J. Hu, and G. Li, "Surface Stress Based Biosensors," *Biosensors and Bioelectronics*, vol. 51, pp. 124-135, 2014.
- [32] A. Heidari, Y. J. Yoon, M. K. Park, W. T. Park, and J. T. M. Lin, "Ultrasensitive Dielectric Filled Lamé Mode Biomass Sensor," *IEEE 16th International Solid-State Sensors, Actuators and Microsystems Conference (TRANSDUCERS)*, China, pp. 2259-2262. 2011.
- [33] F. Liu, A. N. Nordin, and I. Voiculescu, "Multiparametric MEMS Biosensor for Cell Culture Monitoring," *IEEE Design, Test, Integration and Packaging of MEMS/MOEMS (DTIP)*, Spain, pp. 1-5, 2013.

- [34] X. Huang, J. Xu, H. F. Ji, G. Li, and H. Chen, "Quartz Crystal Microbalance Based Biosensor for Rapid and Sensitive Detection of Maize Chlorotic Mottle Virus," *Analytical Methods*, vol. 6, no. 13, pp. 4530-4536, 2014.
- [35] F. J. Gruhl, and K. Lange, "Surface Acoustic Wave (SAW) Biosensor for Rapid and Label Free Detection of Penicillin G in Milk," *Food Analytical Methods*, vol. 7, pp. 430-437, 2014.
- [36] J. Tamayo, P. M. Kosaka, J. J. Ruz, A. S. Paulo, and M. Calleja, "Biosensors Based on Nanomechanical Systems," *Chemical Society Reviews*, vol. 42, pp. 1287-1311, 2013.
- [37] A. Boisen, S. Dohn, S. S. Keller, S. Schmid, and M. Tenje, "Cantilever-Like Micromechanical Sensors," *Reports on Progress in Physics*, vol. 74, pp. 36101-36131, 2011.
- [38] A. Heidari, Y. J. Yoon, M. Lee, L. Khine, M. K. Park, and J. M. L. Tsai, "A Novel Checker Patterned AlN MEMS Resonator as Gravimetric Sensor," *Sensors and Actuators A: Physical*, vol. 189, pp. 298-306, 2013.
- [39] S. Faegh, and N. Jalili, "Comprehensive Distributed Parameters Modeling and Experimental Validation of Microcantilever Based Biosensors with an Application to Ultrasmall Biological Species Detection," *Journal of Micromechanics and Microengineering*, vol. 23, pp. 25007-25019, 2013.
- [40] Y. Chai, S. Horikawa, A. Simonian, D. Dyer, and B. A. Chin, "Wireless Magnetoelastic Biosensors for the Detection of Salmonella on Fresh Produce," *IEEE 7th International Conference on Sensing Technology*, New Zealand, 2013.
- [41] T. P. Burg, M. Godin, S. M. Knudsen, W. Shen, G. Carlson, J. S. Foster, K. Babcock, and S. R. Manalis, "Weighing of biomolecules, single cells and single nanoparticles in fluid," *Nature*, vol. 446, pp. 1066-1069, 2007.
- [42] S. Poshtiban, A. Singh, G. Fitzpatrick, and S. Evoy, "Bacteriophage Tail Spike Derivatized Microresonator Arrays for Specific Detection of Pathogenic Bacteria," *Sensor and Actuators B: Chemical*, vol. 181, pp. 410-416, 2013.

- [43] K. Park, J. Jang, D. Irimia, J. Sturgis, J. Lee, J. P. Robinson, M. Toner, and R. Bashir, "Living Cantilever Arrays for Characterization of Mass of Single Live Cells in Fluids," *Lab on a Chip*, vol. 8, no. 7, pp. 1034-1041, 2008.
- [44] K. Park, L. J. Millet, N. Kim, H. Li, X. Jin, G. Popescu, N. R. Aluru, K. J. Hsia, and R. Bashir, "Measurement of Adherent Cell Mass and Growth," *Proceedings of the National Academy of Sciences*, vol. 107, no. 48, pp. 20691-20696, 2010.
- [45] K. Park, N. Kim, D. T. Morissette, N. R. Aluru, and R. Bashir, "Resonant MEMS Mass Sensors for Measurement of Microdroplet Evaporation," *Journal of Microelectromechanical Systems*, vol. 21, no. 3, pp. 702-711, 2012.
- [46] A. Heidari, Y. J. Yoon, W. T. Park, P. C. Su, J. Miao, J. T. M. Lin, and M. K. Park, "Biotin-Streptavidin Binding Interactions of Dielectric Filled Silicon Bulk Acoustic Resonators for Smart Label Free Biochemical Sensor Applications," *Sensors*, vol. 14, no. 3, pp. 4585-4598, 2014.
- [47] S. Joshi, S. Hung, and S. Vangallatore, "Design Strategies for Controlling Damping in Micromechanical and Nanomechanical Resonators," *EPJ Techniques and Instrumentation*, vol. 1, no. 5, pp. 1-14, 2014.
- [48] J. Linden, and E. Oesterschulze, "Improving the Quality Factor of Cantilevers in Viscous Fluids by the Adaptation of Their Interface," *Applied Physics Letters*, vol. 100, p. 113511, 2012.
- [49] S. D. Vishwakarma, A. K. Pandey, J. M. Parpia, D. R. Southworth, H. G. Craighead, and R. Pratap, "Evaluation of Mode Dependent Fluid Damping in a High Frequency Drumhead Microresonator," *Journal of Microelectromechanical Systems*, vol. 23, no. 2, pp. 334-346, 2014.
- [50] G. A. Cranch, J. E. Lane, G. A. Miller, and J. W. Lou, "Low Frequency Driven Oscillations of Cantilevers in Viscous Fluids at Very Low Reynolds Number," *Journal of Applied Physics*, vol. 113, pp. 194904-194914, 2013.
- [51] G. Zhang, L. Zhao, Z. Jiang, S. Yang, Y. Zhao, E. Huang, R. Hebibul, X. Wang, and Z. Liu, "Surface Stress Induced Deflection of a Microcantilever

- with Various Widths and Overall Microcantilever Sensitivity Enhancement via Geometry Modification,” *Journal of Physics D: Applied Physics*, vol. 44, p. 425402, 2011.
- [52] G. Sosale, K. Das, L. Frechette, and S Vengallatore, “Controlling Damping and Quality Factors of Silicon Microcantilevers by Selective Metallization,” *Journal of Micromechanics and Microengineering*, vol. 21, p. 105010, 2011.
- [53] R. Cox, F. Cosse, S. M. Heinrich, O. Brand, and I. Dufour, “Characteristics of Laterally Vibrating Resonant Microcantilevers in Viscous Liquid Media,” *Journal of Applied Physics*, vol. 111, p. 14907, 2012.
- [54] J. Wooldridge, A. M. Piniella, M. Stewart, T. A. V. Shean, P. M. Weaver, and M. G. Cain, “Vertical Comb Drive Actuator for the Measurement of Piezoelectric Coefficients in Small Scale Systems,” *Journal of Micromechanics and Microengineering*, vol. 23, no. 3, p. 35028, 2013.
- [55] H. Chang, H. Zhao, F. Ye, G. Yuan, J. Xie, M. Kraft, and W. Yuan, “A Rotary Comb Actuated Microgripper with a Large Displacement Range,” *Microsystem Technologies*, vol. 20, no. 1, pp. 119-126, 2014.
- [56] P. Singh, P. Gupta, P. Srivastava, and R. K. Chaudhary, “Design and Modeling of MEMS Capacitive Gyroscope,” *IEEE International Conference on Energy Efficient Technologies for Sustainability (ICEETS)*, India, pp. 907-911, 2013.
- [57] L. Dong, Y. Pan, J. Lou, and J. Bao, “Study of the Influence of Fringe Edge on MEMS Capacitive Accelerometers Self-Calibration,” *Microsystem Technologies*, vol. 22, no. 3, pp. 1-8, 2014.
- [58] N. Lobontiu, and E. Garcia, “Mechanics of Micro-Mechanical Systems,” *Kluwer Academic Publishers*, USA, 2005.
- [59] G. Li, and H. Hughes, “Review of Viscous Damping in Micro-Machined Structures,” *Proceedings of SPIE*, vol. 4176, pp. 30-46, 2000.
- [60] X. Zhang, and W. C. Tang, “Viscous Air Damping in Laterally Driven Microresonators,” *IEEE Workshop on Micro Electro Mechanical Systems (MEMS)*, Japan, pp. 199-204, 1994.

- [61] M. Gologanu, C. G. Bostan, V. Avramescu, and O. Buiu, "Damping Effects in MEMS Resonators," *IEEE International Semiconductor Conference (CAS)*, Romania, pp. 67-76, 2012.
- [62] A. K. Pandey, R. Pratap, and F. S. Chau, "Influence of Boundary Conditions on the Dynamic Characteristics of Squeeze Films in MEMS Devices", *Journal of Microelectronic Systems*, vol. 16, no. 4, pp. 893–903, 2007.
- [63] J. A. Kubby, "A Guide to Hands on MEMS Design and Prototyping," *Cambridge University Press*, UK, 2011.
- [64] T. R. Albrecht, P. Grutter, D. Horne, and D. Rugar, "Frequency Modulation Detection Using High-Q Cantilevers for Enhanced Force Microscope Sensitivity," *Journal of Applied Physics*, vol. 69, pp. 668-673, 1991.
- [65] A. W. Chi, A. A. Azid, and B. Y. Majlis, "Formulation of Stiffness Constant and Effective Mass for a Folded Beam," *Archives of Mechanics*, vol. 62, no. 5, pp. 405-418, 2010.
- [66] A. N. Radwan, R. S. Almikhlafi, and M. S. M. Soliman, "Performance Comparison of Commonly Used MEMS Springs: Double-Folded, U-Shaped and Fish Hook," *IEEE International Electronics, Communications and Photonics Conference (SIECPC)*, Saudi Arabia, pp. 1-6, 2013.
- [67] T. Y. Chang, V. G. Yadav, S. D. Leo, A. Mohedas, B. Rajalingam, C. L. Chen, M. R. Dökmeci, and A. Khademhosseini, "Cell and Protein Compatibility of Parylene-C Surfaces," *Langmuir*, vol. 23, no. 23, pp. 11718-11725, 2007.
- [68] C. L. Chen, S. Jinno, H. Moller, B. Rajalingam, S. H. Chao, S. Selvarasah, A. Khademhosseini, and M. R. Dökmeci, "Multilayer Parylene-C Stencils for Dynamically Controlling Cell Interactions," *IEEE 21th Conference on Micro Electro Mechanical Systems (MEMS)*, USA, pp. 276–279, 2008.
- [69] D. Eroğlu, and H. Külah, "Quality Factor Enhancement of Lateral Microresonators in Liquid Media by Hydrophobic Coating," *Journal of Microelectromechanical Systems*, vol. 20, no. 5, pp. 1068-1070, 2011.

- [70] D. Eroğlu, E. Bayraktar, and H. Kùlah, "A Laterally Resonating Gravimetric Sensor with Uniform Mass Sensitivity and High Linearity," *IEEE 16th Solid-State Sensors, Actuators and Microsystems Conference (TRANSDUCERS)*, China, pp. 2255-2258, 2011.
- [71] D. Eroğlu, "Development of a Resonant Mass Sensor for MEMS Based Cell Detection Applications," *M. Sc. Thesis for Electrical and Electronics Engineering*, Middle East Technical University, Turkey, 2012.
- [72] E. Bayraktar, "Design and Implementation of a MEMS Based Gravimetric Detector for Cytometry Applications," *M. Sc. Thesis for Electrical and Electronics Engineering*, Middle East Technical University, Turkey, 2010.
- [73] V. Milanovic, "Multilevel Beam SOI MEMS Fabrication and Applications," *Journal of Micromechanical Systems*, vol. 13, no. 1, pp. 19-30, 2004.
- [74] S. E. Alper, "MEMS Gyroscopes for Tactical Grade Inertial Measurement Applications," *Doctor of Philosophy*, The Graduate School of Natural and Applied Sciences, Middle East Technical University, Turkey, 2005.
- [75] M. M. Torunbalcı, "Wafer Level Vacuum Packaging of MEMS Sensors and Resonators," *M. Sc. Thesis for Micro and Nanotechnology*, Middle East Technical University, Turkey, 2011.
- [76] S. E. Alper, A. Aydemir, and T. Akın, "Stepped-Etching for Preserving Critical Dimensions in through Wafer Deep Reactive Ion Etching of Thick Silicon," *15th IEEE International Conference on Solid-State Sensors, Actuators and Microsystems, (TRANSDUCERS)*, USA, pp. 1110-1113, 2009.
- [77] C. L. Chen, S. Jinno, H. Moller, B. Rajalingam, S. H. Chao, S. Selvarasah, A. Khademhosseini, and M. R. Dökmeci, "Multilayer Parylene-C Stencils for Dynamically Controlling Cell Interactions," *IEEE 21th Conference on Micro Electro Mechanical Systems (MEMS)*, USA, pp. 276-279, 2008.
- [78] E. Meng, P. Y. Li, Y. C. Tai, "Plasma Removal of Parylene C," *Journal of Micromechanics and Microengineering*, vol. 18, no. 4, pp. 1-13, 2008.
- [79] P. V. Zant, "Microchip Fabrication: A Practical Guide to Semiconductor Processing," *McGraw Hill Publishing Company*, USA, 2nd edition, 1990.

- [80] G. S. May and C. J. Spanos, “Fundamentals of Semiconductor Manufacturing and Process Control,” *IEEE Wiley Interscience Press*, USA, 2006.